An Attitude Control System for the Deployment and Stabilisation of a Tethered Dual CubeSat Mission

by

Mike-Alec Kearney

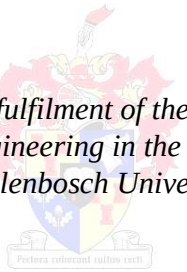

Thesis presented in partial fulfilment of the requirements for the degree Master of Science in Engineering in the Faculty of Engineering at Stellenbosch University

Supervisor: Prof. W.H. Steyn
Department of Electrical & Electronic Enginieering

March 2013

Declaration

By submitting this thesis electronically, I declare that the entirety of the work contained therein is my own, original work, that I am the sole author thereof (save to the extent explicitly otherwise stated), that reproduction and publication thereof by Stellenbosch University will not infringe any third party rights and that I have not previously in its entirety or in part submitted it for obtaining any qualification.

March 2013

"Any intelligent fool can make things bigger, more complex, and more violent. It takes a touch of genius, and a lot of courage, to move in the opposite direction."

Albert Einstein

Abstract

The use of electrodynamic tethers on-board satellites is an exciting scientific prospect. These conductive tethers provide the means for satellites to generate power and to do propulsion by electrodynamic interaction with the geomagnetic field. Although well researched in theory, the concept has not enjoyed much success in practice. This study aims to utilise low-cost CubeSats as experimental tool to verify many of the theoretical principles that govern the behaviour of conductive tethers in orbit.

The study provides a theoretical background of the concept by evaluating past tether missions and analysing existing theory. A feasible application of an electrodynamic tether within the size and weight limitations of a Nano-satellite is formulated. Existing theoretical work is adapted to model the dynamics and electrodynamics of specifically Nano-satellites. Using these mathematical models, control and estimation algorithms are designed which would provide stable deployment of a tethered CubeSat pair and stable control of the orientation of the tethered system. To be able to implement these algorithms on a satellite mission, a prototype of a sensor capable of measuring the angle of the tether using a CMOS camera is designed and built. A hardware platform is built to test the deployment of the tether using an electric motor. Electronics are designed to control the operation of the camera, to do motor control, and to run control and estimation algorithms. Using the results obtained from the practical tests done on the hardware, and using the theoretical models and control algorithms designed, a full orbital simulation of the deployment was done. This simulation includes the performance of the deployment system, the electrodynamic performance of the tether in earth's plasmasphere, and the estimation and control algorithms to control the system. Different deployment strategies are analysed and their performance are compared.

Opsomming

Die gebruik van elektrodinamiese toue aanboord satelliete is 'n opwindende wetenskaplike vooruitsig. Hierdie geleidende toue verleen aan die satelliete die vermoë om krag op te kan wek en propulsie deur elektriese interaksie met die geomagnetiese veld te kan doen. Alhoewel dit goed nagevors is in teorie, het die konsep nog nie veel sukses in die praktyk geniet nie. Hierdie studie het dit ten doel om lae-koste CubeSats aan te wend as 'n eksperimentele instrument om baie van die teoretiese beginsels wat geld vir die gedrag van geleidende toue in wentelbane te verifieer.

Die studie bied 'n teoretiese agtergrond van die konsep deur die evaluering van vorige tou-missies sowel as die analise van bestaande teorie. 'n Uitvoerbare toepassing van 'n elektrodinamiese tou binne die grootte- en gewigsbeperkinge van 'n Nano-satelliet is geformuleer. Bestaande teoretiese werk is aangepas om die dinamika en elektrodinamika spesifiek van toepassing op Nano-satelliete, te modelleer. Deur hierdie wiskundige modelle te gebruik, is beheer- en afskattingsalgoritmes ontwerp wat stabiele ontplooiing van 'n verbinde CubeSat-paar en stabiele beheer van die oriëntasie van die verbinde stelsel sal verseker. Om hierdie algoritmes te implementeer op 'n satelliet-sending, is 'n prototipe van 'n sensor wat in staat is om die hoek van die tou met behulp van 'n CMOS kamera te meet, ontwerp en gebou. 'n Hardeware platform is gebou om die ontplooiing van die tou met behulp van 'n elektriese motor te toets. Elektronika is ontwerp om die kamera te beheer, motor beheer te doen asook om beheer- en afskattingsalgoritmes uit te voer. Deur gebruik te maak van die resultate wat verkry is tydens die praktiese toetse wat gedoen is op die hardeware, en deur gebruik te maak van die teoretiese modelle en beheeralgoritmes wat ontwerp is, is 'n volle wentelbaan-simulasie van die ontplooiing gedoen. Hierdie simulasie sluit die gedrag van die ontplooiingstelsel, die elektriese gedrag van die geleidende tou in die aarde se plasmasfeer, en die afskatting- en beheeralgoritmes om die stelsel te beheer in. Verskillende ontplooiingstrategieë word ontleed en hul gedrag word vergelyk.

Preamble

Acknowledgements

I would like to thank the following persons and institutes for their support and guidance:

Prof W.H. Steyn, for always being willing to help, and believing in me by giving me the freedom to express myself in every aspect of my work.

Alexis Kearney, my father, for providing the inspiration, wisdom and principles needed to complete my studies as well as providing financial support during my entire studies.

Mariaan Kearney, my mother, for providing the motivation, determination, self-belief, and love needed for me to complete my studies.

Stellenbosch University, for providing me with an excellent education and memories to last a lifetime.

Mrs A van Jaarsveld, my English teacher, for providing me with an education in the art of reasoning and for providing assistance with editing the language of this document.

Notations and Conventions

Bold and *italic* are used for emphasis and to signify the first use of a term.

Vectors are written in **Bold** (e.g. $\boldsymbol{p}$)

Unit vectors are denoted with a vector $\boldsymbol{e}$ with a subscript providing reference to the parent vector (e.g. The vector $\boldsymbol{p}$ can be written as $\boldsymbol{p} = p\hat{\boldsymbol{e}}_{\boldsymbol{p}}$).

`Courier New` is used for all the source codes and generally for anything that would be typed literally when programming, including *keywords*, *constants*, *method names*, *variables*, *class names*, and *interface names*.

The present report is divided into *chapters*. Chapters are broken down into *sections*.

Where necessary, sections are further broken down into *subsections* and subsections contain *paragraphs*.

Figures, Tables and Listings are numbered inside a chapter. For example, a reference to *Figure j* of chapter *i* is noted *Figure i.j*.

References are tagged inside square brackets [].

As a respect to both genders, *he* and *she* are used interchangeably in this document.

List of Abbreviations and Symbols

Symbols:

Ω	Right ascension of the ascending node
i	Inclination
u	Argument of latitude
R	Orbital radius
θ	In-plane angle
ϕ	Out-of-plane angle
L	Tether length
$X_i\ Y_i\ Z_i$	Inertial-referenced vector set
$X_o\ Y_o\ Z_o$	Orbit-referenced vector set
$X_b\ Y_b\ Z_b$	Body-referenced vector set
μ_e	Reduced mass
m_A	Mass of satellite A
m_B	Mass of satellite B
μ_g	Earth gravitational constant
Q_θ	In-plane non-conservative forces
Q_ϕ	Out-of-plane non-conservative forces
Q_L	Tether non-conservative forces
ξ_B	Non-dimensional anodic tether segment length
ξ_D	Non-dimensional offset from anodic end of tether
ξ_{COM}	Non-dimensional length to tether centre of mass
I_{ch}	Characteristic tether current
E_t	Motional electric field along tether
q_e	Electron charge
m_e	Electron mass
m_i	Ion mass
N_e	Electron plasma density
v_{HC}	Non-dimensional cathode potential drop
i_{av}	Average non-dimensional tether current
ρ_0	Reference atmospheric density
h_0	Reference altitude
C_d	Coefficient of drag
H	Atmospheric scale height
r_{earth}	Earth radius
ω_{earth}	Earth angular rate
B_S	Earth surface magnetic field strength
E	Young's modulus of elasticity
A_0	Reference tether cross-sectional area
L_0	Reference tether length
Γ	Tensile tension
V	Potential energy
T	Kinetic energy
α	Angle of view
f	Focal length
Φ_v	Luminous flux
E_v	Illuminance

Abbreviations:

EDT	Electrodynamic Tether	UART	Universal Asynchronous Receiver/Transmitter
OML	Orbit Motion Limited		
ADCS	Attitude Determination and Control System	CMOS	Complementary Metal-Oxide-Semiconductor
EKF	Extended Kalman Filter	RGB	Red-Green-Blue
VHDL	VHSIC Hardware Description Language	SCCB	Serial Camera Control Bus
		SRAM	Static random-access memory
VHSIC	Very-High-Speed Integrated Circuits	OBC	On-Board Computer
FPGA	Field Programmable Gate Array	MCU	Microcontroller
		LEO	Lower Earth Orbit
GUI	Graphical User Interface	ISS	International Space Station
LED	Light Emitting Diode	PC	Personal Computer
RAAN	Right Ascension of the Ascending Node	DC	Direct Current
		AC	Alternating Current
COM	Centre of Mass	INA	Instrumentation Amplifier
IGRF	International Geomagnetic Reference Field	OPAMPS	Operational Amplifiers
		PCB	Printed Circuit Board
IAGA	International Association of Geomagnetism and Aeronomy	MSB	Most Significant Bit
		LSB	Least Significant Bit
		AEC	Automatic Exposure Control
DCM	Direct Cosine Matrix		
GPS	Global Positioning System	AGC	Automatic Gain Control
FOV	Field Of View	AWB	Automatic White Balance
AOV	Angle Of View	ABLC	Automatic Black-Level Calibration
RMS	Root-Mean-Squared		
BLDC	Brushless Direct Current		

Table of Contents

List of Figures

1 Introduction

1.1 Purpose of this Study

The concept of space tethers has been around since early 1960 when Yuri Artsutanov, a Russian engineer, suggested a space elevator system where a satellite would lower a tether from geo-stationary orbit onto the ground. The tether could then be used to put objects in orbit without the need for rockets. Since this idea was formulated, tethers have enjoyed attention from scientists from different fields of study. Uses for tethers in space have become abundant. Later analysis of tethers revealed that conductive tethers could be used for propulsion and power generation for satellites in space by interaction with the earth's magnetic field. This made the idea of satellites using tethers very appealing. During the first tether missions it became clear that deploying and controlling a tether in space poses many challenges.

In 1999 the concept of CubeSats was introduced by Jordi Puig-Suari and Bob Twiggs from California Polytechnic State University and Stanford University, respectively. They proposed small Nano-satellites specifically suited for experimental and educational purposes for universities and small institutions around the world. To date about 76 CubeSats have been launched. Initially CubeSats were used as a cheap way of demonstrating technologies that may prove useful for larger satellites. The potential of using CubeSats for other applications, especially when used in clusters or formations, is however, becoming clear.

Multiple ***Electrodynamic Tether (EDT)*** missions have been attempted. There are, however, still limited data and results available with regards to the evaluation of the performance of these systems. This is primarily due to the low number of successful missions. The concept therefore still has a lot of uncertainties. This study aims at contributing to the available literature about CubeSats and to contribute to the data available on the control of a tethered system. The study aims on specifically using low cost CubeSats to demonstrate and study the deployment and control of an EDT in space.

After this study, Stellenbosch University will have a better literature base on EDTs, a summary of all equations and principles governing the motion and behaviour of tethered satellites in space, a simulation environment for simulating tethered satellites, and physical components designed to suit such a tethered satellite mission. This should put the university in a better position to do a tethered satellite mission in the future.

The specific goals which are set as study outcomes are to:

- assemble a thorough literature base on EDTs,
- provide an analytical analysis of the dynamics of EDTs,
- provide an analytical analysis of the electrodynamics of EDTs,
- do a computer simulation implementing these analytical analyses,
- design a control system for a CubeSat EDT satellite mission, and
- produce experimental physical components for a CubeSat EDT satellite mission.

1.2 Scope of this Study

The focus of this study is specifically on the control of the attitude and deployment of a tethered CubeSat system, which includes both theoretical work and design and manufacturing of experimental models. The specific tasks which are set to achieve the goals of the study are discussed below.

Literature Research: Past tether missions are studied. This involved reading as much literature about past tether missions as possible and analysing data and results provided by it. By doing so, key problems associated with tether missions are identified. The solutions to these problems and the technologies developed to solve these problems are then better understood in order to be used in future missions. Specific focus is placed on EDT missions. Literature on the key theoretical parts of tether missions is collected, studied and summarised.

Theoretical modelling of system dynamics: The science and mathematics involved in understanding the dynamics of an orbiting tether are researched and studied. This includes dynamic modelling of the two-body system in orbit assuming a slack-spring tether model.

Theoretical modelling of electrodynamic current collection of an EDT: Electromagnetic modelling of the conductive tether in the earth's plasmasphere is studied by reviewing a collection of literature on the matter of ***Orbit Motion Limited (OML)*** current collection theory. From this literature, the analytical equations required to describe an EDT CubeSat mission are identified. These principles and equations are then applied to accurately model a small, lightweight CubeSat tethered system with design specifications fit for a CubeSat mission.

Formulation of a CubeSat configuration suitable for an EDT mission: A feasible concept of an EDT within a CubeSat sized satellite system is formulated. The design takes into account the size, mass, and power constraints of CubeSats.

Design of an orientation strategy for controlling a CubeSat EDT system: Different orientation strategies are studied and the approach best suited for a CubeSat mission is selected. The sensors that are needed to determine the attitude of the system to sufficient accuracy, and the actuators needed to control the attitude are identified.

Design and production of an experimental prototype of a sensor to measure the tether angle: A suitable sensor for determining the orientation of the tether system is designed and an experimental model is designed, built and tested.

Design of a reliable deployment system for a CubeSat EDT mission: Passive and active deployment strategies are studied. The focus is on a reliable release and separation mechanism and also a stable, reliable method of controlling the rest of the deployment.

Design and production of an experimental prototype of a deployment system: Experimental deployment hardware is designed, manufactured and tested. This involves a separation mechanism, deployment guidance system, and an actuation system for controlling the deployment speed.

Formulation of control algorithms for an *Attitude Determination and Control System* (ADCS) and deployment: From the mathematical models of the dynamics and electrodynamics which are set up, control algorithms are formulated and an ***Extended Kalman Filter (EKF)*** is designed to estimate the state variables describing the system.

Simulation of the entire EDT CubeSat system: A simulation environment is created in which the electrodynamic model, orbital dynamic model, sensor performance, and control algorithms are integrated to accurately simulate the behaviour of the system when in orbit.

1.3 Research Question

In essence the research question that will be answered in this study is:

Is it feasible to control a 500m tethered dual satellite mission with electronics and deployment hardware which is small, lightweight and low power enough to fit inside a 3U CubeSat, and will this system be able to demonstrate the electrodynamic effects of the EDT in the earth's magnetic field?

1.4 Document Outline

This document is divided into 6 chapters; the first being the current chapter serving as introduction. This section focuses on giving a brief description of the following 5 chapters and its subsections, providing an outline for the structure of the rest of the document.

Chapter 2: Literature Review

The literature review provides a list of documents that hold information relevant to the topic discussed in this document. Readers interested in tethered spacecraft may use this list and the brief descriptions contained therein, as a starting point to access relevant information about the topic. This may also serve as a theoretical introduction to readers aiming to read this document without having the relevant knowledge and background information about the subject.

Chapter 3: Theoretical System Description

This chapter provides a technical/mathematical introduction to the concept of tethered satellites and the operation of electrodynamic tethers in space. After the basics of the concept is discussed and illustrated, the technical modelling and -description of the system is given. The system is mathematically modelled and all forces and moments acting on the system are defined and the theoretical equations used to calculate these forces are derived with reference to relevant source literature where applicable. Sensors and actuators that may be implemented on a tethered satellite system are discussed and designed. Control algorithms and ADCS strategies are discussed and the operation of the tethered system is outlined.

Chapter 4: Hardware and Testing

To demonstrate the functionality of the key parts of the system, some subsystems were designed, built and tested. This involved designing and building electronic systems, designing and manufacturing mechanical structures, testing these systems, and implementing algorithms discussed in the theoretical section of the document. Different types of software were designed and coded. Embedded C-code was written for use on the microcontroller, ***VHSIC Hardware Description Language*** (VHDL) code was written for the ***Field Programmable Gate Array*** (FPGA) system involved in the implementation of the designed sensors, and JAVA application code was written for the ***Graphical User Interface*** (GUI) interface implemented on a ***Personal Computer*** (PC) to control and test the system. This section discusses the flow and layout of this software and gives short descriptions of the functions their individual parts have to perform.

Chapter 5: Orbital Simulation

Using the models discussed in Chapter 3 and practical designs and tests done in Chapter 4, the entire system was simulated. The simulation was done in Matlab Simulink using embedded Matlab code. The simulation consists of the application of theory discussed in this document

as well as functions and simulations imported from external sources. These external sources are referenced where applicable.

Chapter 6: Conclusions and Recommendations

All lessons learned and conclusions made after analysing the performance of the system are discussed. The design choices made in implementing the system, are analysed and discussed. Conclusions are made as to why certain designs worked better than others. The limitations of the study are discussed. Based on this, recommendations are made for future studies and improvements on the current study.

Appendices:

The appendices list literature and work that may be helpful to illustrate the workings of certain parts of the system, but which is not necessarily crucial to the understanding of the operation of the system. It thus serves as a reference source for the reader of this document.

2 Literature Review

2.1 Breakdown of System Elements

In this chapter the summary of relevant literature is listed and a description of the main topics discussed in each is given. The literature will be grouped according to which part of this study it contributes to. The five groups in which the literature on tether systems will be discussed are listed below with a description of their contents and aims.

General Information – This serves as background information on the topic or as overall guide to the basic concept of tethers and is meant to provide an introduction to the topic.

Previous Tether Missions – A list of tethered satellite missions is discussed and a short overview of the challenges identified in these missions, is given.

System Dynamics – The focus of this section is on the mathematical equations and laws that govern the motion and forces of the individual parts of the tethered system as well as the system as a whole.

Electrodynamics – The Electrodynamics of the system includes the physics governing the electromagnetic effects of a conductive wire in a magnetic field, the effects the physical design of the system have on its electromagnetic performance, and modelling of the earth's plasmasphere.

Tether and Mechanical Design – Material choices and tether shapes of EDTs, deployment mechanisms, and other structural designs form the subject of the mechanical design of the system.

2.2 Literature Study

2.2.1 General Tether Information

2.2.1.1 Tethers in Space Handbook [1]

This textbook contains a summary of previous tether missions, discusses possible future projects regarding tethers and also gives an overview of the mathematics and scientific principles of an electrodynamic tether system. The book gives an overview of both successful and unsuccessful past missions and provides scientific measurement data from these missions. It serves as a useful starting point for understanding the current state of research in this field.

2.2.1.2 Space Tethers and Space Elevators [2]

This book provides an introduction to the concept of EDTs in space as well as other applications of tethers. It provides the basic orbital physics that govern the motion of spacecraft and enables the reader to understand the fundamentals of orbiting bodies. It provides a comprehensive history of tethers as well as a description of past tether missions. It discusses different practical applications of space tethers and their value.

2.2.2 Previous Tether Missions

Of the tethered satellite missions launched, a large fraction has either failed because of tether deployment malfunction or because of other technical problems. It is, however, very clear that the deployment of the tether should enjoy a lot of focus during the design process to improve the reliability of the mission. Relevant tether missions, in which the focus was specifically on EDTs, are listed.

The first step in tethered spaceflight was studying the plasmasphere. Sub-orbital missions were done, using sounding rockets to launch measurement devices to high altitudes. These missions are discussed below.

2.2.2.1 Cooperative High Altitude Rocket Gun Experiment (CHARGE) [2]

CHARGE-1 (1983) / TPE-3

The CHARGE satellites were an international collaboration between Japan and the USA. The project started as the Tether Payload Experiment (TPE), but later evolved into a series of missions. These experiments were all launched using sounding rockets that offered a cheap alternative to launching a satellite into orbit. The objective of these missions was to get to microgravity altitudes in the ionosphere and to do experimental tests using specifically an electron gun to fire electrons into the plasmasphere. The aim was to use this mechanism to charge the one satellite relative to the other, thereby inducing a current through the tether connecting them.

Japanese rockets were used to launch the first two missions named TPE-1 and TPE-2. In both these missions the full deployment of the tether failed and the electron gun failed to fire due to battery failure.

After these two failed TPE-missions, CHARGE-1 was launched on August 8, 1983. The rocket reached an altitude of 169km where it split into two parts deploying a 418m tether. Unfortunately the electron beam failed shortly after deployment, and the experiment failed. Some experimental data was collected during the flight. Once again the battery pack was to blame.

CHARGE-2 (1985)
On December 14, 1985 CHARGE-2 was launched, containing similar equipment to CHARGE-1. The system deployed to 426m and was equipped with thruster systems to maintain tether tension. All systems operated successfully. The electron beam was fired and the beam was observed by on-board sensing equipment. Other scientific observations regarding the charge collection on the satellites were also made. The system induced a current through the tether and the mission was deemed a success.

CHARGE-2B (1992)
As identified in the CHARGE 1 mission, the tether acts as an electromagnetic antenna. This idea was used in CHARGE 2B and the electron gun was modulated in the Very Low Frequency (VLF) range to generate electromagnetic waves, which were then measured with on-board equipment. The tether was deployed to 400m and all experiments worked as planned.

2.2.2.2 Observations of Electric-Field Distribution in the Ionic Plasma:- A Unique Strategy (OEDIPUS) [2]

OEDIPUS-A (1989)
This project was another sub-orbital experiment done as a collaborative project between Canada and USA. It was launched on January 30, 1989 from Norway. The rocket was launched to an altitude of 512km and deployed a 958m conductive tether, which was a record for the longest tether in space at that time. This mission only included measuring equipment to study the ionosphere and the mission was a success.

OEDIPUS-C (1995)
In November 1995 the second OEDIPUS mission was launched from Alaska using a Black Brant XII rocket. This time the rocket reached 843km altitude and a record 1174m conductive tether was deployed, once again successfully doing ionospheric measurements throughout its life.

After the plasmasphere had been studied and understood to the level that predictions on the behaviour of tethers in space could be made, orbital missions were launched to study the applications EDTs may hold for spacecraft. The first of these missions was done from the Space Shuttle.

2.2.2.3 Tethered Satellite System (TSS) Mission on the Space Shuttle [2]

STS-46 (1992) – TSS-1

Figure 2.1: TTS-1 launched from STS-46 (left) STS-46 crew (right) [3]

In July 1992 the first 518kg TSS tether mission was launched from the STS-46 Space Shuttle. The objective was to deploy a 1.6m spherical satellite, dedicated to experiments on the plasmasphere, connected to the shuttle with a 22km tether. The mission was led by NASA. Half of the experimental payloads were built by Italy. The TSS contained cold gas thrusters which were to be used for control of the attitude of the system. During the deployment, the system encountered several deployment problems, which required the crew on-board the shuttle to retract and release the tether multiple times. The maximum deployment length reached was 256m. Eventually the crew had to give up and after multiple attempts they managed to retract the TSS and it was safely brought back to earth.

STS-75 (1996) – TSS-R

On 25 February, 1996 the next iteration of the TSS was deployed from the STS-75 shuttle mission. The mission was named TSS-Reflight. This time the deployment was successful. As the tether was deployed, tether current increased in accordance with electromagnetic theory. At 19.7km of deployed tether, the tether broke. According to analysis, the high currents flowing through the tether caused outgassing of the Nomex Nylon core the tether contained. The dense cloud of ionized particles caused by this outgassing, created a spark, which led to unexpected currents and caused the tether to melt. The mission was not deemed a failure on account of the experimental data collected and the currents induced in the tether.

After these shuttle missions, the next step was taken to launch satellites utilising tethers. The only successful EDT satellite mission that is considered to provide valuable information for this study is discussed next.

2.2.2.4 Plasma Motor Generator (PMG) Mission [2]

On 26 June, 1993 NASA and Tether Applications Inc. launched the PMG mission on the second stage of an Air Force Delta II rocket. The satellite was to deploy a 500m tether and the focus was on current collection and electrodynamic propulsion. The tether was successfully deployed and successfully demonstrated current generation and electrodynamic propulsion. It proved that the tether bias was easily reversible by on-board power sources and that the

current through the tether could easily be driven in such a way that it could provide electrodynamic propulsion. The tests lasted seven hours when the batteries failed. The satellite was in a $193km \times 869km$ orbit with 25.7 degree inclination. According to telemetry data, the separation of the satellites was done at initial speeds of 2-3m/s. The EDT generated currents of between 100mA and 300mA during daytime and 10-50mA during night time. This mission closely resembles the design in this document and is deemed an important benchmark for the performance of a tethered system. The satellite was, however, much larger than a CubeSat and could accommodate a Hollow Cathode Plasma contactor to ensure coupling to the plasmasphere. This included a 1 litre bottle of gas which was used to create a plasma cloud through the contactor. This illustrated the size of the equipment needed to produce the coupling to the plasmasphere that is required for tether currents of this magnitude. The variation in current during night and daytime did, however, prove that the limiting factor in the performance of the system was the external current collection from the plasmasphere.

2.2.2.5 Failed missions

Of all the failed tether missions, the following were identified as the main causes of failure:

- **Mechanical deployment issues**. This is the most common cause of failure for tether missions. Though the particular problem differs for different missions, the tethers tend to jam within the deployment mechanism, causing the tether to break or the system to not fully deploy.
- **Tether temperature effects.** In some cases the difference in temperature of the tether in the sunlit and eclipse parts of the orbit, causes the tether to expand and leads to mechanical failure during deployment.
- **Too large currents**. In the case of the TSS-R mission the large current flowing through the 20km tether caused it to melt and break.
- **Electronic failure**. This seems to be a problem particularly in the Nano and Pico satellite range. The causes for these failures range from battery failures to digital electronics failing because of radiation damage.
- **Tether dangers to other satellites**. In the case of the YES satellite the mission was launched in a different orbit than originally intended, because of low availability of launches. The satellite was at such a high altitude and at such an inclination, that there were concerns over whether the tethered satellites were going to hit the ISS, and the mission was aborted.
- **Micro-Debris damage**. Some reports indicated tethers breaking unexpectedly. This was attributed to micro-debris damaging the tether.

2.2.3 System Dynamics

2.2.3.1 A unification of models of tethered satellites [4]

This paper considers different models for massive tethers in space with a range of complexity. These include the slack-spring model, dumbbell model and variations of these where energy dissipation within the tether is taken into account. The different models are compared and the limitations of the simpler models are discussed. This serves as a good starting point for understanding the different approaches to modelling a tethered spacecraft system. The paper takes a strict mathematical approach.

2.2.3.2 An introduction to Lagrangian mechanics [5]

The textbook provides the necessary theoretical basis for understanding the process of mathematically modelling a system using Lagrangian principles. The book is based on notes from Saint Michaels College. It discusses the basic mathematical principles and methods needed for derivation and use of the Lagrangian equations. Many examples are discussed and the book provides all the tools to mathematically model the dynamics of the tether system that is studied.

2.2.3.3 Dynamics and control of tethered satellite system [6]

This paper considers the dynamics and control of multi and single bodied tether systems. It focuses specifically on the retrieval of a sub-satellite that is tethered to a main satellite. The theory discussed, not only provides insight into the retrieval process, but also provides valuable understanding of the analysis process of a tether system.

2.2.3.4 Optimal control of electrodynamic tether orbit transfers using timescale separation [7]

This paper was the most important piece of literature in the process of understanding the dynamics of tethered systems. It provides a well-structured mathematical derivation of the dynamics of the tether using Lagrangian principles. It then discusses the control principles used in stabilising an electrodynamic tether. The control algorithms are not only focused on the dynamics of the system, and thus the liberation angles, but also focuses on the orbital elements of the satellite system.

2.2.3.5 Passivity-Based Control of a Rigid Electrodynamic Tether [8]

This article focuses mainly on the stability of a tethered satellite system as it orbits through the varying geomagnetic field of an inclined orbit. Areas of stability are found and the performance of the system is investigated for a variety of control laws.

2.2.4 Electrodynamics

2.2.4.1 Systems Analysis of Electrodynamic Tethers [9]

The paper focuses on the modelling of the current collection and flow in electrodynamic tethers in space. It specifically focuses on bare electrodynamic tethers. The paper provides the necessary equations to calculate the current profile along the tether and efficiencies of the tether operating in generator and thruster modes. It also discusses the optimal altitudes and orbits for electrodynamic tethers to function at optimal efficiency. Anodic contactors are discussed and the concept of the bare EDT is introduced and studied. The hollow cathode contactor and its related theory is discussed. According to this study the optimal altitude for an EDT is roughly 300km and is governed by a trade-off between electron density and geomagnetic field strength. It also discusses the efficiency of an EDT system acting as a thruster or a generator. It concludes that there exists an optimal fraction of a tether that should be bare for maximum efficiency.

2.2.4.2 Asymptotic Solution for the Current Profile of Passive Bare Electrodynamic Tethers [10]

The article focuses on deriving an analytical solution to the electrical current flowing through an EDT. This is beneficial in the sense that the analytical solution can be used in control algorithms and in simulations without the need for access to complicated numerical models for solving these electrical currents. This is done at the expense of accuracy, but the article also demonstrates how the analytical solution provides sufficient accuracy when used within specified operating conditions. From this derived current profile, the analytical solutions for the Lorentz forces and moments are derived.

2.2.4.3 Performance Analysis of Bare Electrodynamic Tethers as Microsat Deorbiting Systems [11]

The EDT as deorbiting device is studied with specific focus on CubeSats. The electromagnetic performance of such a system is studied and calculations on the orbital decay of such a tethered CubeSat system are discussed. Issues regarding the deployment and operation of such a system are also studied.

2.2.4.4 Electrodynamic Tether Propulsion and Power Generation at Jupiter [12]

This is an article published by NASA which focuses on the uses and performance of an EDT in orbit around Jupiter. Jupiter has magnetic characteristic that makes it particularly favourable for an EDT system. The study predicts propulsion forces of up to 50 N and power generation of up to 1MW for an EDT system in such an orbit. Dynamics and performance of a 1mm tether orbiting in these conditions are modelled and simulated.

2.2.5 Tether and Mechanical Design

2.2.5.1 Using LEDs for Inter-Satellite Links [13]

When light travels through space, there is no need to contend with atmospheric scattering, rain fade and other physical losses and the only significant loss is free space loss. Using ***Light Emitting Diodes*** (LED) in space thus seems like a viable technology for example inter-satellite communications. In this article this idea is discussed and an example is given of a 1W LED with Fresnel lenses providing communication over 160km. Other examples are also discussed and importantly, the situation of seeing the LED against the brightness of the sun, is discussed. This involves using LEDs in the frequency range which falls under the Fraunhofer absorption frequencies. These are narrow dead bands in the sun's frequency spectrum. This study is of importance for the possible use of a LED for implementing the sensor for measuring the tether orientation angles.

2.2.5.2 CubeSat Tether System [14]

This is a Project Definition Document of a project that focuses on building a 3U tether system much like the one studied in this project. The document provides an example of how such a CubeSat project can be approached in terms of the logistics and project management. The

project lists clear performance measures by which the tether mission's success can be measured.

3 Theoretical System Modeling

3.1 Concept of Operations

An overview of the concept of tethered spacecraft is discussed in this section. The different components of the concept are discussed and explained through graphical illustrations and diagrams. Each subsection contains a distinguishable part of the workings of the system. The purpose of this section is to familiarise the reader with the principles underlying the dynamics of a tethered system in space, and to explain how such a system operates and how it can be of practical use.

3.1.1 Tethered Satellites and Gravity Gradient

The simplest form of describing the motion of a body orbiting another is by use of a Kepler orbit. The Kepler orbit considers only the gravitational effect the two bodies have on each other to describe their motion, thus excluding external forces and perturbations acting on the

system. For simplicity, in this document, the focus will be on circular orbits. In these orbits the orbital velocity is constant and is only a function of the orbit radius. The position of the body in its orbit can be described by the parameters defined in Figure 3.1

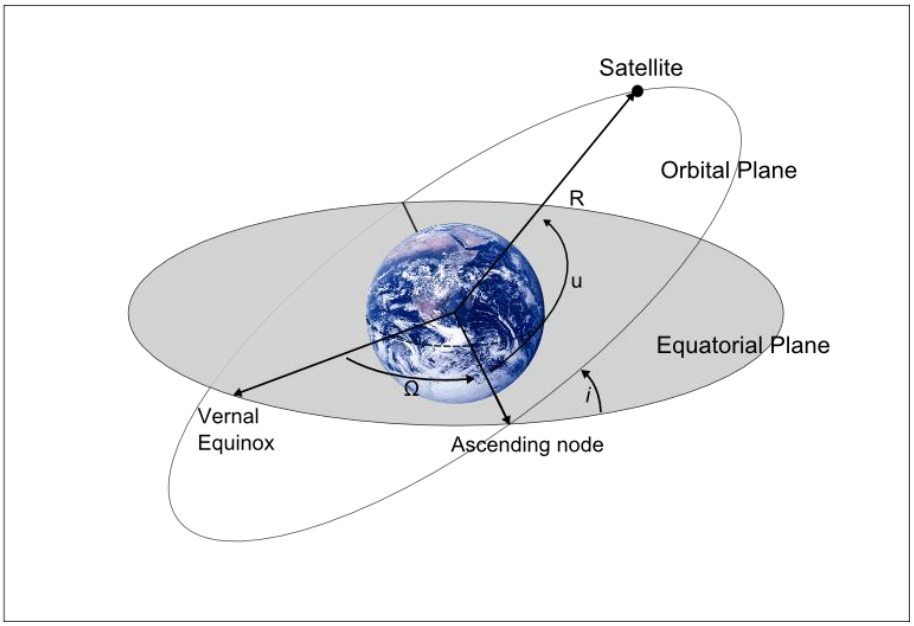

Figure 3.1: Illustration of orbital elements for a circular orbit

The key parameters describing the circular orbit are

Ω the **Right Ascension of the Ascending Node (RAAN),**

i the inclination,

u the argument of latitude, and

R the orbit radius.

When two bodies moving in different orbits at different altitudes are connected with a tether the motion of the two bodies becomes connected. Instead of having two separate velocities describing the motion of the two bodies, only one velocity then describes the motion of the **Centre of Mass (COM)** of the system and the relative motion of the two satellites is described with relative angles and velocities as illustrated in Figure 3.2. The pair then forms a connected system and external forces acting thereon affect both bodies indirectly.

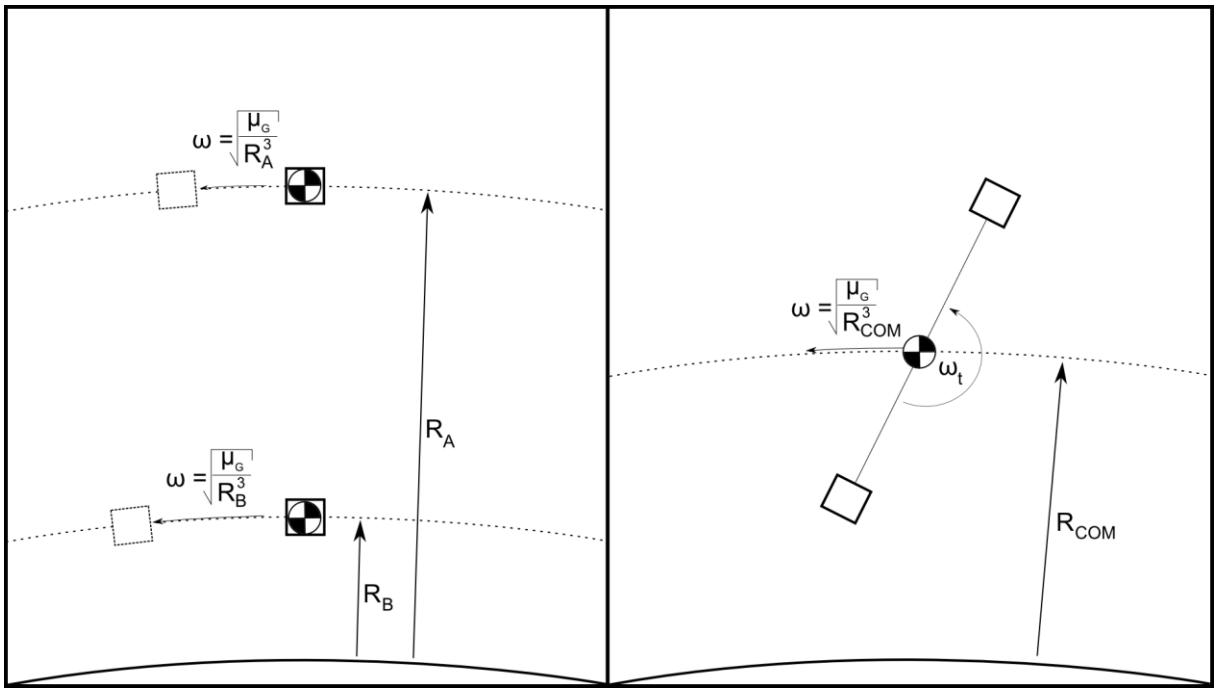

Figure 3.2: Individual versus tethered motion of two bodies

The fact that the two bodies are in orbits with different altitudes, necessarily means that they will move apart with time because they have different orbital velocities. The tether connecting the two bodies essentially places a constraint on the maximum distance between the two bodies. The tether will thus always have to place some constraining force on the two bodies to keep them moving together.

The force keeping a moving body in orbit around the earth is the gravitational force (F_G) of the earth on the body. However, if the body is not moving and the gravitational force is the only force on the body, it will simply fall to the earth. The movement of the body thus plays a key role in keeping it in orbit. The counter-acting force that prevents the body from falling to earth is the apparent centrifugal force. It is described as an apparent force because in fact, it is more a manifestation of the body's linear momentum as a resistance against changing its velocity. For simplicity, it will be referred to as a force for the rest of this section.

When a system is in a circular orbit, the centrifugal force equals the gravitational force, keeping the body orbiting at a constant distance from earth. When the two-body tethered system is in such a circular orbit, the centrifugal and gravitational force on its COM is thus constant and equal.

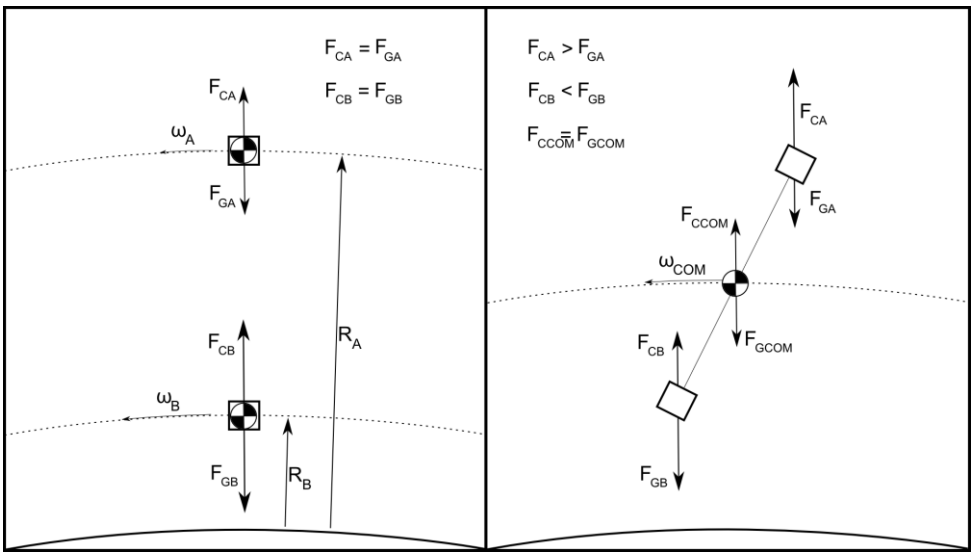

Figure 3.3: Individual versus tethered orbital forces of two bodies

When each body is considered individually, the forces in the Nadir (Towards from earth) and Zenith (Away from earth) direction must also cancel out each other in order for the bodies to maintain their constant altitude. Even though the linear velocities of the bodies may differ, the angular rate at which the two bodies orbit earth, must be equal considering that it is moving as a unit. Using this equal angular rate, the centrifugal and gravitation forces on a body in orbit can be calculated using Equations (1) to (3). This is illustrated in Figure 3.3.

For a body *i* at altitude *h*, the orbital rotational velocity ω_i is

$$\omega_i = \sqrt{\frac{\mu_{eart\,h}}{r_i^3}} \tag{1}$$

where $r_i = r_{eart\,h} + h$.

The magnitude of the centrifugal force in terms of this angular rate is

$$F_{Ci} = m_i \omega_i^2 r_i \tag{2}$$

and the magnitude of the gravitational force is

$$F_{Gi} = \frac{\mu_{eart\,h} m_i}{r_i^2} \tag{3}$$

For simplicity, the body in the orbit with higher altitude will be referred to as Body A and the body with lower altitude as Body B. Body A has a larger rotational radius than the lower Body B. From Equation (2) the conclusion can be made that A has a higher and B has a lower centrifugal force than the COM, because of their higher and lower altitudes. Similarly, from Equation (3) the conclusion can be made that A has a lower and B has a higher gravitational force than the COM, because of their higher and lower altitudes. The result is that the net force (excluding the tether tension) is Zenith on body A and Nadir on body B. To keep the

bodies moving together, with the distance between them constrained to the length of the tether, the tether has to exert some constraining force on both bodies. The tether has to exert the force needed for the net radial force on the bodies to be zero. This force resulting from the difference in altitude and thus the difference in gravitation force on the two bodies is called the Gravity Gradient force (F_{GG}). From equations (2) and (3), the gravity gradient force on body i with rotational radius r_i in a tether system with a COM with rotational radius r_{COM} is

$$F_{GGi} = F_{Ci} - F_{Gi}$$

$$= m_i \omega_i^2 r_i - \frac{\mu_{eart\,h} m_i}{r_i^2}$$

$$= \mu_{eart\,h} m_i r_i \left(\frac{1}{r_{COM}^3} - \frac{1}{r_i^3} \right) \quad (4)$$

The centrifugal and gravitational forces are always in the Nadir direction, so when the direction of the tether is not Nadir, the gravity gradient forces result in a moment rotating the system towards the Nadir direction creating an equilibrium point which simplifies the stabilisation of the system.

3.1.2 Earth Magnetic Field

Electromagnetic tethers rely on the magnetic field generated by the earth's spinning core to provide the magnetic flux needed to generate a current. A simple model of the fundamental magnetic field of the earth is a dipole tilted roughly 11º from the earth's rotational axis. The actual magnetic field around the earth is, however, perturbed and imperfect. For the purposes of this section and for initial calculations on the control of the EDT, a perfect non-shifted non-tilted dipole model is assumed. This model is illustrated in Figure 3.4.

In Section 5.1 the entire system is simulated and perturbations are inserted in the model by using the ***International Geomagnetic Reference Field*** (IGRF) model. This is a collaborative international project, led by the ***International Association of Geomagnetism and Aeronomy*** (IAGA), which integrates magnetic measurements done by institutions from around the world to do a spherical harmonic expansion of the magnetic potential of the earth. This model and its coefficients are available online [15].

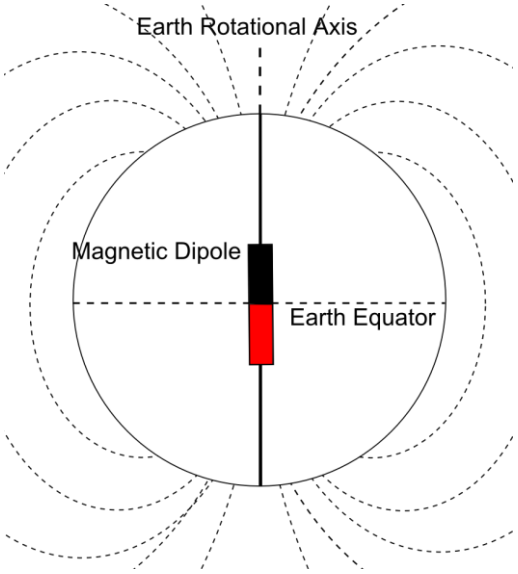

Figure 3.4: Tilted dipole model of earth magnetic field

3.1.3 Motor and Generator Rule and an Electrodynamic Tether

The electrodynamic force on the tether moving through the geomagnetic field is easily described applying Flemming's left and right hand rules which are illustrated in Figure 3.5

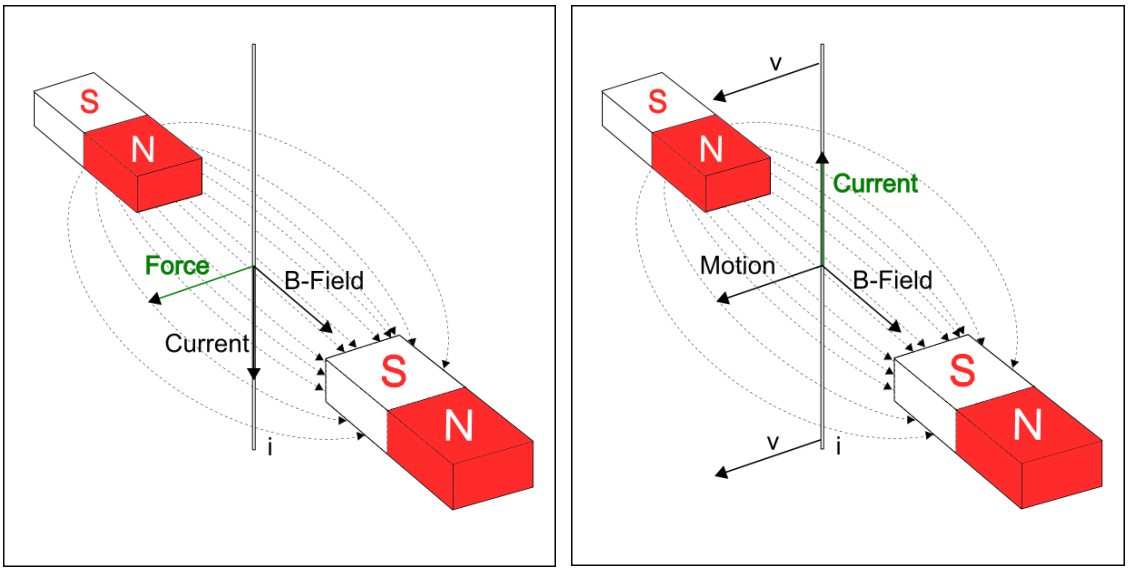

Figure 3.5: Flemming's motor and generator rule

The right hand generator rule states that a conductive wire moving in a magnetic field directed orthogonal to the wire, causes a current in the wire. The underlying theory is described by Faraday's laws. The more detailed physics are discussed in depth in Section 3.3.6.2 where the force on the EDT is calculated. When the tether moves through the magnetic field of the earth, according to the generator rule, a potential is created across the tether causing a current proportional to the component of the magnetic field orthogonal to the tether motion and orientation.

When a large enough potential is forced over a tether by a voltage source at one end of the tether in the opposite direction of the current flow just discussed, a current will be forced in the opposite direction. This current, interacting with the magnetic field, will cause an orthogonal force on the tether as in the motor rule.

In this way the tether can either be used as a power generating device as with the generator rule, or as a propulsion device as in the motor rule.

3.1.4 Completion of the Electric Circuit

In conventional electronics circuits are completed by conductive wires. In the case of the EDT, this is not possible. If the tethered system were to have two wires between the two bodies, with current flowing up in the one wire and down in the other, the effect of the one wire will be cancelled by the current flowing in the opposite direction in the other and no resulting force will be possible, thus defeating the purpose of the tether.

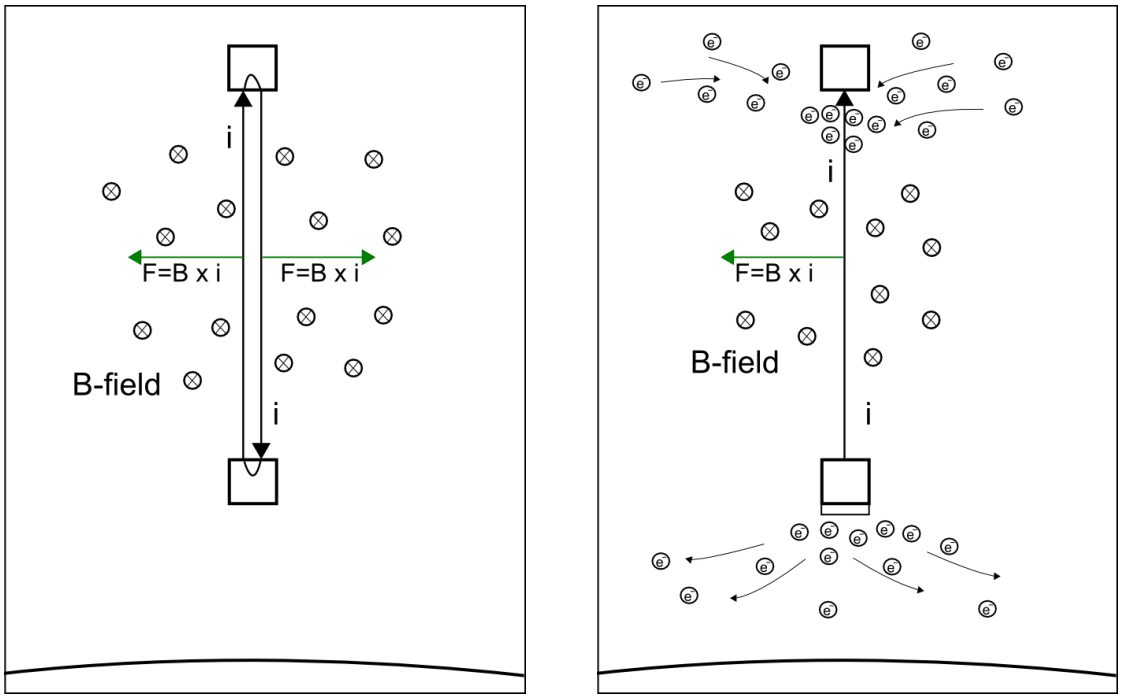

Figure 3.6: Completion of tether circuit in space

The solution to this problem relies on the fact that there are enough free electrons and ions in LEO to 'complete' the circuit. The anode of the tether attracts electrons and collects them through the bare EDT. On the other end of the tether a cathodic plasma contactor is needed to attract free positively charged hydrogen (H^+) and Oxygen (O^{2+}) ions from the surrounding ionosphere to expel electrons flowing towards that end of the tether. Classically, contactors were inserted at both ends of the tether, but the concept of a bare EDT as anodic collector was introduced by Sanmartin et al [16] and have been proved by many (e.g. [9]) to be more efficient than an anodic contactor. The trade-off when making this choice is the increased efficiency the contactor offers, but the decreased mass using only the bare EDT offers.

This mechanism then requires only one tether, which makes it possible for a net force/current to be generated on the system. A key part of optimising the tether system is maximising this electron collection from the local surrounding plasma. A good design is to use a bare tether and a plasma contactor at only the cathodic end of the tether. The key measure of performance of this contactor is the potential drop over it when current is flowing through the tether. This is further discussed and a suitable plasma contactor is chosen in Section 3.3.6.2 dealing with the electrodynamic force on the EDT. Adding a contactor at the other anodic part of the tether may increase the electron collection of the tether which may boost the performance. The increase in performance does, however, not outweigh the increase in mass needed for the contactor, and the system is most efficient with only a contactor at the cathodic end of the tether [9].

3.1.5 Uses of the EDT

The potential of tethers is undoubtedly large. Ways of harnessing this potential are still few because of practical challenges set by the complicated dynamics of tether systems and the difficulty of controlling such a system. With more tether missions launched and especially with the opportunities small CubeSat missions are providing, the day where tethers will be used on many satellites to provide mission critical functions, is near.

One of the most promising and most practical uses for tethers is for deorbiting. With the requirements for passive end of life deorbiting devices increasing, tethers may soon be used in many satellites as a deorbiting device. The idea is that a tether can be stored within a small part of a satellite and deployed at end of life for deorbiting. The Lorentz force generated by the electromagnetic tether then continuously decelerate the satellites, lowering their orbit until they are further deorbited by aerodynamic drag [11].

EDTs can theoretically generate a lot of power with up to 40kW for tethers with 20km length [2]. This power generated by the tethers can be put through a load, which may be a battery, to provide power to the satellite to function. The advantage of using such an EDT power system is the fact that it can generate power even if in eclipse, in contrast with traditional solar panels which provide power only in the sunlit part of the orbit.

The forces a tether can generate can be controlled by controlling the current through the EDT. When the tether moves through the earth's magnetic field with only a load connected to the tether, a current will flow through the tether that will convert the satellite's motion into electrical energy, which is absorbed in a load. The satellite system's orbital energy is therefore lowered. The reverse is also true. If a large enough potential is placed across the tether to overcome the bias caused by electromagnetic effects, the current will flow in the opposite direction, causing a propulsion force on the satellite system. Using these two modes of the system, the orbit of the system can be controlled and the tether may serve as alternative for traditional fuel thrusters. There have been suggestions to use this method to do orbit maintenance for the ***International Space Station*** (ISS) [17].

A special case for using a tether for propulsion is using it in orbit around Jupiter. In contrast with the earth, the ion density around Jupiter is still high enough to enable the functioning of EDTs even at altitude higher than the geostationary altitude of the planet. When the orbiting satellite is at a higher altitude than the geostationary altitude, the relative motion of the corotating plasma surrounding the planet to the tether is in the direction of the satellite's motion. This means that power can be generated while the satellite's orbit is maintained. The propulsion force can simply be controlled by controlling a load connected to the tether, thus controlling the induced current in the tether. Such a system can for instance be used to study the surface of Jupiter remotely or even to do atmospheric measurements in low orbit. The magnetic field can be used to overcome aerodynamic drag and a tethered satellite system can orbit at low altitude around Jupiter without the need for a propulsion system [12] [2].

There is still much to learn about the earth's own atmosphere. Projects such as QB50 which aim to study exactly this environment are proof of this [18].The magnetic field around the earth is something that is constantly perturbed by the sun and shifts in the earth's magnetic dipole. Measurements are continuously taken to update models of the magnetic field to be used by other missions. The earth's gravitational field is also studied for a variety of reasons. The atmosphere itself and the particle densities in it are also a priority for many scientists. For many of these studies, differential measurements done in orbit are needed. Tethers provide the perfect mechanism for doing this. With a fixed tether length, differential measurements can be done at a constant distance between the measurement apparatus. More important are the experiments where measurements have to be done at altitudes below 300km. Satellites experience very large atmospheric drag at this altitude, causing them to deorbit within days. Satellites dedicated for experiments at this altitude therefore have a very short lifespan. Tethers can provide a solution to this problem. Theoretically a very large main satellite can be launched in a higher orbit with a smaller satellite dragging through the atmosphere for experimental tests. In this way, experiments can be done at low altitude while the satellites are at a high enough altitude to provide a decent lifespan. If the length of the tether can be controlled, the height at which it does measurements can also be changed by simply reeling in the tether.

3.2 Satellite Configuration and Orbit Selection

3.2.1 Satellite Structure and Size

The proposed design for the satellite to carry the tether system is done based on the CubeSat form factor. The CubeSat standard defines a unit used for measuring the size of a CubeSat. CubeSats are defined in terms of an amount of 'U's, where a 1U is $100mm \times 100mm \times 100mm$, a 2U is $200mm \times 100mm \times 100mm$ etc. The suggested satellite will fall in the classification of a 3U CubeSat. The satellite is seperated into two halves, namely the main satellite, and the payload satellite. The main satellite consists of a 1.5U satellite dedicated to the tether mission containing the tether deployment system, the tether angle sensor, a miniaturised three axis reaction wheel ADCS system combined with torquer-rods and other standard satellite subsystems such as an ***On-board Computer*** (OBC), power unit and orientation sensors.

The payload satellite consists of 0.5U dedicated to the tether system and 1U dedicated to a payload CubeSat. The ADCS design in this study focuses on the control of the tether angle, which is measured as the angle the tether makes with the Nadir vector, and it focuses on the ADCS of the main satellite. The payload satellite also requires an ADCS strategy, but this is left for when the design and mission of the final payload is done. The orientation of the tether is measured by the main satellite and this measurement requires the main satellite to point to a fixed orbital reference such as the Nadir vector. The only requirement from the payload satellite for the sensor to function is that it should be visible from the sensor on the main satellite. This does not require a specific body orientation from the payload satellite and is further discussed in Section 3.4.1.1. The rotation of the payload satellite is, however, constrained from completing full rotations in any of its axes since this would cause the tether to either wind around the satellite, or to wind around its own axis and eventually break.

3.2.2 Orbit Selection

The orbit selection for the proposed tether mission is done based on the opportunities it would provide in terms of an experimental payload. As discussed in the previous section, the satellite would provide a 1U payload space for experiments. As explained in Section 3.1.5, atmospheric tests are scientifically valuable and a relatively low orbit of 350km altitude was selected to provide the opportunity for a science payload to be added. This orbit selection is also favourable for EDTs since it offers a balance between geomagnetic field strength and electron-density, and atmospheric density. This balance and performance efficiency of EDTs has been studied and an altitude of roughly 300km were found to be optimal [9].

An equatorial orbit was selected. This inclination is preferable, because of the high number of launch opportunities available. An equatorial orbit also provides a maximum motional electric field across the tether considering the fact that the geomagnetic field, the motion of the tether, and the orientation of the tether are orthogonal.

3.3 System Modelling and Dynamics

The mathematical description of the orientation, dynamics and the electromagnetics of the system is done in this section. The reader will gain an understanding of the fundamental forces acting on the system by considering the energy of the system and mathematical models of the environment surrounding the tether. The mathematical methods employed in this section are also briefly discussed and explained.

3.3.1 Variables Describing the Closed System

When computing the movement of the tethered system in its orbit, the system can be replaced by an object with the mass and inertia of the total system placed at the system's COM. The control of the parts within the system is, however, a more complex multi-body problem, with many variables describing the state of the system. The significant variables are described in Figure 3.7.

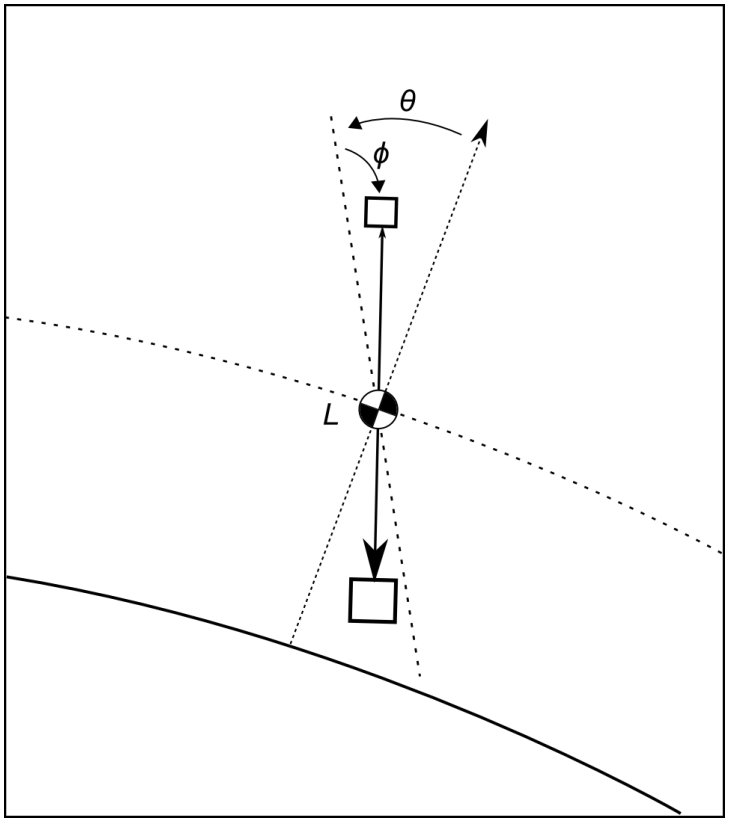

Figure 3.7: System variable definitions.

The variables are defined as:

- the in-plane angle θ is the angle from the Nadir direction within the orbital plane,
- the out-of-plane angle ϕ is the angle from the Orbital plane to the tether, and
- the length L is the distance between the two satellites.

These three variables will form the key set of parameters describing the state of the system at any given time. An important fact to note is that the rotation axis in the direction of the tether is not considered in this definition. The reason for this is two-fold. Firstly the inertia of the system in this axis is much smaller than in the other two axes where the mass of the satellites is spread over the distance of the tether. Secondly, the relative rotation of the satellites in this direction does not lead to the satellites influencing each other through the tether, considering the long length and small thickness of the tether. The long and thin tether may wind up if the satellites rotate relative to each other, but the torque it will transfer, will be insignificant.

3.3.2 Forces and Moments

To proceed with the analysis of the dynamics within the system, all forces and moments must be identified. These forces can initially be listed intuitively. (See Figure 3.8)

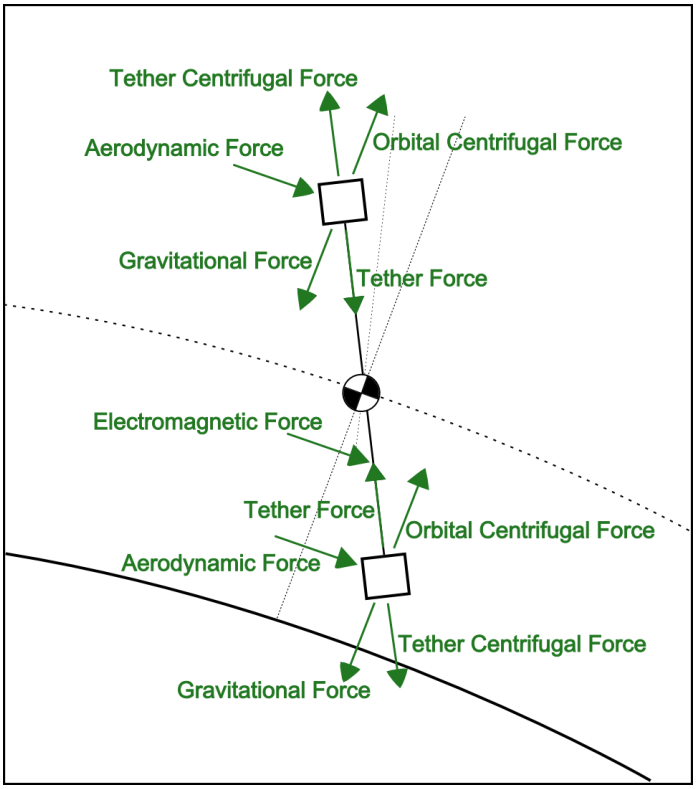

Figure 3.8: Forces acting on a tethered system.

The forces can be classified into two categories, namely the conservative and non-conservative forces. Conservative forces are forces that store their energy, whereas non-conservative forces are forces which dissipate energy. An example of a conservative force is gravity, which is the main force governing the relative motion of the two bodies.

Writing Newtonian equations describing the total force and moment on the system are complex because of the number of forces acting on the system and their dependency on all three system variables. A simpler method to model the system is therefore required.

3.3.3 Motivation for using the Lagrangian Approach

An alternative solution to using these Newtonian equations is the Lagrangian approach. The Lagrangian method focuses on the energy of the system and uses the law of conservation of energy to constrain the total energy of the system and so derives the equations of motion of the system. These are two methods to derive the same equations; the Lagrangian is just the preferred method.

Apart from the fact that handling the large number of forces is easier with the Lagrangian approach, it is also more convenient for simulation purposes. The Lagrangian focuses specifically on all conservative forces and outputs the dynamic equations of the system irrelevant of external non-conservative inputs on the system. The non-conservative forces are then later individually added. This suits the simulation approach where the dynamic equations derived using the Lagrangian, form the basic black box model of the system, considering only the gravitation forces governing the orbital motion of the satellite. External non-conservative forces are then fed in from models. This separates the individual parts of the system in a way that it can be kept modular as illustrated in Figure 3.9.

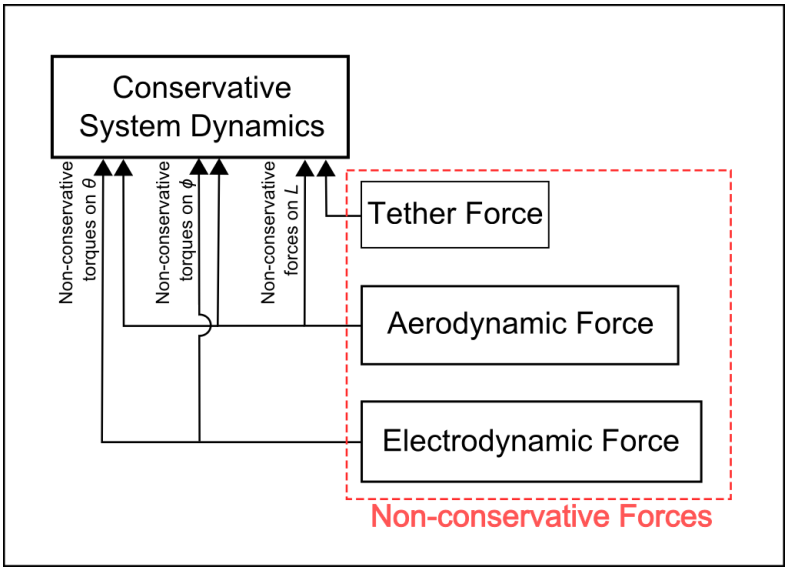

Figure 3.9: Modular structure of Lagrangian equations.

3.3.4 Energy of the System

To calculate the equations of motion of the system, the kinetic and potential energy of the entire system are formulated below. To do this, some vectors are defined in Figure 3.10.

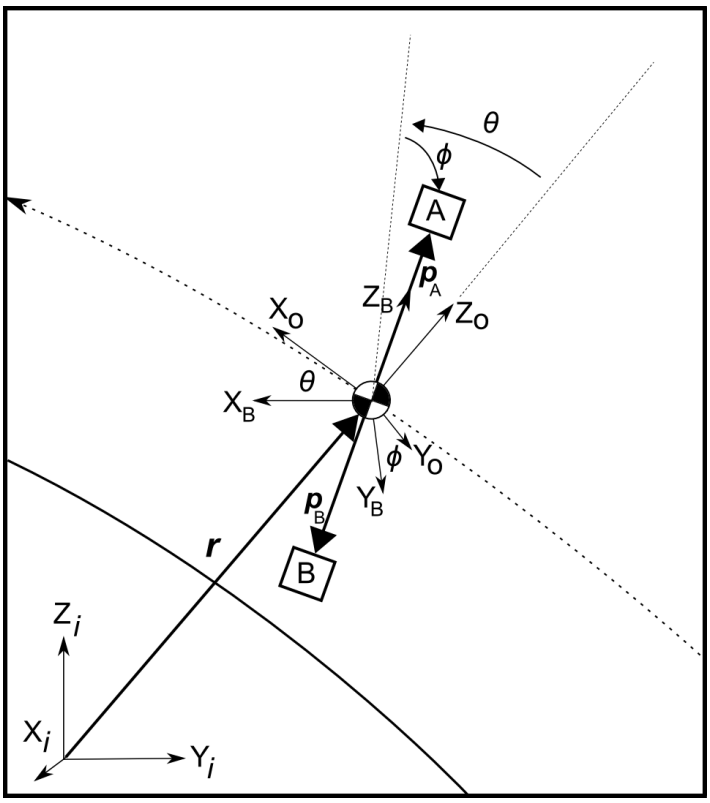

Figure 3.10: Vector definitions for deriving equations of motion.

The key definitions made here are

- $\boldsymbol{X_i, Y_i, Z_i}$ form the orthogonal inertial vector set
- $\boldsymbol{X_o, Y_o, Z_o}$ form the orthogonal orbital vector set
- $\boldsymbol{X_b, Y_b, Z_b}$ form the orthogonal body vector set
- $\boldsymbol{p_B}$ is the vector from the COM to satellite A and is also written as $\boldsymbol{p_B} = -p_B \hat{\boldsymbol{e}}_{\boldsymbol{p}}$
- $\boldsymbol{p_A}$ is the vector from the COM to satellite B and is also written as $\boldsymbol{p_A} = p_A \hat{\boldsymbol{e}}_{\boldsymbol{p}}$
- $\boldsymbol{r}$ is the vector from the centre of the earth to the COM

3.3.4.1 Kinetic Energy

The total kinetic energy of the system is the sum of the kinetic energies of its separate massive parts, namely body A, body B and the tether. The kinetic energy of the tether is calculated by integrating along the tether, assuming uniform mass distribution.

After simplifications, the final kinetic energy of the system can be written as [7]

$$T = \frac{1}{2}M\dot{\mathbf{r}}\cdot\dot{\mathbf{r}} + \frac{1}{2}\mu_e\left(\dot{L}^2 + L^2(\boldsymbol{\Omega}\times\hat{\boldsymbol{e}}_{\boldsymbol{p}})\cdot(\boldsymbol{\Omega}\times\hat{\boldsymbol{e}}_{\boldsymbol{p}})\right) \tag{5}$$

where

M is the total mass of the system

μ_e is a reduced mass term

$\boldsymbol{\omega_0}$ is the orbital angular rate of the system

$\boldsymbol{\omega_e}$ is the tether angular rate, and

$\boldsymbol{\Omega = \omega_0 + \omega_e}$.

The reduced mass term μ_e is written as [7]

$$\mu_e = \frac{\left(m_A + \frac{m_T}{2}\right)\left(m_B + \frac{m_T}{2}\right)}{m_A + m_B + m_T} - \frac{m_T}{6} \tag{6}$$

where

m_A and m_B are the masses of the two bodies

and m_T is the mass of the tether.

3.3.4.2 Potential Energy

The potential energy of the system is purely gravitational potential energy. Once again the sum of the parts of the system is considered and the mass of the tether is integrated along the tether to obtain the total potential energy. During the derivation of this term, the distance to each body and each integration-element of the tether had to be computed. To do this, an approximation of the square root operator was made by writing it as a second order binomial expression.

The total potential energy is then written as [7]

$$V = -\frac{\mu_g M}{R} - \frac{\mu_g L^2}{2R^3}\mu_e\left(3(\hat{\boldsymbol{e}}_{\boldsymbol{p}}\cdot\hat{\boldsymbol{e}}_{\boldsymbol{r}})^{\mathbf{2}} - 1\right) \tag{7}$$

where

μ_g is the gravitational constant.

3.3.5 Equations of Motion

The Lagrangian equation of motion can now be constructed by using Equations (5) and (7).

$$\mathcal{L} = T - V = \frac{1}{2}M\dot{\mathbf{r}}\cdot\dot{\mathbf{r}} + \frac{1}{2}\mu_e\left(\dot{L}^2 + L^2(\boldsymbol{\Omega}\times\hat{\boldsymbol{e}}_{\boldsymbol{p}})\cdot(\boldsymbol{\Omega}\times\hat{\boldsymbol{e}}_{\boldsymbol{p}})\right) + \frac{\mu_g M}{R} + \frac{\mu_g L^2}{2R^3}\mu_e\left(3(\hat{\boldsymbol{p}}\cdot\hat{\boldsymbol{e}}_{\boldsymbol{r}})^{\mathbf{2}} - 1\right) \tag{8}$$

The benefit of using the Lagrangian approach is the convenience of easily getting the equations of motion in terms of the defined variables θ, ϕ, and L that defines the state of the system. Equation (8) must thus be rewritten in terms of these variables. To do this, all vectors defined in Figure 3.10 must be written in terms of the system variables and in the same reference frame. The body reference frame was chosen to do the calculations in. To write all vectors in the body frame, the unitary transform ***Direct Cosine Matrix*** (DCM) is constructed to rotate the orbit reference frame to the body frame.

$$\boldsymbol{DCM} = \begin{bmatrix} cos\theta & 0 & -sin\theta \\ sin\phi sin\theta & cos\phi & sin\phi cos\theta \\ cos\phi sin\theta & -sin\phi & cos\phi cos\theta \end{bmatrix} \tag{9}$$

The Lagrangian is rewritten and simplified to

$$\mathcal{L} = \frac{1}{2}Mv^2 + \frac{1}{2}\mu_e\left(\dot{L}^2 + L^2\left(\dot{\phi}^2 + \cos^2(\phi)\left(\dot{\theta}+\dot{v}\right)^2\right)\right) + \frac{\mu_g M}{r} + \frac{\mu_g\mu_e L^2}{2r^3}(3cos^2(\phi)cos^2(\theta) - 1) \tag{10}$$

The equations of motion of θ, ϕ and L can now be derived. To do this, the Euler-Lagrange equation is used. For a Lagrangian function with continuous partial derivatives for a variable ψ and $\dot{\psi}$, the Euler-Lagrangian equation can be written as [19]

$$\frac{d}{dt}\left(\frac{\partial\mathcal{L}}{\partial\dot{\psi}}\right) - \frac{\partial\mathcal{L}}{\partial\psi} = Q_\psi \tag{11}$$

where

Q_ψ is the non-conservative forces acting on the system.

When applied to the system variables, the following three equations are derived. Terms for the orbital acceleration were discarded because of the assumption made of a circular orbit.

$$\mu_e L^2 \left(cos^2\phi\ddot{\theta} + 2\left(\frac{\dot{L}}{L}cos^2\phi - \dot{\phi}cos\phi sin\phi\right)(\dot{\theta}+\dot{v}) + \frac{3\mu_g}{r^3}cos^2\phi cos\theta sin\theta \right) = Q_\theta \qquad (12)$$

$$\mu_e L^2 \left(\ddot{\phi} + 2\frac{\dot{L}}{L}\dot{\phi} + cos\phi sin\phi \left((\dot{\theta}+\dot{v})^2 + \frac{3\mu_g}{r^3}cos^2\theta \right) \right) = Q_\phi \qquad (13)$$

$$\mu_e L \left(\frac{\ddot{L}}{L} - \dot{\phi}^2 - cos^2\phi(\dot{\theta}+\dot{v})^2 - \frac{\mu_g}{r^3}(3cos^2\phi cos^2\theta - 1) \right) = Q_L \qquad (14)$$

The non-conservative forces Q_θ, Q_ϕ and Q_L acting on the system are discussed in the following section.

A Matlab script was written which does the Lagrangian derivation using the Matlab symbolic toolbox. The DCM defined in Equation (10) was used to convert vectors to the body reference frame. The code for the Matlab script is shown in Appendix A.4.

3.3.6 Non-conservative Forces

3.3.6.1 Aerodynamic Drag

One of the main external forces on a satellite in ***Lower Earth Orbit*** (LEO) is aerodynamic drag. At 350km altitude the atmospheric density is about 10^{12} times smaller than on the surface of the earth, but considering that a satellite in a circular 350km orbit moves at over 7km/s, the effect of drag on satellites is significant.

For the case of tethered satellites, aerodynamic drag has two major effects in the orientation of the system. Firstly, the tether will typically form a bulge, and secondly, for long tethers, the equilibrium position of the tether (which is normally Nadir) shifts to a slight angle. The reason for this shift is based on the fact that the atmospheric density in space decreases exponentially with altitude. If the two satellites have similar geometry, the lower satellite of the tethered satellite pair is at a lower altitude with higher atmospheric density, and thus has higher drag.

The atmosphere density ρ can be approximated as an exponential function. If we assume a certain atmospheric density for the bottom satellite, the atmospheric density at the top satellite can be calculated using the following equation [20]

$$\rho = \rho_0 e^{\frac{-(h+h_0)}{H}} \tag{15}$$

where

ρ_0 is the reference atmospheric density $[kg \cdot m^{-3}]$

h is the altitude $[km]$

h_0 is the reference altitude $[km]$

and H is atmospheric scale height. $[km]$

Once the atmospheric density is known, the aerodynamic force on the satellites can be determined.

$$\boldsymbol{F} = -\frac{1}{2} C_d A \rho v \boldsymbol{v} \tag{16}$$

where

C_d is the coefficient of drag

A is the projected area of the body in the direction of the velocity of the body $[m^2]$

and $\boldsymbol{v}$ is the velocity of the body relative to the atmosphere. $[m \cdot s^{-1}]$

The velocity of the tether to the surrounding atmosphere is dependent on the satellite orbital speed as well as the speed of the earth's co-rotating atmosphere, which is roughly the same as the rotational rate of the earth. The latter is insignificantly small in comparison with the speed of the tether and is not further considered in this analysis.

For a cube with air velocity perpendicular to one of the faces of the cube $C_d = 1.05$, and when the air velocity is at 45 degrees angle with the face, $C_d = 0.8$. When the satellite pair is at its Nadir equilibrium, the air velocity is perpendicular with the cube face. When the in-plane angle of tether rotation is non-zero, the satellites are also rotated with an angle to the air velocity and the drag coefficient will drop to 0.8 at 45 degrees. The area of interest for the aerodynamic drag is how it will affect the equilibrium position of the tether and the assumption of relatively small tether angles is made.

By combining the drag coefficient of a cube with Equations (15) and (16) the atmospheric moment on the system can be written as

$$\boldsymbol{T} = \frac{1}{2} C_d A L \rho v (\boldsymbol{e_p} \times \boldsymbol{v}) \tag{17}$$

When considering the in-plane angle specifically, the magnitude of the moment is

$$T = \frac{L}{4} C_d d^2 \rho_0 v^2 cos\theta \left(1 - e^{\frac{-(h+h_0)}{H}}\right) \tag{18}$$

where L is the length of the tether $[m]$

and d is the side length of the cube. $[m]$

This aerodynamic moment will constantly push the cube away from the equilibrium position and this will in fact shift the equilibrium position to some offset in the in-plane angle. If the moment is combined with the liberation equation for the in-plane angle (Equation (12)), the equilibrium position can be found by setting $\ddot{\theta} = \dot{\theta} = \ddot{\phi} = \dot{\phi} = \phi = \dot{L} = 0$

$$\mu_e L^2 \left(\frac{3\mu_g}{r^3} cos\theta sin\theta\right) = \frac{L}{4} C_d d^2 \rho_0 v^2 cos\theta \left(1 - e^{\frac{-(h+h_0)}{H}}\right)$$

$$\theta_{equilibrium} = sin^{-1}\left(\frac{r^3 C_d d^2 \rho_0 v^2 \left(1 - e^{\frac{-(h+h_0)}{H}}\right)}{12\mu_e \mu_g L}\right) \tag{19}$$

However, analysis of this offset for a bare wire tether of 500m shows that this offset angle will be insignificantly small. Analysis as shown in [7] reveals that for relatively thick tape tethers in the range of 5km, the aerodynamic drag of the tether plays such a significant role that this angle increases to multiple degrees. These studies also reveal that for the same tether structure, but shorter lengths of only hundreds of metres, the effect of aerodynamics on the tether in-plane angle becomes insignificant, supporting the findings made here. The effect of aerodynamics on the system dynamics will thus be ignored for the rest of the analysis.

3.3.6.2 Electromagnetic Force

Classically, the current and bias profiles of EDTs are calculated using numerical methods. This requires a large number of calculations to be done and repeated access to ionospheric models. Bombardelli et al [10] formulated an analytical solution to this problem that has a claimed accuracy of within 7% of numerical methods if specifications of designed subsystems are kept within specified ranges. These analytical solutions will be used to describe the currents and forces for purposes of this study.

The electrodynamic force experienced by the bare EDT is determined by a complex system of interacting physical subsystems. The main governing element is the contact or conductivity from the tether to the plasma surrounding it. The reason is that bad contact restricts the collection and disposal of electrons from the tether system to the surrounding atmosphere which limits the flow of current through the tether and therefore also the electromagnetic force experienced thereby. Traditionally, with large satellites, good contact is ensured by placing a hollow cathodic plasma contactor at each end of the tether. These devices are electrically driven and use electrical energy, to ionise gas and produce plasma. This plasma then provides good contact to the surrounding plasmasphere.

The most definitive work done on the electron collection from the plasma in space was by Sanmartin and Martinez-Sanchez [16]. They in particular studied the effectiveness of a tether system operating under ***Orbit Motion Limited*** (OML) theory conditions. They found that a tether would operate under OML if the tether radius is less than one Debye length. A Debye length is a term in Plasma Physics stating the characteristic shielding distance of a plasma. This limit is about 3mm for tethers in LEO around earth [16]. Studies reveal that tape tethers provide the most effective EDTs [11]. This is mostly due to the fact that it provides maximum robustness against impact of small debris and that it provides a large surface area for electron collection. A tape tether can for instance still operate if only a part of the tape is torn. Even though its efficiency would decrease, it still does not compromise the entire mission.

These tape tethers are typically made from Aluminium. Due to constraints in the local availability of such tethers, the choice was made to design the system with a simpler, cheaper copper wire tether. As this kind of tether is locally available, it enables tests and experiments relevant to the study to be done locally and serves as adequate alternative for tape tethers.

A 0.2mm copper tether was chosen for its small diameter and low weight. Such a tether would not only provide sufficient strength to withstand the forces present in space, but it will also provide good electrodynamic tether performance.

Another paper by Bombardelli et al [11] provides insight to how a CubeSat system would interact with the plasma when operating under OML. The main constraint they place on the performance of the tether system is the contact impedance. The contact impedance is determined by how well the cathodic contactor functions. The performance of these cathodic contactors is power driven and power is one of the main constraints on a CubeSat. Apart from the power issue, the availability and feasibility of miniaturised hollow cathode contactors are unknown and it is very difficult to determine what the performance of a CubeSat sized EDT mission would be. The assumption is made that satisfactory contact with the local plasma is made, but that the performance of the system is limited by the available power of the CubeSat. The detailed design of such a contactor is not within the scope of this study and will not be further discussed. Good plasma contact will be assumed and current profiles will be calculated accordingly. In reality this current flowing in the system may be smaller or limited by these factors. The variability in the magnitude of the current is, however, taken into account when controllers for the system are developed. Even though the current size may vary, the direction of resulting moments on the system is dependent on the orientation of the

tether and the magnetic field. These are known variables in the system and can therefore be used to calculate the directional effect of the tether current, irrespective of its magnitude.

To continue with the design and simulation of the tether system, the local electron plasma density (Ne) of the earth needs to be considered. This plasma density depends largely on solar activity and cannot be accurately modelled mathematically. Values for Ne can be extracted from a large numerical database constructed using past measurements of the electron densities. This, however, requires continuous access to such a terrestrial ionospheric model and is also computationally intensive. For purposes of this document, calculations are done using extreme values of Ne (between $10^{13}\ m^{-3}$ and $10^{11}\ m^{-3}$) corresponding to maximum and minimum solar activity.

The anodic segment length is defined as X_B and the tether length as X_L.

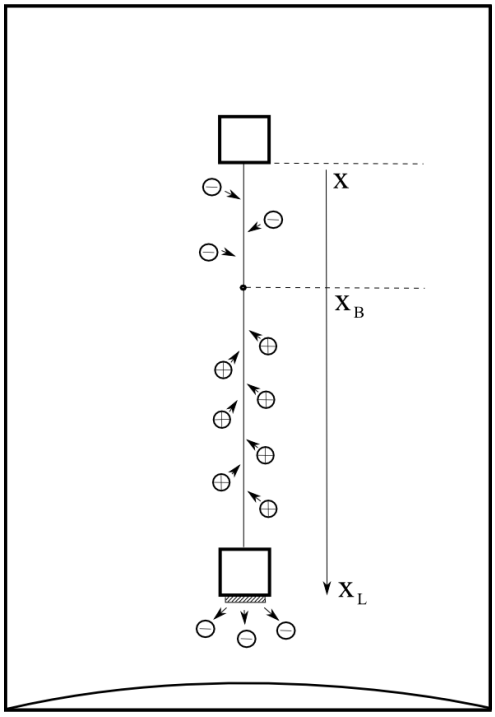

Figure 3.11: Definition of tether segments.

The dimensionless abscissa is defined as

$$\xi = \frac{X}{X_L} \tag{20}$$

and therefore the non-dimensional anodic segment length is ξ_B.

The ideal case is considered where the load impedance is set to zero and the potential drop over the cathode is zero, $\xi_B = 1$ and we reach our characteristic current I_{ch} of [10]

$$I_{ch} = \frac{2p}{3\pi} N_e \sqrt{\frac{2E_t}{m_e} q_e^3 L^3} \tag{21}$$

where

p is the tether cross sectional perimeter	$[m]$
E_t is the projected motional electric field along the tether	$[V \cdot m^{-1}]$
m_e is the electron mass	$[kg]$
q_e is the electron charge	$[C]$
and L is the length of the tether.	$[m]$

For a satellite in a circular orbit through the earth's magnetic field the magnetic field direction in the orbital reference frame is written as in Equation (22). In this case the geomagnetic model described in Section 3.1.2 and the orbital parameters described in Section 3.1.1 is used.

$$\boldsymbol{B} = \frac{B_s r_{eart\,h}^3}{r^3} \begin{bmatrix} -2\sin(u)\sin(i) \\ \cos(u)\sin(i) \\ \cos(i) \end{bmatrix} \tag{22}$$

The motional electric field caused by the satellite moving through the geomagnetic field can be calculated next. The motion of the satellite through the magnetic field is the sum of the orbital motion of the satellite, and the motion of the tether within the orbit. Considering the fact that a gravity gradient Nadir stabilised system is investigated, the magnitude of the motion of the tether is deemed insignificant in comparison with the magnitude of the orbital motion. Assuming a constant magnetic field for the length of the tether the motional electric field component along the tether is written as

$$\begin{aligned} E_t = \boldsymbol{e_{tether}} \cdot (\boldsymbol{v} \times \boldsymbol{B}) &= \begin{bmatrix} 1 \\ 0 \\ 0 \end{bmatrix} \cdot \left(\frac{B_s r_{eart\,h}^3}{r^3} \begin{bmatrix} 0 \\ \sqrt{\frac{\mu_g}{r}} \\ 0 \end{bmatrix} \times \begin{bmatrix} -2\sin(u)\sin(i) \\ \cos(u)\sin(i) \\ \cos(i) \end{bmatrix} \right) \\ &= \frac{B_s r_{eart\,h}^3}{r^3} \sqrt{\frac{\mu_g}{r}} \cos(i) \end{aligned} \tag{23}$$

where

r is the orbital radius	$[m]$
μ_g is earth's gravitational constant	$[m^3 \cdot s^{-2}]$
$r_{eart\,h}$ is earth's radius	$[m]$
B_s is earth's surface magnetic field at the equator.	$[T]$

From Equation (23) it is clear that the motional electric field will vary with the inclination of the orbit and with the orbital radius. The approximate maximum motional electric field in the direction of the tether at 350km altitude and an orbital inclination is calculated as

$$E_t = 0.3304\, V/m \tag{24}$$

Using this potential, an average electron plasma density of $N_e = 0.2 \times 10^{-12}$ and a tether length of 500m, the characteristic current for the 0.2mm copper tether can be calculated as

$$I_{ch} = 32.6\ \text{mA} \tag{25}$$

This was done with the assumption of a conductivity of $\sigma = 6 \times 10^7\ [S \cdot m^{-1}]$ for copper at 20ºC [21]. The conductivity decreases with temperature and the conductivity drops about 30% with an increase in temperature to 100ºC. For this calculation, the accuracy is not that important considering the approximate nature of many of the electrodynamic variables. These calculations are merely an indication of the range of currents to expect and this variability is taken into account when designing the controller which uses the electrodynamic force.

For the control of the current through the EDT, two modes of operation are considered. To be able to control the liberation angles using the EDT, the currents must be calculated which correspond with an 'on'- and 'off'-state for the tether.

For the 'on'-state, the assumption of sufficient contact between the tether and the surrounding plasma is made. As suggested by Claudio Bombardelli [22] (an expert in this field) during personal communications, the best way to approximate a relatively short EDT is to assume that the ohmic effects of the tether is insignificantly small in comparison with the contactor impedence and to calculate the anodic length as a function of the cathodic potential drop. This would require some form of plasma contactor which will have a potential drop associated with it. The suggested potential drop for a CubeSat is 20-40V. For purposes of control, the potential drop can, however, be overcome by biasing the tether with a power source on the satellite. The anodic segment length can thus be controlled to a degree. This is power intensive and lowers the power generation capabilities of the tether, but when used for control, will be activated for only short periods and serves as a viable control method. In this mode the anodic segment length can be written as [10]

$$\xi_{B\ max} = 1 - v_{HC} \tag{26}$$

where v_{HC} is the non-dimensional cathodic potential drop which is calculated using [10]

$$v_{HC} = \frac{\Delta V_{HC}}{E_t L} \tag{27}$$

where ΔV_{HC} is the cathodic contactor potential drop.

The next mode is where a large load is inserted between the tether and the plasma contactor and contact with the surrounding plasma is broken. This mode of operation of an EDT is called a floating EDT [23] and form the lower bound for ξ_B. In this case ξ_B can be approximated as

$$\xi_{B\ min} = \mu^{2/3} \tag{28}$$

where

μ is the ion mass ratio defined as [10]

$$\mu = \sqrt{\frac{m_e}{m_i}} \tag{29}$$

where

m_i is the dominant ion mass at the altitude the tether is operating. At 350km altitude the dominant ion element is oxygen which has an approximate mass of 5.36×10^{-26}kg. The maximum and minimum anodic segment length corresponding to the 'on' and 'off' state is then $\xi_{B\ min} = 0.0325$ and $\xi_{B\ max} = 0.76$ respectively. The average non-dimensional current through the wire can then be calculated as

$$\mathrm{i}_{av} = \frac{\xi_B^{3/2}(5 - 2\xi_B) - 2\mu(1 - \xi_B)^{5/2}}{5} \tag{30}$$

where

$$\mathrm{i}_{av} = \frac{I_{av}}{I_{ch}} \tag{31}$$

Using the characteristic current calculated in Equation (25) and the average non-dimensional current calculated in Equation (31) the maximum and minimum average electric current that will flow in the tether is calculated as $I_{av\,min} = 0.12$ mA and $I_{av\,max} = 15$ mA. The electric current profile over the length of the tether is shown below.

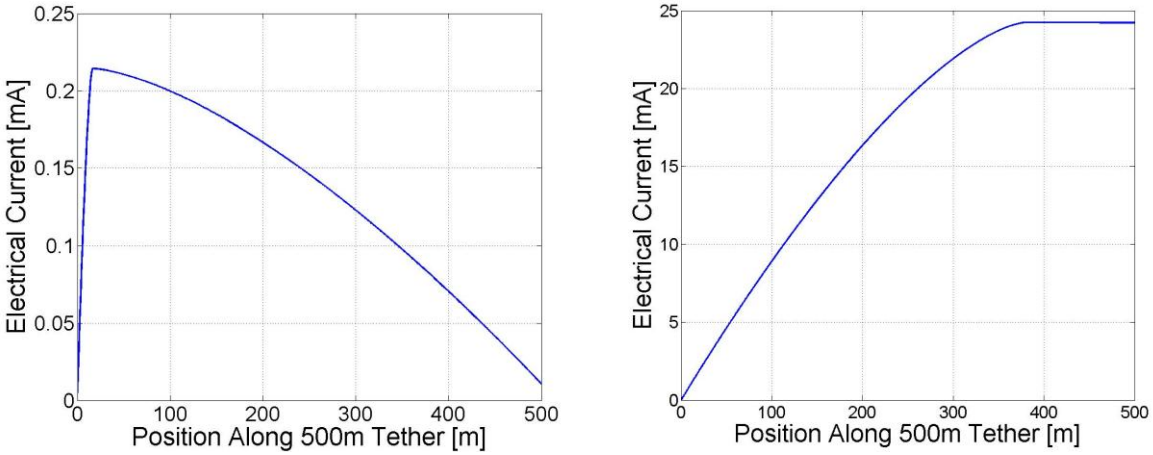

Figure 3.12: Electrical current profile for floating EDT (left) and for EDT with plasma contactor (right).

The displacement of this average current from the centre of mass is required to calculate the moment on the system. To do this, the following equation is used

$$\xi_d = \frac{1}{14}\frac{8\xi_B^{7/2} - 35\xi_B^{3/2} + 4\mu(1-\xi_B)^{5/2}(5+2\xi_B)}{2\xi_B^{5/2} - 5\xi_B^{3/2} + 2\mu(1-\xi_B)^{5/2}} \tag{32}$$

When the average current is known, Equation (21), (23) and (24) can be combined and the tether Lorentz force can be calculated using the following equation

$$\mathbf{F} = \mathrm{i}_{av} I_{ch} BL(\hat{\boldsymbol{e}}_{\boldsymbol{t}} \times \hat{\boldsymbol{e}}_{\boldsymbol{B}}) \tag{33}$$

where

the local magnetic field is $B\hat{\boldsymbol{e}}_{\boldsymbol{B}}$ $[T]$

and the vector along the tether is $L\hat{\boldsymbol{e}}_{\boldsymbol{t}}$. $[m]$

The Lorentz torque is calculated as

$$\mathbf{T} = F(\xi_d - \xi_{COM})\,(\hat{\boldsymbol{e}}_{\boldsymbol{t}} \times \hat{\boldsymbol{e}}_{\boldsymbol{F}}) = \mathrm{i}_{av} I_{ch} BL^2(\xi_d - \xi_{COM})[\hat{\boldsymbol{e}}_{\boldsymbol{t}} \times (\hat{\boldsymbol{e}}_{\boldsymbol{t}} \times \hat{\boldsymbol{e}}_{\boldsymbol{B}})] \tag{34}$$

Using Equation (34), the Lorentz torques during 'on' and 'off' states for the tether, can be calculated. The maximum torque that can be expected, if the assumption of orthogonal magnetic field and tether orientation is made, is $|T_{on}| = 12.2\text{mN}$ and $|T_{off}| = 9.6 \times 10^{-5}\text{mN}$. Actual torques, within an orbit with an inclination and varying magnetic field direction, will be smaller. Within the simulations done in Section 5.1, the full IGRF model is used to accurately calculate the electromagnetic torques acting on the system.

3.3.6.3 Tether Elasticity

Like any other metal, the tether will deform when tension is applied to it. While the tether is in the process of being deployed, the tension in the tether is so low that the deformation of the tether is insignificant. If the tether, however, becomes taut while the satellites are still drifting apart, the kinetic energy of the satellites will be momentarily transferred to elastic potential energy in the tether, and then converted back to kinetic energy with the satellites moving back towards each other. The satellites will however be kept apart by gravity gradient forces. If the satellites are moving too fast, the energy in their motion may be enough to stretch the tether to the point where it deforms permanently or breaks. If however, the deformation of the tether is within its elastic range, the process will be a sequence of energy transfers, and minimal energy will be consumed by friction within the tether.

In this section the elastic force the tether will exert on the system, and the limit at which the tether will deform permanently, are investigated. This will lead to a better understanding of what would happen in the situation where the controller loses control over the deployment process and the tether is fully unwound.

The elasticity of the copper tether is described by Young's modulus. This relates the tension in a material to the amount it is deformed. Young's modulus for Copper is in the order of 117GPa. Using this value, the tension in the tether when stretched can be written as

$$\mathrm{F} = \frac{E A_0 \, \Delta L}{L_0} \tag{35}$$

where

E is Young's modulus of the material	$[N \cdot m^{-2}]$
A_0 is the cross-sectional area of the un-stretched material	$[m^2]$
L_0 is the length of the un-stretched material	$[m]$
and ΔL is the length the material is stretched.	$[m]$

The tensile tension (Γ) within the copper tether is then calculated as

$$\Gamma = \frac{F}{A_0} = \frac{E \Delta L}{L_0} \tag{36}$$

If the system reaches the point where the tether becomes taut, the important thing to consider is if the satellite are moving fast enough, and therefore have enough kinetic energy to stretch the tether beyond its elastic range. If so, the tether will deform permanently or break. Breaking the tether would have mission critical consequences. Stretching the tether beyond its elastic range and causing permanent deformation within the structure of the copper, may however, also be critical to the operation of the EDT. When a material deforms beyond its elastic range, the conductivity of the material is drastically decreased. The limit of the elastic range of a material is called the yield point. The yield strength is the tension at which this yield point is reached, and for copper this is 70MPa. Considering that the deformation of the tether is mission critical, a 50% safety factor is used and the tension limit for the tether is set

to 35MPa. The maximum elastic deformation which is then possible for the tether is calculated as

$$\Delta L_{max} = \frac{\Gamma_{max} L_0}{E} \tag{37}$$

The energy required to stretch the tether to the point of deformation can be calculated by integrating the tether elastic force over the distance the tether is stretched.

$$F = \frac{E A_0}{L_0} \Delta L$$

$$\int_0^{L_{max}} F \, d(\Delta L) = \frac{E A_0}{L_0} \int_0^{L_{max}} \Delta L \, d(\Delta L)$$

$$V = \frac{E A_0}{2 L_0} (\Delta L_{max})^2$$

$$V = \frac{L_0 A_0}{2E} \Gamma_{max}^2 \tag{38}$$

To ensure that this point is not reached, the predetermined masses of the satellites are used to calculate the kinetic energy of the system for a given deployment speed as done in Section 3.3.5

$$T = \frac{1}{2} \mu_e \dot{L}^2 \tag{39}$$

If this kinetic energy in the motion of the satellites exceeds the energy required to stretch the tether to its upper elastic bound, the tether will be in danger of being deformed permanently. This then forms the upper limit for the deployment kinetic energy of the system to be within a safe range. The maximum safe deployment speed can be calculated by combining Equations (42) and (43)

$$\dot{L}_{max} = \sqrt{\frac{A_0 L_0 \Gamma_{max}^2}{\mu_e E}} \tag{40}$$

Using this equation, the maximum deployment speed of the satellites at the point where the tether becomes taut is calculated as 2.3m/s.

3.3.7 Satellite Body Rotation

One aspect of the dynamics of the system that may have a significant influence on the system, but which has not been included in the derivation of the dynamic equations, is the satellites' individual body rotations and the effect the tether has thereon. The satellite body oscillations were a particular problem in the Gemini 11 mission where the rotations could not be damped, and the mission was eventually terminated [2].

The moment that the tether exerts on the satellites depends greatly on the connection point of the tether to the satellites and the distance this point is from the COM of the satellite. With a CubeSat, the body of the satellite is extremely small, and even if the tether is attached to the side of the satellite, this distance is still very small. The moments are therefore also small in comparison with the moments and forces present on the tether system as a whole. The CubeSats, however, have a very low moment of inertia, which means that even though the moments are small, they still have a significant effect on the satellite orientation.

To accurately model these torques and rotations, the rotations of the satellite bodies and their inertia have to be modelled and included when doing the Lagrangian calculations for the modelling of the system. The kinetic energy in the rotation of the satellites, as well as the effect a rotation of the satellite has on the gravitational potential of the system, have to be calculated. To do so, two new variables are needed for each satellite, describing its rotation with two angles relative to the tether body frame. The system then goes from being a three variable system to a seven variable system, which dramatically complicates the mathematics involved in the derivation process.

If the assumption is made that the effect of the body rotations on the tether is insignificant, the dynamics of the tether and the satellite body can be separated. The tether is then still modelled as having two point-like end masses. The effect the tether has on the rotation of the satellite on the other hand, is of importance, considering that the ADCS of the satellite needs to be capable of maintaining the satellite's orientation even though the tether is disturbing it. With the model of the tether dynamics known, the satellite can use its sensor data of the tether angles and distance to estimate the disturbance force from the tether and an efficient ADCS control system can be implemented.

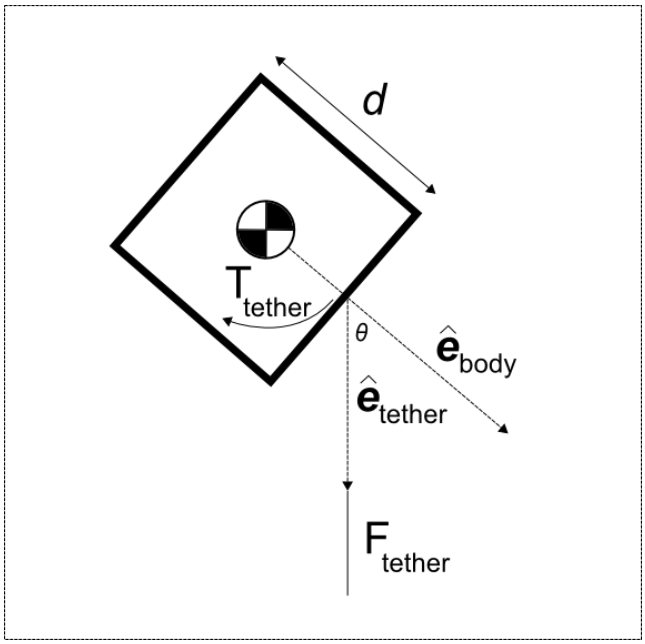

Figure 3.13: Tether tension as disturbance force on satellite body.

Using the vectors defined in Figure 3.13 the disturbance moment of the tether on the satellite can be written as

$$\mathbf{T_{tether}} = \frac{1}{2} d\mathrm{F}_{tether} (\hat{\boldsymbol{e}}_{\boldsymbol{body}} \times \hat{\boldsymbol{e}}_{\boldsymbol{tether}}) \tag{41}$$

The main satellite will have a 3 axis reaction wheel system for doing ADCS and because a constant Nadir-orientation is required, the tether needs to be attached as close to the COM as possible.

3.4 Attitude Determination and Control

The ADCS strategy of the system is complicated by the fact that the system consists of multiple separate bodies. The orientation of the two satellites as well as the tether need to be monitored and controlled.

The ADCS of the system is separated into two modes, the first being before the deployment of the tether when the two satellites are still connected as a 3U unit, and the second mode when the tether is deployed. While the satellites are still connected, the main satellite will be responsible for all ADCS tasks, including detumbling and orientating the system to the Nadir direction. After the deployment is done, the main satellite will stay Nadir pointing, using its ADCS equipment to orientate itself towards Nadir with relatively high pointing accuracy. The main satellite will also be responsible for the control of the tether angle and for the tether deployment. This requires sensors and actuators for measuring and controlling the relative angle between the two satellites and the Nadir vector, and the deployed distance of the tether.

The rest of this section discusses the implementation of such sensors and actuators and the control algorithms needed to control the system.

3.4.1 Sensor Design

3.4.1.1 Relative Angle

The orientation control of the tether system is described by the control of the in- and out-of-plane angles θ and ϕ. These angles describe the orientation of the vector between the two satellites in relation to the Nadir direction. To measure these angles, the absolute positions of both satellites must be determined and the angle then calculated from these positions, or the rotation of one of the satellites must be kept fixed and the angle of the other must be measured relative to a fixed face on the first satellite. Determining the absolute position of a satellite is a complex task. Sensors such as a ***Global Positioning System*** (GPS) can be used in larger satellites, but are too energy intensive for CubeSat applications and lack the necessary accuracy to sufficiently determine the relative angles between the satellites at a distance of 500m.

A CMOS imager based sensor is proposed for this design. The strategy is to keep the lower satellite of the pair in a constant body rotation so that one face of the satellite points in the Nadir direction. A camera will then be mounted on the opposite face of the satellite, facing away from earth. The satellite in the higher altitude has a bright directional LED on its side facing towards earth. The LED will be visible as a dot on the imager on the lower satellite. If the lower satellite's orientation is known, the boresight of the camera, which has fixed orientation relative to the satellite body, is also known. The angle between the camera boresight orientation vector and the vector towards the top satellite can then be determined by the position of the LED dot in the image.

The lens used for the camera would have to be a narrow beam lens for two reasons. Firstly, the wider the **Angle of View (AOV)** of the lens, the lower the angular resolution of the sensor becomes. Secondly, the lens needs a narrow field of view to keep the sun out of the AOV of the camera for the largest fraction of the orbit. If the sun is in the AOV the light from the sun will overexpose the image and the LED will not be visible.

The AOV view of the lens is determined by its focal length *f*. The focal length determines the size of the LED on the image sensor as well as the AOV of the lens. The AOV α, is given by Equation (42).

$$\alpha = 2arctan\left(\frac{d}{2f}\right) \tag{42}$$

where

d is the width of the image sensor. []

If the assumption of infinity focus is made, the size of an object on the image sensor is determined by the following relation:

$$x = \frac{fX}{D} \tag{43}$$

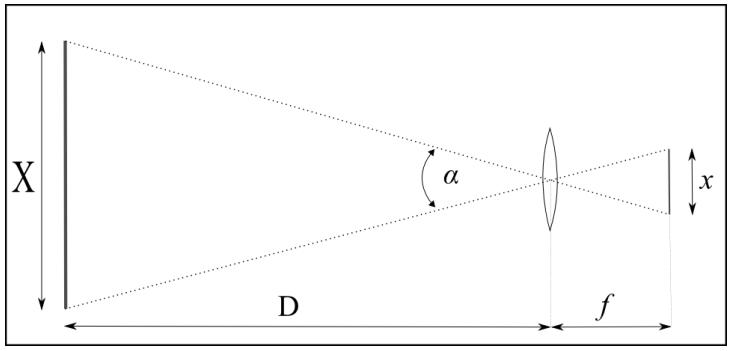

Figure 3.14: Lens focal length.

The choice of focal length for the lens is based on the fact that the LED must be in the field of view of the camera even when the satellites are at a maximum relative angle.

Using Equation (43), the actual size that a pixel of the image sensor represents on an image plane at distance D away from the camera, can be calculated. If a sensor is used with physical pixel size of p, the projected size P the pixel represents at distance D is

$$P = \frac{Dp}{f} \tag{44}$$

With a LED size of l, the LED will only represent one pixel on the image sensor when the distance between the LED and the camera is greater than

$$D = \frac{lf}{p} \tag{45}$$

In the case where the LED only illuminates one pixel at a time, the sensor reading of the position of the LED will be quantised in nature because of the limited resolution of the camera. The amount of pixels on the ***Complementary Metal-Oxide-Semiconductor*** (CMOS) sensor is easily calculated by dividing the total width of the sensor by the width of a pixel. With the amount of pixels and the AOV known, the angle each pixel represents is calculated by

$$\Delta\alpha = \alpha\frac{p}{d} \tag{46}$$

To ensure that the LED is visible at a specific distance, the luminous flux of the light on the lens must meet two requirements namely, being larger than the brightest star in the view of the camera and being large enough to overcome the sensor's minimum sensitivity.

A lens with radius *b* placed at a distance of D from a light source, measures $\frac{\pi b^2}{D^2}$ steradians. If a LED is used with intensity of I_v Candela, the luminous flux that reaches the lens can be calculated as:

$$\emptyset_v = \frac{I_v \pi b^2}{D^2} \tag{47}$$

and the illuminance of a single pixel with width *p* is then

$$E_v = \frac{I_v \pi b^2}{D^2 p^2} \tag{48}$$

The largest star in the sky is Betelgeuse which has an angular diameter of approximately 50×10^{-3} arc seconds viewed from earth. For such a star to be larger than a pixel on the sensor, the focal length of the lens needs to be impractically large. We thus assume a star will always just illuminate one pixel at a time. Betelgeuse has a luminance intensity of 3.3×10^{32} Candela. With the star at a distance of 642.5 light years, a lens size of *b* and pixel size of *p*, the illuminance of the star on the image sensor if orbiting in LEO can be calculated using Equation (48). It is important to note that the effects of temperature changes on the sensitivity of the camera are compensated for by the Auto-White-Balance capabilities of the sensor.

As mentioned in Section 3.2.1 the orientation of the payload satellite is not required to be fixed. There are of course constraints to the motion of the satellite in the sense that it should not complete full rotations, for this will cause the tether to wind up or break. The only requirement is that the payload satellite must be measurable from the main satellite. This can be assured, irrespective of the orientation of the payload satellite, if multiple LEDs are placed on the payload satellite in such a way that their beam widths overlap to the extent that it covers a full hemisphere. Using LEDs with beam-width of about 20° this is easily achieved.

A limitation of this design is that the sensor will not be able to provide measurements when the sun is in the AOV of the camera. The deployment must therefore be scheduled in such a period where the sun will not interfere with measurements. For periods where the sun does restrict measurement updates, the EKF can still be used to estimate the states using time updates and propagating the states using the model of the system.

3.4.1.2 Distance between satellites

During deployment, the distance between the two satellites and the rate at which this distance increases, must be measured to ensure that the deployment process is smooth and the deployment is done to the desired distance. As with the relative angle sensor, the key constraints for the sensor design are power, size and weight.

There are two ways of measuring the deployment distance. The first is having a sensor capable of measuring the absolute distance between the satellites. This can be done by having some sensor on the one satellite, capable of sensing the other, and from the sensor data calculating the distance. This would require a sensor capable of range-finding over hundreds of metres. Possible options for such sensors include laser rangefinders, radar, and GPS sensors. All of these sensors are relatively bulky and high power. These sensors therefore do not fit the requirements for CubeSat applications.

An alternative method of measuring the distance is by an incremental measurement system where the distance is updated as it increases from a relative position. In such a system, not the distance between the satellites, but rather the distance to which the tether is deployed, is measured. This method is not as reliable as the first for multiple reasons. Firstly, it relies on the assumption that the tether is straight and under tension. Whenever the tether becomes slack, the two satellites will in fact be closer than the predicted measurement. Secondly, because of the fact that the distance is updated from a previous measurement, there is a risk of losing the current distance due to electronic failure, which will then lead to the system being in an unknown position.

The first problem is something that cannot be solved, because it is inherent to the type of measurement this method uses. The assumption of a straight tether is something that is a theme throughout the entire system analysis, though, and is something that is focussed on during the whole analysis and design process. By slow and controlled deployment this problem can be essentially eliminated.

The second problem is something that can be solved, using signal processing and hardware architecture techniques. The main risk is that the processor could reset, resulting in all system variables being lost. To solve this problem, the deployment distance can be iteratively written to non-volatile memory and new measurements can be continuously correlated with this data to ensure no information is lost. In the case of a MCU reset, the last written distance in the memory can be loaded and the process can be continued from that position.

Implementing such a sensor can be done by using any type of rotary encoder. The encoder can be placed on the reel containing the tether and can so count the number of rotations of the reel. This will give a discretised reading of the deployment distance where the discrete measurement levels depend on the rotary resolution of the encoder.

The deployment distance is then

$$s = \frac{2\pi R_{reel}}{\eta_{sensor}} S_{sensor} \tag{49}$$

where

R_{reel} is the radius of the reel containing the tether []

η_{sensor} is the dimensionless resolution of the sensor in *counts per revolution* and S_{sensor} is the sensor output count. []

In the case of a 500m tether unwinding from the reel, the reel's radius will not be constant since the further the tether unwinds, the smaller the diameter of the reel becomes.

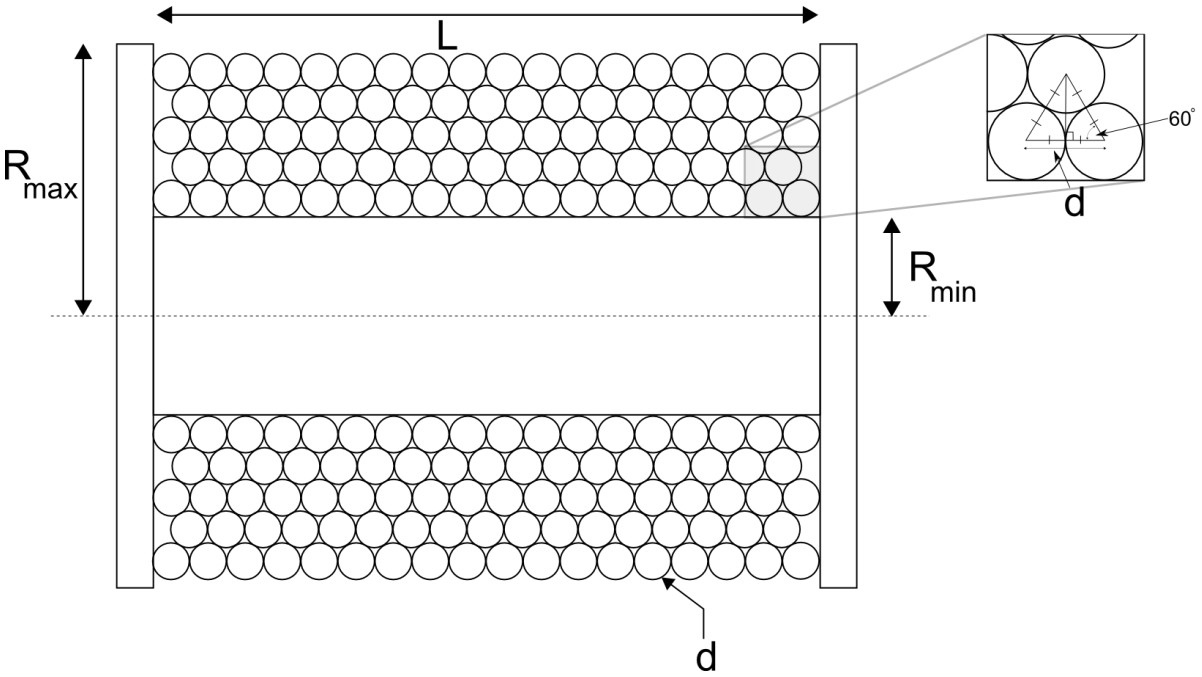

Figure 3.15: Deployment spool with cylindrical wire.

If there is a total of N windings on the reel when it is full, and the reel and wire have dimensions shown in Figure 3.15, the number of turns per layer and the reel thickness (R_{max}) can be calculated as

$$\text{Turns per layer} \approx \frac{L}{d} \tag{50}$$

$$\text{Number of layers} = \frac{Nd}{L} \tag{51}$$

$$R_{max} = R_{min} + \frac{Nd^2}{L}\sin(60°) = R_{min} + 0.87\frac{Nd^2}{L} \tag{52}$$

The thickness of the reel will hence drop with 0.87 times the wire diameter *d* after every layer is removed. The thickness will drop from R_{max} at the start of deployment to R_{min} at the end. The reel thickness can be approximated linearly for calculations to determine the distance of tether deployed.

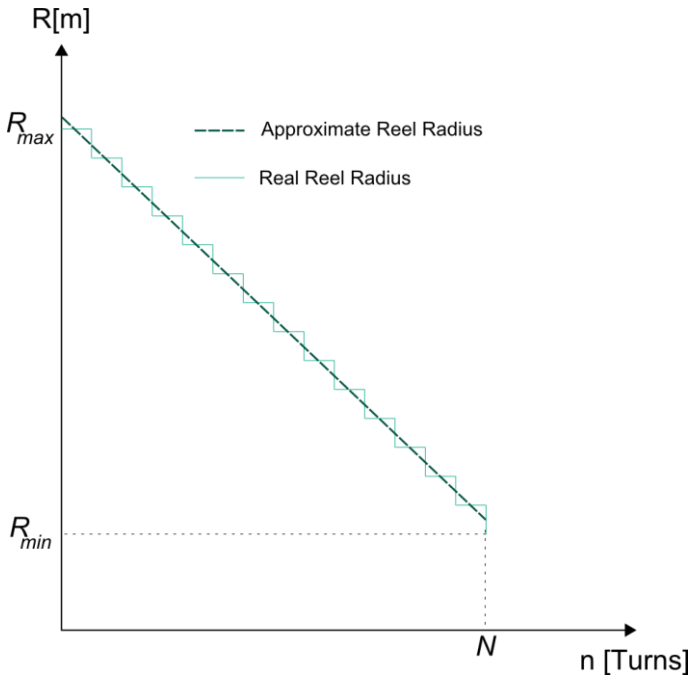

Figure 3.16: Change in spool radius with amount of tether deployed.

The reel radius *R* as a function of the amount of rotations *n* is given by

$$R_{reel} = \left(\frac{R_{min} - R_{max}}{N}\right) n + R_{max} \tag{53}$$

3.4.2 Actuator Design

3.4.2.1 Deployment Distance

The distance between the two satellites and therefore the length of the tether connecting the two satellites will be controlled by controlling the feed rate of the reel located on the main satellite. This can either be done passively by placing mechanical damping on the reel, or actively by controlling the speed of the reel using an electric motor. Both of these methods have advantages. The passive system is simpler to implement, will take less space in the satellite, will weigh less and will consume less power. There are, however, a number of variables such as temperature, friction and expansion of materials that may influence deployment performance and cannot be controlled. The active solution offers better control of deployment speed, more certainty that the reel will not get stuck, and the option of also reeling the tether back in at the end of life, if required. Reeling the tether in opens the option of not only testing the behaviour of the system as the tether is deployed, but also as it is retracted. Not a lot of experimental data is available regarding this, and the knowledge gained while doing so will add extra value to launching the tethered system.

The force the motor will exert on the tether is simply a function of the torque of the motor, the friction torque in the motor and reel combination, and the diameter of the reel.

$$F_{motor} = (T_{motor} - T_{friction})/R_{reel} \quad (54)$$

Where R_{reel} is the radius of the reel as discussed in Equation (53).

3.4.3 Control Algorithms

3.4.3.1 Relative Attitude Control

The stability of tether systems has been discussed in many papers [4] [8] [9]. All of these assume certain parameters for the physical structure of the tether, the electrodynamic interaction of the tether with the plasmasphere, and the environment the tether will be operating in. These are all very complex mathematical models and are very difficult to experimentally verify. The lack of completed past tether missions means that there are very little experimental data to use to gain certainty about how the tether will react in space. The modelling of the electromagnetic force depends largely on how well the tether makes contact with the local plasmasphere. Good contact is usually ensured by using a hollow cathode contactor, but in the case of CubeSats, power and size constraints mean that there are no miniaturised cathodic contactors available.

With this shortage of accurate and reliable models in mind, the choice was made to simplify the control algorithms for the ADCS of the tether system to a bang-bang controller focussing more on the stability of the tether at large angles than on the accuracy of control at small angles. The magnitude of the electrodynamic force expected from the tether is small in comparison with the gravity gradient forces. Further, considering the relatively large inertia of the tether system, the influence these electrodynamic moments will have on the system is small. Control will therefore be done over a very large time scale and at very low rates.

After a specific tether with a specific contactor impedance is determined as discussed in Section 3.3.6.2 the only variable influencing the current flowing through the tether is the load impedance. This is the control input which can be used to control the current flowing through the tether. The tether operates in different electromagnetic modes depending on the load impedance and the current flowing through the tether. The analytical solutions derived for these currents are thus only accurate for certain cases where the load impedance falls within a certain range. Having the load impedance changing to different values ranging from an open circuit to a short circuit thus creates more uncertainty in how the system will react and complicates the modelling problem even further. As suggested, the solution is to use a bang-bang controller where instead of a variable load; a load with fixed magnitude is used. The load is switched on or off depending on whether a tether current is desired. This not only simplifies the modelling problem, but also the practical implementation of such a tether control system.

Information about the current magnetic field measurements done by the satellite, and the current orientation of the satellite measured by its ADCS sensors are used to determine if an electromagnetic current through the tether at that time will result in a force decreasing the

magnitude of the oscillation in the θ and ϕ angles. Direction of the rotation of the satellite is compared with the electrodynamic moment that will result from a current flowing through the wire, and if the direction of the moment and the direction of the rotation are in opposite directions, current is allowed to flow through the tether. This is illustrated in Figure 3.17.

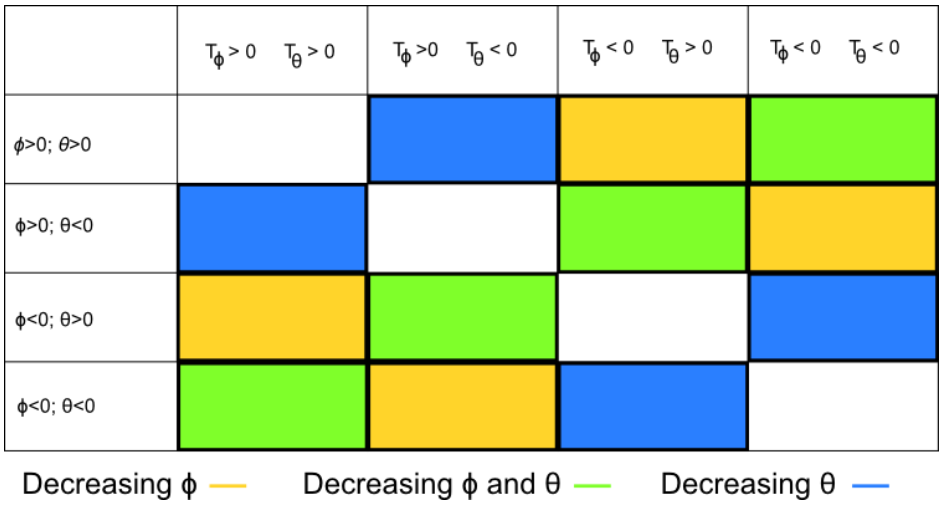

Figure 3.17: Electromagnetic control strategy.

The problem, however, is that while allowing the current to flow through the tether at a specific stage might benefit the rotation of the system in the one angle, it might worsen the rotation in the other. There are two solutions to this problem. The first is to only allow a tether current when the tether is in such a position in orbit and at such an orientation that it will benefit both angles simultaneously. The second is to devise some weighting system which determines the priority of controlling a specific angle and then making the control decision based on this.

The weighting system considers the RMS value of the oscillation in the angle. An acceptable oscillation is set before the control starts and acts as baseline for the weighting system. In the case of the EDT in orbit, the θ angle typically gains larger oscillations during deployment due to the fact that the system has a large orbital rotation in the same axis. If there were no tether in the system, this is the angle in which the lower body would gain relative position over the upper body because of its higher orbital rotational velocity. During deployment the orbit radius of the satellites changes and to conserve the system's angular momentum, their orbital rates need to change with it. The bottom satellite therefore moves ahead in the orbit and an oscillation in the θ angle after deployment, is inevitable.

For this reason the weighting of the two angles will be set up to favour the θ angle for control.

In practice the proposed mission can serve as a valuable tool to verify the electromagnetic modelling involved in calculating the Lorentz torques on a tether system. Angle measurements done by the relative sensor and tether currents measured by on-board electronics can be combined and the results can be compared with existing OML theory. This can serve as experimental verification for this theory and will be useful for all future tether missions.

3.4.3.2 Deployer Control

The control of the tether length is influenced by forces such as gravity gradient and centrifugal forces. These are non-linear forces dependent on all the system variables. Two controllers were designed to control the deployment speed of the tether.

The first is a purely proportional controller using only the measured tether distance as sensor input. The distance is differentiated and low-pass filtered to obtain the deployment speed, which is then fed into the proportional controller. The low pass filter is necessary to illuminate spikes in the speed because of the quantised nature of the distance measurements. This type of controller is well suited for the prototype tests on earth, where the only dominant force on the mass is the gravitational force pulling it towards the earth. In the case of the tethered system in space, the centrifugal forces and increasing gravity gradient forces form the dominant forces in the deployment system and purely proportional control does not perform well. This control method was, however, demonstrated to still provide acceptable control of the deployment speed.

The second controller implemented was a non-linear full state feedback controller using an EKF to estimate the states of the non-linear system. The sensors that are available, measures the tether angles and the deployment distance, but not the angular rate at which the tether is rotating or the speed at which the tether is deployed. The EKF provides the means to estimate these states from the limited measurements that are available. The first step in designing the EKF was to set up the state space representation of the system in terms of the state variables.

The state vector is defined as

$$\boldsymbol{x} = [\theta \quad \phi \quad L \quad \dot{\theta} \quad \dot{\phi} \quad \dot{L}] \tag{55}$$

From the equations derived in Section 3.3.5, the time derivative of the state vector can be written as

$$\dot{\boldsymbol{x}} = f(\theta, \phi, L, \dot{\theta}, \dot{\phi}, \dot{L}) + \boldsymbol{W_t}$$

$$= \begin{bmatrix} \dot{\theta} \\ \dot{\phi} \\ \dot{L} \\ -2(\dot{\theta} + \omega_o)\left(\frac{\dot{L}}{L} - \dot{\phi}tan\phi\right) - 3\omega_o^2 cos\theta sin\theta \\ -2\frac{\dot{L}}{L}\dot{\phi} - cos\phi sin\phi((\dot{\theta} + \omega_o)^2 + 3\omega_o^2 cos^2\theta) \\ L\dot{\phi}^2 + Lcos^2\phi(\dot{\theta} + \omega_o)^2 + L\omega_o^2(3cos^2\phi cos^2\theta - 1) \end{bmatrix} + \boldsymbol{W_t} \tag{56}$$

where $\boldsymbol{W_t}$ is zero-mean Gaussian process noise with covariance matrix of $\boldsymbol{Q_t}$.

With a sensor for measuring the in- and out-of-plane angles, and tether length, the measurement equation can be written as

$$\boldsymbol{y} = \boldsymbol{h}(\theta, \phi, L) + \boldsymbol{V_t} = \begin{bmatrix} \theta \\ \phi \\ L \end{bmatrix} + \boldsymbol{V_t} \tag{57}$$

where $\boldsymbol{V_t}$ is zero mean Gaussian measurement noise with covariance matrix of $\boldsymbol{R_t}$.

The Jacobian of the state equation of the system is then

$$\boldsymbol{F} = \frac{\partial \boldsymbol{f}}{\partial \boldsymbol{x}} = \tag{58}$$

$$= \begin{bmatrix} 0 & 0 & 0 & 1 & 0 & 0 \\ 0 & 0 & 0 & 0 & 1 & 0 \\ 0 & 0 & 0 & 0 & 0 & 1 \\ 3\omega_o^2(s^2\theta - c^2\theta) & 2\vartheta\dot{\phi}sec^2\phi & \frac{2\vartheta\dot{L}}{L^2} & 2\left(\dot{\phi}t\phi - \frac{\dot{L}}{L}\right) & 2\vartheta t\phi & \frac{-2\vartheta}{L} \\ 6\omega_o^2 s\theta c\theta s\phi c\phi & [\vartheta^2 + 3\omega_o c\theta](s^2\phi - c^2\phi) & \frac{2\dot{L}\dot{\phi}}{L^2} & -2c\phi s\phi\vartheta & -2\frac{\dot{L}}{L} & -2\frac{\dot{\phi}}{L} \\ -6L\omega_o^2 s\theta c\theta c^2\phi & -2Ls\phi c\phi\vartheta^2 - 6L\omega_o^2 c^2\theta s\phi c\phi & \dot{\phi}^2 + c^2\phi\vartheta^2 + \omega_o^2(3c^2\phi c^2\theta - 1) & 2Lc^2\phi\vartheta & 2L\dot{\phi} & 0 \end{bmatrix}$$

where

$sin\theta$ is written as $s\theta$

$cos\theta$ is written as $c\theta$

$tan\theta$ is written as $t\theta$

and the assignment $\vartheta = \left(\dot{\theta} + \omega_o\right)$ is done to shrink the physical size of the term.

The Jacobian of the measurement equation of the system is

$$\boldsymbol{H} = \frac{\partial \boldsymbol{h}}{\partial \boldsymbol{x}} = \begin{bmatrix} 1 & 0 & 0 & 0 & 0 & 0 \\ 0 & 1 & 0 & 0 & 0 & 0 \\ 0 & 0 & 1 & 0 & 0 & 0 \end{bmatrix} \tag{59}$$

An EKF is then implemented using the following steps [19]:

First are the control-update steps

$$\boldsymbol{P_k^-} = \boldsymbol{A_{k-1}} \boldsymbol{P_{k-1}^+} \boldsymbol{A_{k-1}^T} + \boldsymbol{Q_k} \tag{60}$$

$$\boldsymbol{X_k^-} = \boldsymbol{X_{k-1}^+} + \dot{\boldsymbol{X}}_{\boldsymbol{k-1}}^+ \boldsymbol{T_s} = \boldsymbol{X_{k-1}^+} + \boldsymbol{f}(\dot{\boldsymbol{X}}_{\boldsymbol{k-1}}^+)\boldsymbol{T_s} \tag{61}$$

and then the measurement-update steps:

$$\boldsymbol{L_k = P_k^- C_k^T \left(C_k P_k^- C_k^T + R_k \right)^{-1}} \tag{62}$$

$$\boldsymbol{P_k^+ = (I - L_k C_k) P_k^-} \tag{63}$$

$$\boldsymbol{X_k^+ = X_k^- + L_k \left[y_k - h(X_k^-) \right]} \tag{64}$$

By implementing these steps recursively, an estimate for the state vector is obtained which can then be used to calculate a control signal. As part of the EKF design, the covariance matrices $\boldsymbol{Q_k}$ and $\boldsymbol{R_k}$ have to be specified. The effect of these two matrices is that its relative size determines if new measurements or the model is more reliable and thus serves as a weighting system. These variables influence the performance of the EKF, and for the algorithm to function optimally, these values have to be chosen in relation with the accuracies of the sensors providing the measurements.

4 Hardware & Testing

4.1 Overview

4.1.1 Test Environment

The sensors that are designed in this study are for use on satellites and will therefore be used in a space environment. For testing the tether angle sensor, which is camera based, the main difference between the space environment and the environment on earth is that atmospheric effects in terms of scattering and losses are much smaller in space. The effect of the atmosphere on the light travelling through it is, however, not a significant issue, and the sensors can be reliably tested on earth. For testing the deployment mechanism, the large gravitational pull of the earth forms a significant difference to the space environment. Eliminating this large disturbance force is also very difficult and poses a particular challenge in the process of testing the deployment mechanism. One of the main challenges in deploying a tether in space is the fact that there are no, or only small forces, pulling the satellites apart. The deployment is done mainly by separating the satellites with force and then relying on momentum to ensure sufficient deployment distance until the gravity-gradient force becomes significant. As the satellites drift further apart, the gravity-gradient force becomes larger and then provides the tension needed to ensure further deployment. The challenge is thus to design a deployment system that has low enough friction force constricting the deployment so that the deployment can be reliable.

For the deployment system to be tested in conditions similar to those in space, the large gravitational pull from earth must be removed from the system. To test the deployment mechanism on earth, one of the two satellites needs to be grounded, in contrast with the space environment where both satellites float freely. The other satellite can then be deployed from this fixed point. The deployed satellite will as mentioned, experience a constant gravitational pull in the direction of the earth. To compensate for this gravitational pull, two solutions are suggested.

The first proposed solution involves deploying the tether horizontally and placing the deployed satellite on a flat, horizontal, frictionless table. By doing so, the deployment direction is rotated orthogonally to the gravitational force, and no longer has a significant influence on the deployment process. To emulate the gravity-gradient force that is present in space, the frictionless table can be tilted to a slight angle so that only a small component of the gravitational force is in the direction of the tether. This setup is illustrated in Figure 4.1.

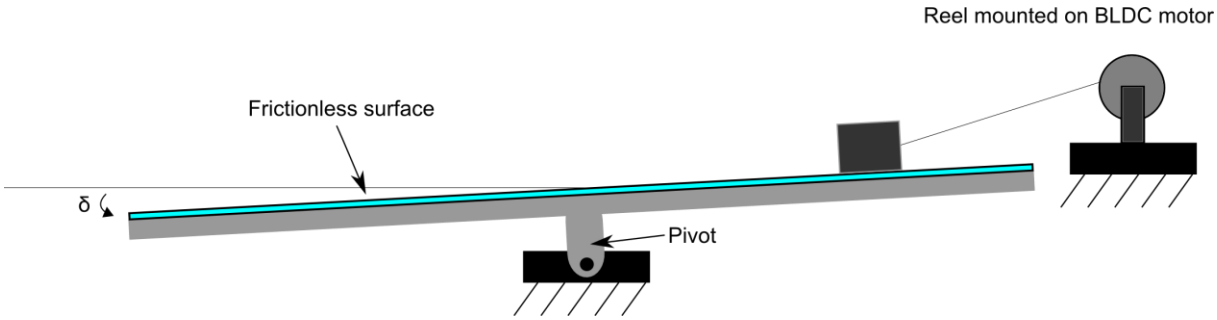

Figure 4.1: Illustration of frictionless table to simulate space gravity.

This solution provides an accurate way of removing the effect of gravity from the deployment process. Unfortunately such a frictionless table is not available for this study and this solution could not be implemented.

A second proposed solution to eliminate the effects of gravity from the deployment is to attach a second tether to the deployed satellite. The force this second tether exerts on the satellite is then controlled to cancel out the gravitational force. In this way the deployment tether only exerts the control forces on the deployed satellite, while this second tether is responsible for continuously compensating for earth's gravity. To be able to control the tension in this second tether a sensor is needed to measure the tether tension. A loadcell was chosen to accomplish this. A diagrammatic representation of the system is shown below.

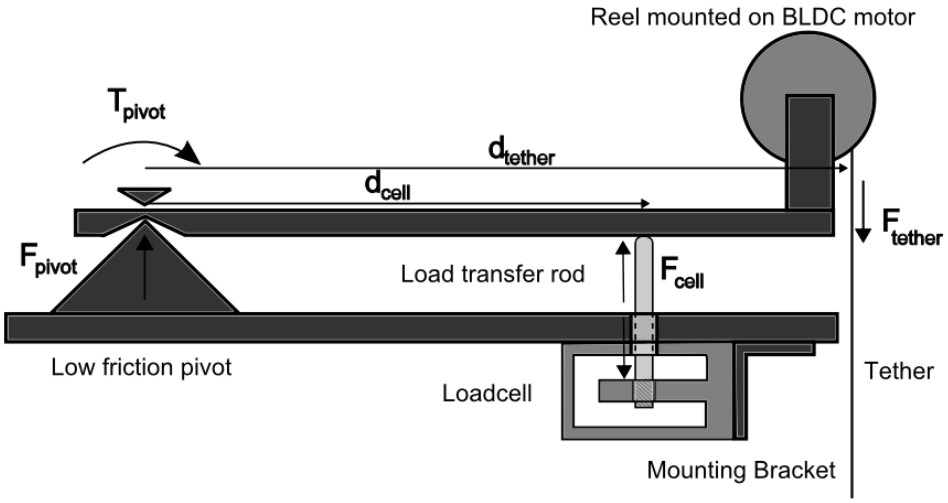

Figure 4.2: Illustration of loadcell integration into system.

This system was built and tested. A Futek Q10542-168 parallelogram load cell was used and its datasheet is attached in Appendix B.3. A Perspex base and mounting plate were designed and manufactured. A spool containing the tether was mounted on a BLDC motor which was in turn mounted on the mounting plate. This plate was placed on the pivot point as illustrated in Figure 4.2. Due to constraints in manufacturing capabilities, the BLDC motor could not be aligned perfectly with the axis of the spool, which caused vibrations and unwanted disturbance forces in the system. To solve this problem, gears were added to the spool and the motor was mounted next to the spool, instead of in line with it. This provided some margin for error in alignment, considering that the depth of the teeth of the gears could provide the necessary play needed to absorb the effects of misalignments. An image of the system is shown below.

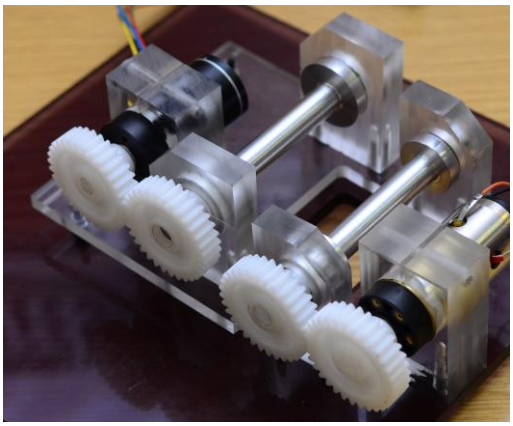

Figure 4.3: System identification hardware.

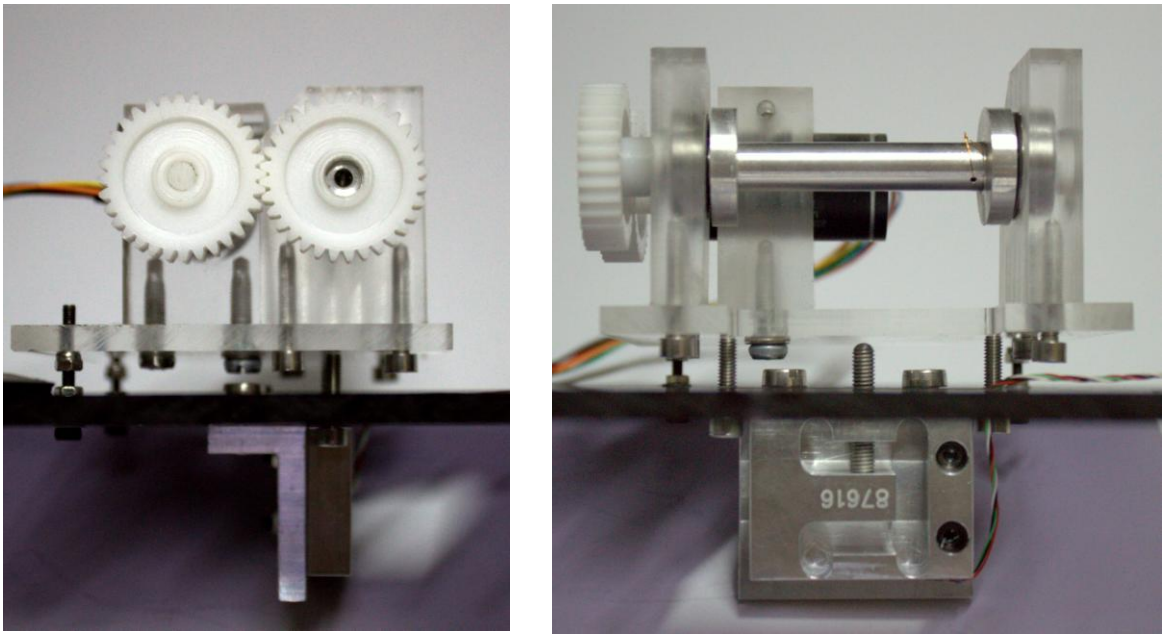

Figure 4.4: Loadcell integration into deployment system.

As illustrated in Figure 4.2 the tether force can be determined with a loadcell measurement by Equation (65). The equation is derived by simply taking the sum of the moments around the pivot axis to compute T_{pivot} . The loadcell outputs a voltage proportional to the force applied to it, and the tether force could then be calculated by using the following equation:

$$\mathrm{F}_{tether} = F_{cell}\frac{d_{cell}}{d_{tether}} = K_{cell}V_{cell}\frac{d_{cell}}{d_{tether}} \quad (65)$$

Using the system to perfectly compensate for the effects of gravity proved complex. Unforeseen disturbances originating in the gears, the sensitivity of the loadcell to temperature effects, and loadcell sensitivity to electronics noise in the supply voltage all contributed to the inaccuracies in the loadcell measurements. After many iterations and improvements of the system, the noise could be minimised, but accurate control still proved challenging. Since this forms only a small part of the study, the idea had to be abandoned after a considerable amount of time was spent on it. The construction of the mechanism and the integration of the loadcell into the system did however serve a purpose in a later part of the study discussed in Section 4.2.2.1.2.

4.2 Design

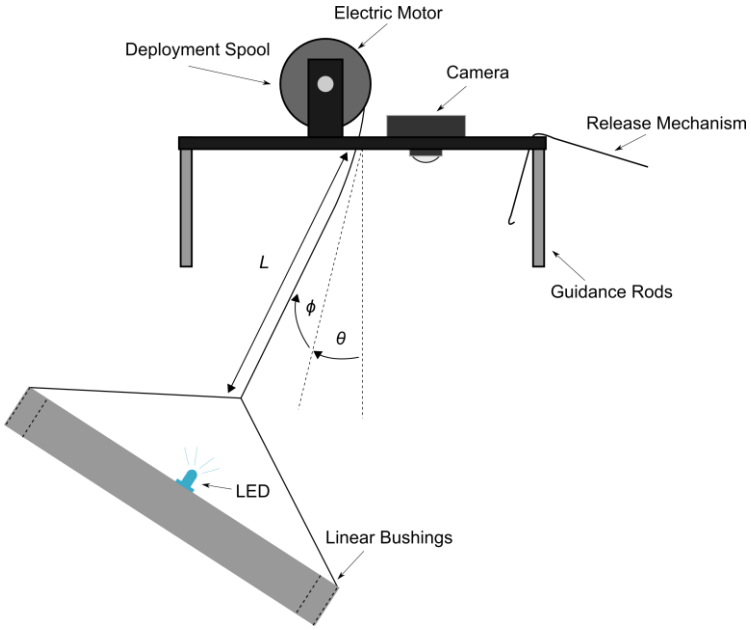

Figure 4.5: Test setup for tether angle sensor and deployer.

4.2.1 Tether Angle Sensor

4.2.1.1 Electronics

4.2.1.1.1 Circuit Design

The circuit for using the OV9653 camera module was based on a design done by [24]. The system was adapted to accommodate an ARM Energy Microprocessor instead of a Microchip PIC processor. Voltage translation hardware was also added to accommodate camera modules using different voltage levels. The address and data bus sizes were increased to enable higher resolution cameras with higher colour depth.

The general layout and interface diagram of the system is shown in Figure 4.6. The MCU serves as central unit controlling the operation of the camera. The MCU has direct communication to the camera through the i2c bus for setting the camera registers and so configuring the camera to the relevant operating modes. Further the MCU controls the FPGA to operate in the appropriate mode. Data output by the camera is routed through the FPGA to the SRAM. The FPGA is driven by the camera clock output which also drives the address counter in the FPGA. The camera requires a clock input and this input is generated by a clock divider implemented within the FPGA. Lastly the MCU has a connection to the UM232R module for ***Universal Asynchronous Receiver/Transmitter*** (UART) communication to a PC.

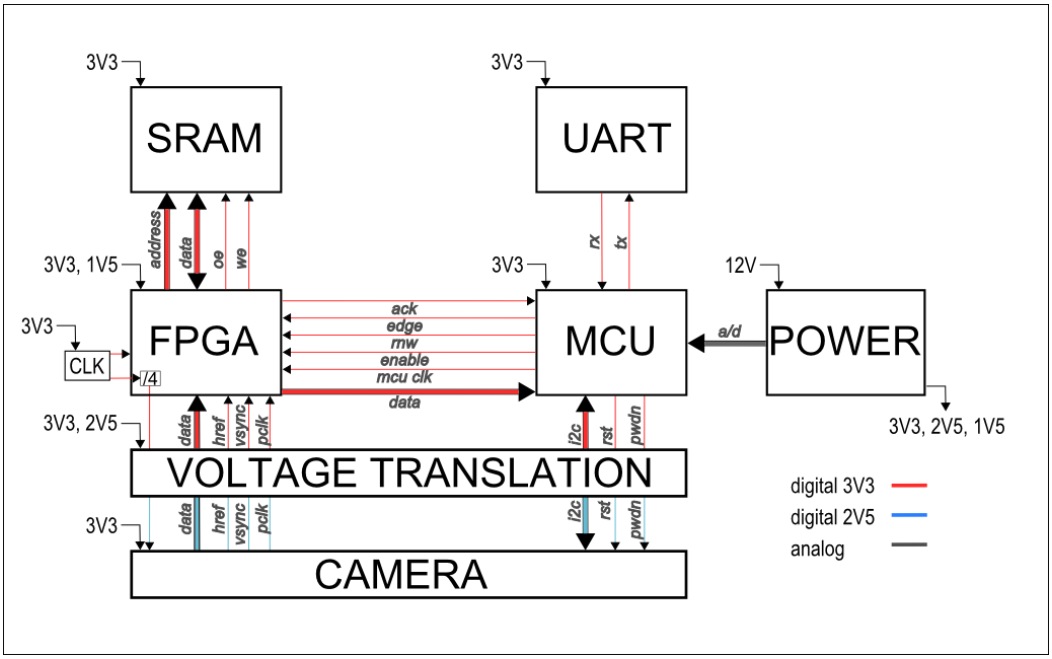

Figure 4.6: Imager electronics interfaces.

4.2.1.1.2 Camera Description

The camera used for the relative sensor is an Omnivision AA9653 Camera module. The module consists of passive electronics, voltage regulators, and an OV9653 CMOS image sensor. This is a 1.3MP sensor with maximum resolution of 1280x1024 (SXGA). The pixels in the sensor are arranged in a Bayer RGB pattern.

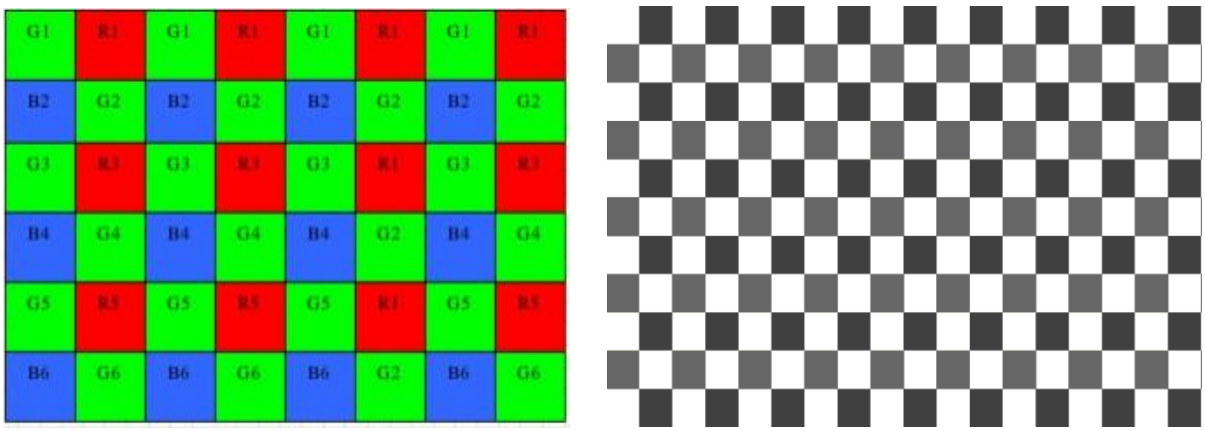

Figure 4.7: Demonstration of Bayer RGB pattern in OV9653 camera module.

Figure 4.7 (left) shows the Bayer arrangement in theory and Figure 4.7 (right) shows a sample image of a white surface taken with the camera with its red, green and blue gains all set to different values and the camera set to Raw RGB output mode. The different colour gains enable differentiation between the pixels by looking at their intensity and revealing the Bayern pattern.

The configuration and control of the camera registers are done through a ***Serial Camera Control Bus*** (SCCB) interface. This communications protocol works roughly the same as i2c with the main difference being that in SCCB the 9th bit, which is an acknowledged bit in i2c, is a 'don't-care'-bit. A short list of the crucial registers that must be set to setup the camera is listed in Appendix A.1.

The sensor offers Raw RGB, RGB (GRB4:2:2), YUV(4:2:2) and YCbCr(4:2:2) output formats. These are all different colour spaces outputting linear combinations of the red, green, and blue data. YUV and YCbCr colour spaces are mainly used for improving image transmission by encoding the data in such a way that loss of accuracy during transmission is minimal when taking into account the human perception thereof. This is not applicable when taking grayscale images; for the application in this study the compression or 'smudging' of the pixels are unwanted and a raw output is required. The raw RGB mode is therefore used where each pixel's intensity is transmitted as a separate 10-bit number.

The camera outputs data through a 10-bit bus, with timing bits for the pixel clock, vertical sync, and horizontal sync acting as clocks for capturing images. Figure 4.8 illustrates the timing of a typical capture output sequence from the camera. In essence, VSYNC indicates the start of a new photo, HSYNC the start of a new line in the photo, and the pixel clock the next pixel in the line.

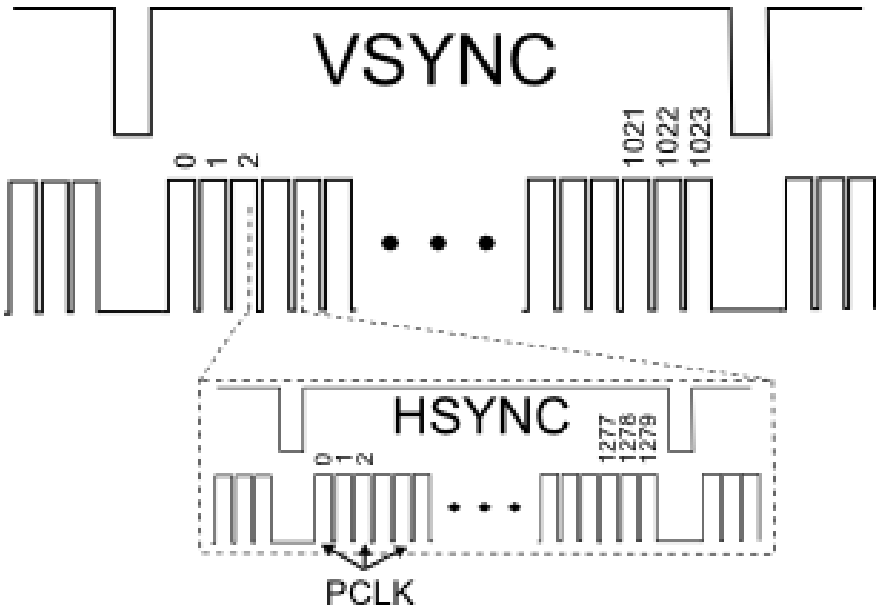

Figure 4.8: Camera timing protocol.

4.2.1.1.3 LED Description

The LED used for the relative sensor has to be visible on the image sensor at a distance of 500m. The requirements for this to work, is discussed in Section 3.4.1.1.

The choice was made to use a lens with an AOV of 40º. From Equation (42) and considering that the OV9653 sensor has a physical width of 3.28mm

$$f = 5mm$$

As discussed in Equation (45), the LED will illuminate exactly one pixel on the OV9653 sensor, which has a pixel size of $3.18\mu m \times 3.18\mu m$, if the 3mm LED (Appendix B.2) is a distance larger than *D* away from the sensor where D is calculated as

$$D = 4m$$

Thus at 500m the LED will not illuminate more than a single pixel on the sensor. With an typical LED luminous intensity of 7.15 Candela (Appendix B.2) and a lens diameter of 5mm, the illuminance of a single pixel can then be calculated according to Equation (48) as

$$E_v = 220\ lux$$

With the sensitivity of the sensor at $0.9\ V/lux \cdot s$ and an exposure time of 1ms, the LED will induce a voltage of 198mV. The sensor is rated with a dark current of 30mV/s which will result in a sensor reading of 0.03mV. The light from the LED will therefore be disguisable from the background of space.

One of the brightest and largest stars that may come in view of the camera sensor is Betelgeuse. As mentioned in Section 3.4.1.1 it has a luminance intensity of 3.3×10^{32} Candela and is at a distance of 642.5 light years, which is about $6 \times 10^{18}\ m$. From Equation (48) the illuminance of the star on a pixel of the sensor can be calculated as

$$E_v = 70\ lux$$

The illuminance of the LED will be 3 times as bright as the brightest star and ensures that the LED will always be distinguishable from the stars. The intensity of sunlight reflecting from planets in our solar system is not considered here and may pose a larger problem. In the case where these reflections are found to interfere with the operation of the sensor, the sensor can be disabled for a brief period of time.

For testing purposes a lens with focal length of 6mm was available and was used. This decreases the field of view of the camera, but does not affect the performance of the system further and serves as a good validation test for the system.

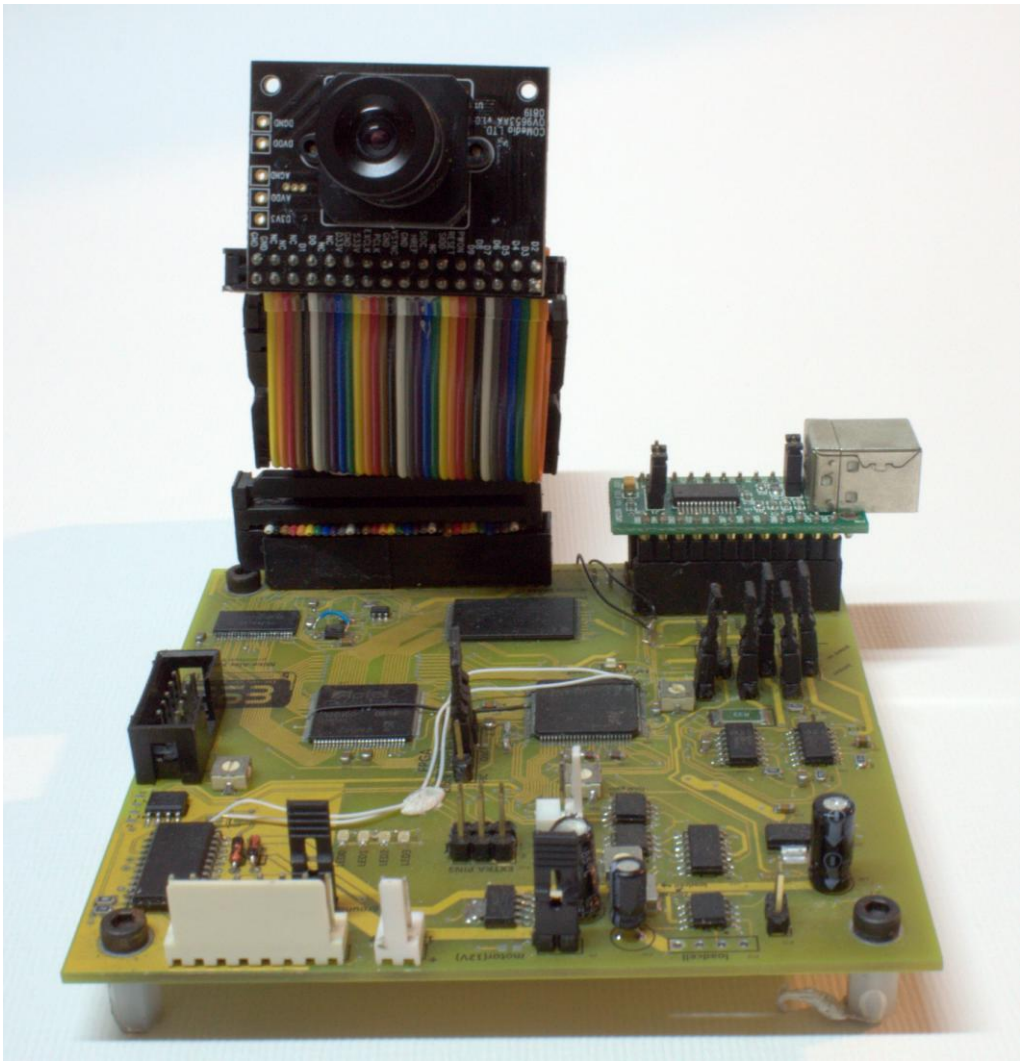

Figure 4.9: Camera hardware.

4.2.2 Deployer

4.2.2.1 Mechanics

4.2.2.1.1 Mechanical Structure

A mechanical structure was designed to house the motor, deployment spool, camera, and launcher.

As part of the launcher system, a guidance mechanism had to be implemented to ensure linear, smooth motion of the deployed satellite. Without such a system, misalignments in the launcher may cause unwanted rotations during launch. Four hardened steel rods paired with linear bushings where used as guides. To ensure smooth operation of this system, the rods need to be perfectly straight, and all four rods have to be mounted near parallel to each other. This was achieved with high accuracy by using hard steel rods which resist bending, and manufacturing of the housing which holds the rods with high precision using CNC

technology. The technical drawings used to create the base and the bearing and motor brackets are attached in Appendix C.

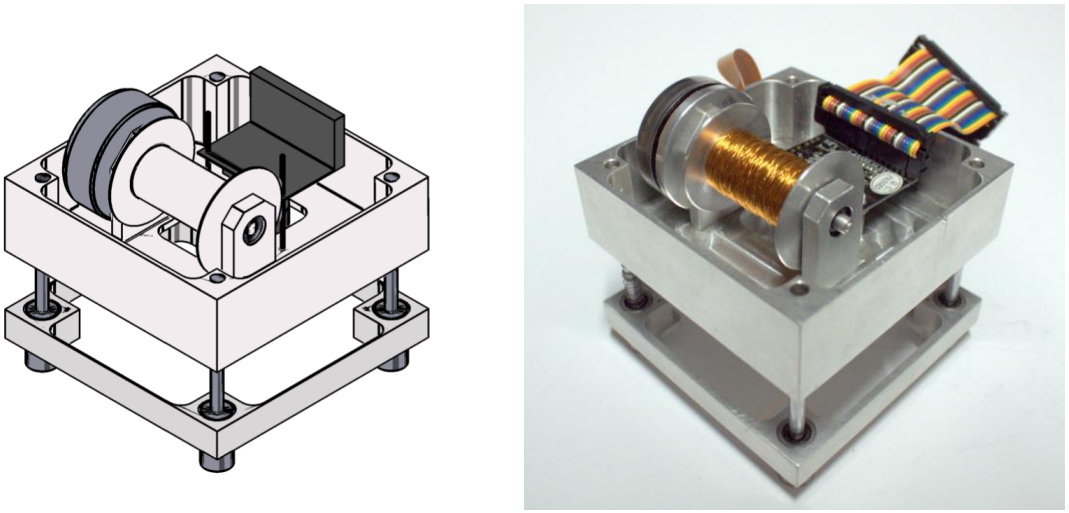

Figure 4.10: Deployer hardware.

The structure was built to resemble the CubeSat form factor to gain better understanding of the sizes involved in building parts for a CubeSat.

4.2.2.1.2 System Identification

Before attempting to control the deployer prototype, the system had to be investigated. The basic equations governing the motion of the system were done, but there were still uncertainties about the effect the motor driver would have on the system and the elastic behaviour of the tether. To further investigate the system, the test setup which was discussed in Section 4.1.1 was used. The loadcell was used to directly measure the tether tension and using this measurement in combination with system identification techniques, the system's resonant behaviour could be studied.

This was done by feeding different torque input references to the ***Brushless Direct Current*** (BLDC) motor and measuring the tether tension as output. In particular, the system was tested with different frequency sine waves as input. By sweeping across the frequencies and measuring the ***Root-Mean-Squared*** (RMS) value of the oscillations that resulted from the motor torques, the resonant frequencies of the system could be identified. At each frequency the system was left for a few seconds to eliminate transition effects. The output signal was then sampled for a few seconds, the RMS value determined, and the value stored.

The results were then plotted on a logarithmic scale to represent a bode frequency plot.

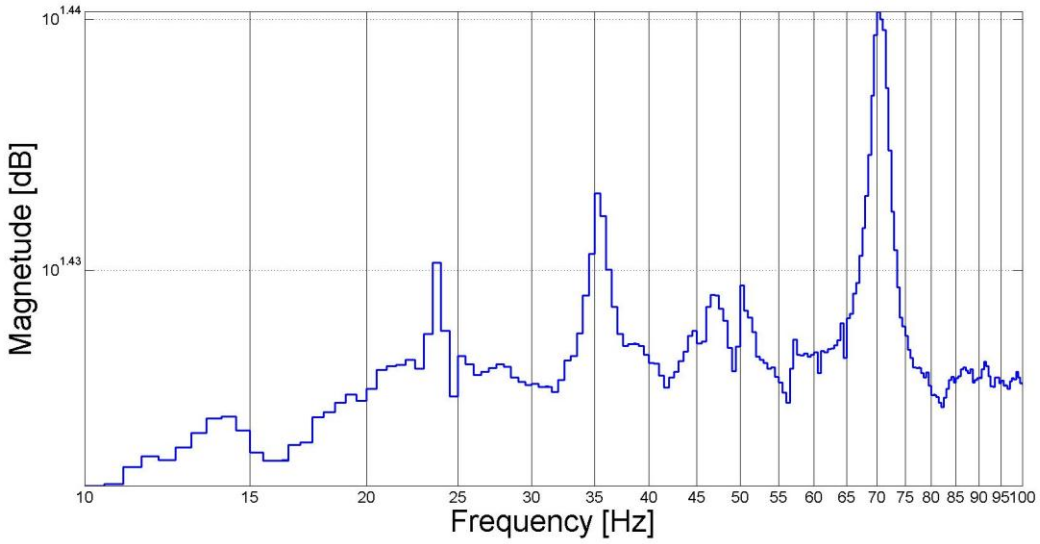

Figure 4.11: System identification frequency analysis of deployer.

The limitation of this method is that the phase of the system was not investigated. The goal was, however, only to identify the resonant frequencies of the system to gain insight into the dominant modes of the system. As shown in Figure 4.11 the resonant frequencies of the system are located at roughly 24 Hz, 35 Hz, 48 Hz and 70 Hz with the 24 Hz and 48 Hz pair, and the 35 Hz and 70 Hz pair, both seeming like harmonics of the same fundamental source.

In the test setup a one metre length of tether was used with a mass of 100g attached to it. When Young's modulus of copper is used as described in Section 3.3.6.3, the spring constant of the piece of tether can be determined. The natural frequency of the spring-mass system can be derived as [25]

$$\omega = \sqrt{\frac{k}{m}}$$

With the copper wire and the given specifications, this should be in the order of 40 Hz. The conclusion was made that one of the pairs of harmonics is due to this tether elasticity.

The mechanical setup was done in such a way that the connection between the tether and the end-mass was not at the COM of the body. This resulted in body rotations of the end-mass as is predicted for the case of a tethered satellite. This basically forms a pendulum with length equal to the distance between the connection point and the COM of the body. The natural frequency of a pendulum in earth gravity is given as [25]

$$\omega = \sqrt{\frac{g}{L}}$$

The object used as end-mass was about 5mm in length and according to calculations, should have a resonant frequency of about 10Hz.

The values calculated here are not exact nor exactly equal to the values obtained from the frequency analysis of the system, but they are close, providing possible explanations for the results. The information taken from these tests are not exact either, but rather that the elastic resonant frequencies of the tether are at a relatively high frequency. Control of the tether deployment will be done at very low speeds with a settling time for the speed controller of about 15s. With this slow control, these tests provide the assurance that the elastic mechanics of the system will have an insignificant effect on the control dynamics.

4.2.2.1.3 Separation

When the satellites are close together, there is not a significant gravity gradient force to pull the satellites apart. The two satellites thus have to be launched apart with an initial velocity to start the deployment process. Two possible mechanisms to achieve reliable separation and provide the required initial deployment velocity are considered.

The first option is the use of a gas launcher. The concept relies on a compressed gas canister which is pierced at the moment of launch, to propel the satellites apart. The launcher will still need to have a mechanism keeping the satellites together during launch and initial operation, but with the canister not yet pierced, the mechanism will be under no tension and will operate with low control effort and high reliability. The proposed concept is illustrated in Figure 4.12.

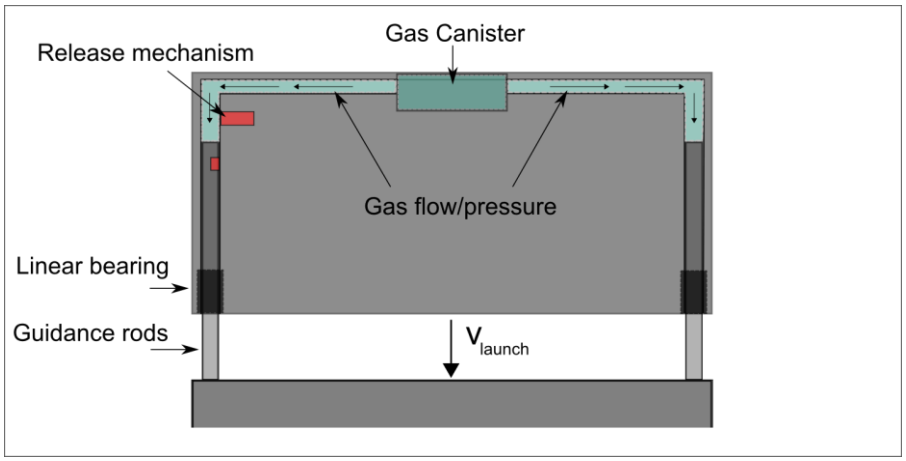

Figure 4.12: Illustration of gas powered launcher.

The problem with this solution is caused by the effect the leftover gas has on the system. After the deployment is done and the gas canister is punctured, the entire satellite will be exposed to gas particles. To reduce the negative effect these particles might have on the rest of the satellite, an inert gas such as Argon may be used. The particles floating with the satellite in orbit will, however, still potentially cause damage within the satellite.

A simpler solution is to have a spring-loaded release mechanism to start the deployment. The problem with such a configuration is that the design of a reliable release mechanism is complicated. With the tension of the spring pressing against the release mechanism, the friction created makes the system vulnerable to cold welding which may cause the mechanism to fail. To solve this problem, the electric motor which is used for the deployment control, is used to momentarily remove/reduce the tension on the release mechanism by pulling the

satellites together. By doing so, some of the force exerted by the spring-loads is cancelled by the electric motor. During this period the release can be toggled without having a large tension force on it and therefore operating more reliably.

Such a release mechanism was implemented for tests on earth. The release involves a balancing steel rod which keeps the satellites together when under tension from the spring load. When the tension is removed from the rod by pulling the satellites together using the electric motor, the rod is free to move under its own gravitational force which causes it to rotate to such a position that it no longer obstructs the satellites from separating. The sequence of events for toggling the release is shown in Figure 4.13.

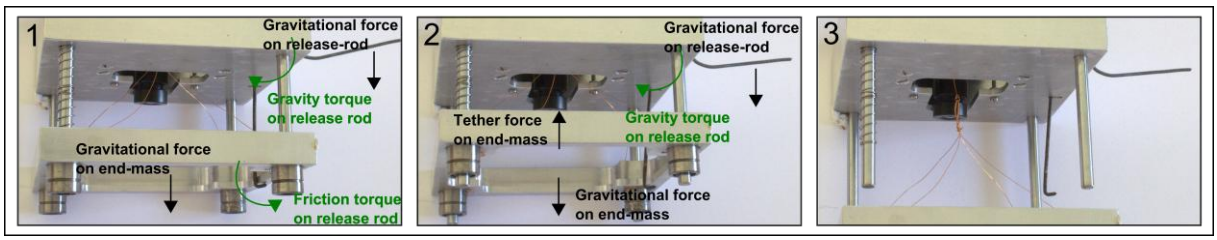

Figure 4.13: Deployment sequence illustration.

In this case the gravitational force on the rod provides the torque needed to rotate it into such a position that it no longer obstructs the motion of the deployed satellite. When orbiting in space, this gravitational force will not be present and a spring load can rather be used to rotate the release pin. It must be noted that this was just a basic design serving as demonstration of the concept.

4.2.2.2 Electronics

4.2.2.2.1 Circuit Design

The same processor and power electronics used for the tether angle sensor was used to control the tether deployment. For controlling the BLDC motor, a motor driver was added which contains the switching electronics needed to drive the motor. To be able to use the small voltages generated by the loadcell, ***Instrumentation Amplifiers*** (INA) were used to amplify the loadcell outputs in such a way that the full A/D range is utilised. This also involved adding some tuning potentiometers to scale the signal and add DC-offsets to accompany AC voltage signals. Figure 4.14 shows a diagrammatic representation of the system.

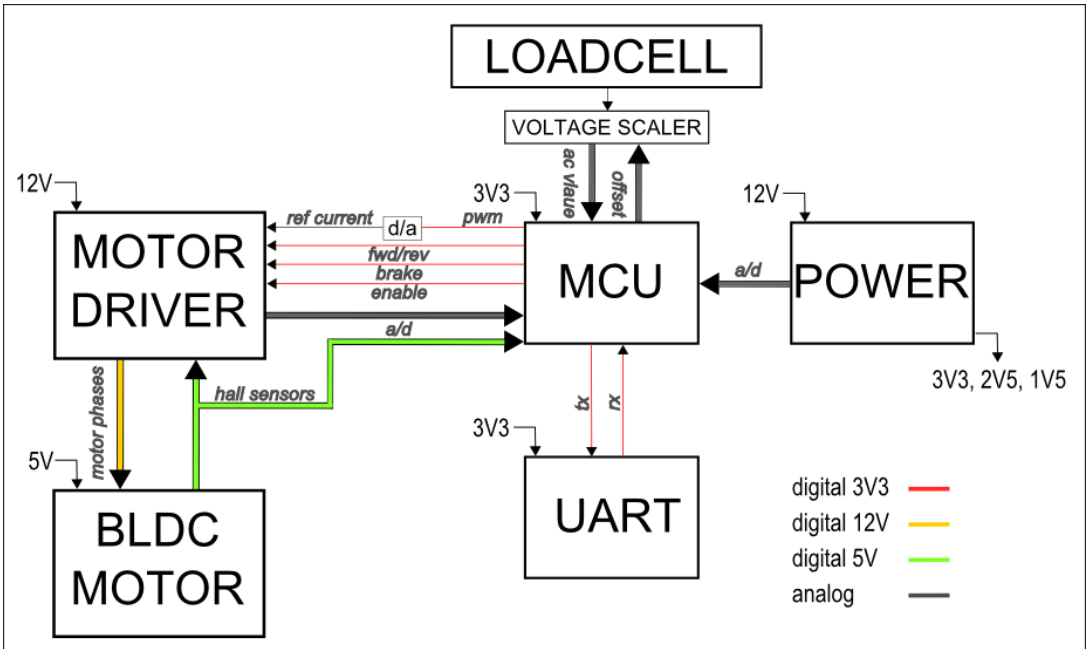

Figure 4.14: Deployment electronics interfaces.

The motor driver does full ***Pulse Width Modulated*** (PWM) current control. A DC reference voltage is supplied and the driver then controls the switching electronics in such a way that the current through the motor is driven to this reference value. This control current for the motor driver is determined by the control algorithm run on the MCU. The MCU generates a PWM signal with duty cycle proportional to the magnitude of the desired current. This PWM signal is then placed through a low-pass filter to create the DC reference signal required from the motor driver. The resolution, to which the MCU can change this DC voltage it is supplying, depends on the resolution to which it can vary the duty cycle of the PWM signal. With this limited resolution available from the MCU in mind, the design was adapted. During control of the deployment when tested on earth, the electric motor must constantly provide an offset torque to cancel the effects of gravity. The control of the deployment speed is done by subtracting or adding small signals to the offset, and by doing so speeding up or slowing down the deployment. The range of motor torques that is needed is thus the maximum signal required for control plus the offset voltage for cancelling the effects of gravity. The gravitational offset torque is large in comparison with the control torques. The range of torques required from the motor is therefore in this case mainly determined by this offset. The size of the discrete steps in reference voltage the MCU can supply, is determined by the total range of voltages that is required, divided by the resolution the MCU can supply. In the case where the control signal includes the torque for cancelling the effects of gravity, the resolution is

$$\Delta\tau_{control} = (\tau_{offset} + \tau_{control})/K_{MCU\ Resolution} \quad (66)$$

Because the offset torque is so large, the discrete steps in magnitude of the control signal are mainly determined by the offset torque. This low resolution influences the quality of the control that can be done on the deployment speed. A solution to this problem was to add buffer and amplifier electronics to manually compensate for the offset torque. ***Operational Amplifiers*** (OPAMPS) and potentiometers were used to add an offset voltage to the MCU control signal, with magnitude determined by manual tuning of a potentiometer. By tuning the

potentiometer, the magnitude of the offset added to the control signal can be controlled. Before using the MCU to control the deployment, the potentiometer can be tuned until the offset is close to the force required to compensate for the effects of gravity, and the mass hanging from the tether is almost 'weightless'. The schematic for this configuration is shown below.

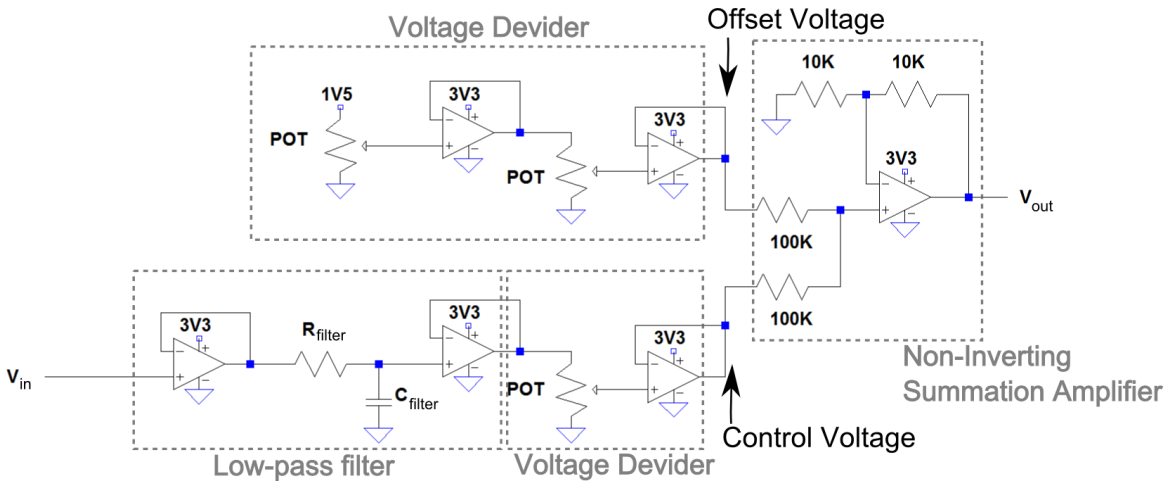

Figure 4.15: Motor Driver Scaling Electronics

With this configuration, the offset to compensate for gravity is supplied by tuning the potentiometers. The range of the MCU control voltage is then only the control signal plus a small residual offset which may still be present, because of the incorrect tuning of the offset voltage. The control resolution is dramatically increased by doing so.

4.2.2.2.2 Motor Driver

To drive a BLDC motor, complex switching electronics are required to drive the correct phase of the motor at the correct time. This requires reading the Hall sensors of the motor to determine the position of the magnets and then driving the correct phase. To do this, an integrated DMOS driver is used which contains all switching electronics to do current control of a BLDC motor. The L6235D driver is used and its datasheet is attached in Appendix B.1. The driver implements a constant off-time PWM current controller which is set up by primarily a capacitor and resistor pair, used to determine switching times of the transistors.

This RC-network determines the rise and fall times of the signal controlling the switching electronics. The transistors are either switched on to drive the motor directly, or in the case the transistors are switched off, the motor current is circulated through freewheeling diodes. This off-time is determined by the RC_{off} time constant. The off-time t_{off} is calculated as follows:

$$t_{off} = 0.6R_{off}C_{off} + t_{dt}$$

where t_{dt} is a $1\mu s$ dead time which prevents cross-conduction within the circuitry

$20\text{k}\Omega \leq R_{off} \leq 100\text{k}\Omega$ and

$0.47\text{nF} \leq C_{off} \leq 100\text{nF}$.

The choice of t_{off} was not design critical. The main consideration when selecting the component values, was keeping the switching frequency above the audible range for convenience. The values $R_{off} = 36\text{k}\Omega$ and $C_{off} = 1.5\text{nF}$ were chosen for a switching frequency of roughly 30 kHz.

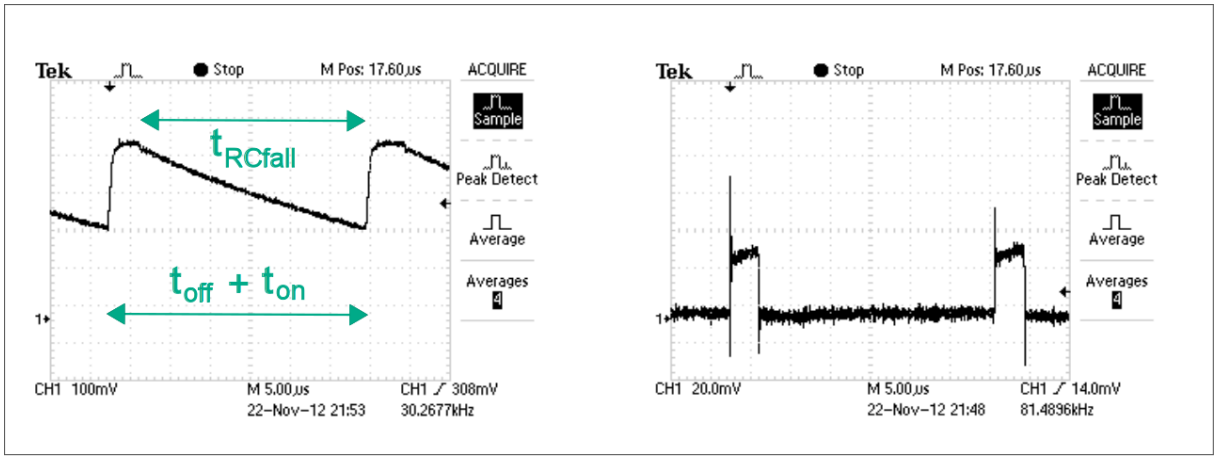

Figure 4.16: Oscilloscope measurements of motor driver electronics. (V_{RC} *left and* V_{Sense} *right*) .

The oscilloscope measurements of the RC-voltage and the sense voltage show that $t_{RCfall} = 28\mu s$ and a period of $t_{switch} = t_{off} + t_{on} = 33\mu s$ corresponding with a switching frequency of 30.3 kHz.

For further reference on these switching characteristics, the L6235D driver's datasheet is attached in Appendix B.1

4.2.2.2.3 Electric Motor and Hall Sensors

A BLDC motor was chosen for the deployment mechanism for the following reasons:

- low friction
- high torque/size and
- no commutator contact/wear.

The requirements set for the motor were:

- enough torque to lift 100g mass against gravity when connected to a 20mm radius spool and
- input voltage between 8V and 12V (according to motor driver and power supply limits).

A Maxon Motors 12V EC45 Flat BLDC motor was chosen. With a stall torque of 260 mNm, the motor will be able to lift more than a kilogramme when placed on a reel with diameter of 20mm. A datasheet of the motor is attached in Appendix B.4.

For an actual tether mission, the forces present in the tether will be magnitudes smaller than those under earth's gravity conditions and the required motor torque is therefore also smaller. The friction force in a motor usually scales with its size and power and for a tethered mission a much smaller motor than the EC45 is needed. The suggested motor is a Faulhaber series 1509 BLDC motor. This motor is lighter and physically smaller than the Maxon motor, has dynamic friction of only 2.6×10^{-9} Nm, and is thus very well suited for the tether mission. A datasheet of the Faulhaber motor is added in Appendix B.4.

4.3 Integration & Testing

4.3.1 Circuit Design

The ***Printed Circuit Board*** (PCB) design was done in two stages. A first prototype was done and tested before a complete second version was designed. First, the motor driver and camera electronics were separated for simplicity, and because of limited local PCB manufacturing capabilities. This separation also protected the digital electronics from the larger currents the motor electronics draw. Below is a picture of the camera electronics (bottom), the motor driver electronics (top left) and the loadcell amplifiers (top right).

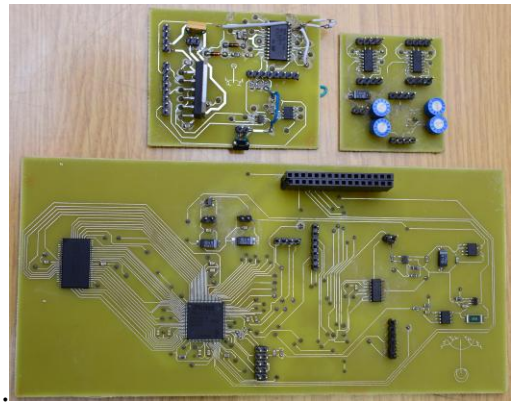

Figure 4.17: First iteration of PCB design.

The second prototype combined these boards into one. From lessons learned during the first iteration, jumpers were added in order to isolate different parts of the board. To still ensure separation between the power and digital electronics, two ground planes were used. The motor electronics were placed on the one, and the digital electronics on the other. The ground planes are connected at only one location with a resistive connection, thus supplying some filtering of voltage spikes that may be present on the power ground plane. Figure 4.18 shows the PCB design file and a picture of the second PCB iteration.

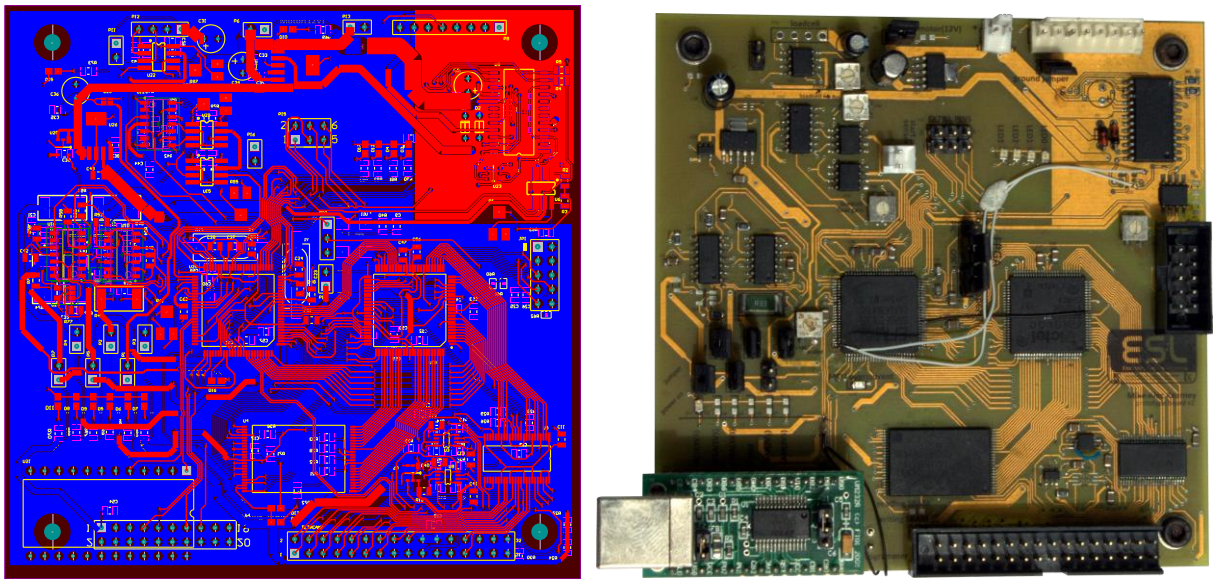

Figure 4.18: PCB design and manufacturing.

After the manufacturing of the PCB some manual modifications were done. These include:

- swapping of the TX and RX lines from the UM232R UART module,
- rerouting of the Hall sensor outputs to MCU quadrature detect pins,
- addition of ‘Enable’-line to the level-shifter for isolating the camera module, and
- adapting of MCU oscillators to fit on incorrect footprints.

4.3.2 Software

4.3.2.1 MCU Firmware

The main while-loop in the MCU routine consists of 4 functions, one for handling UART commands, one for motor control, one for camera control, and one for sending sensor data through UART back to the PC. Below is a flow diagram of the program.

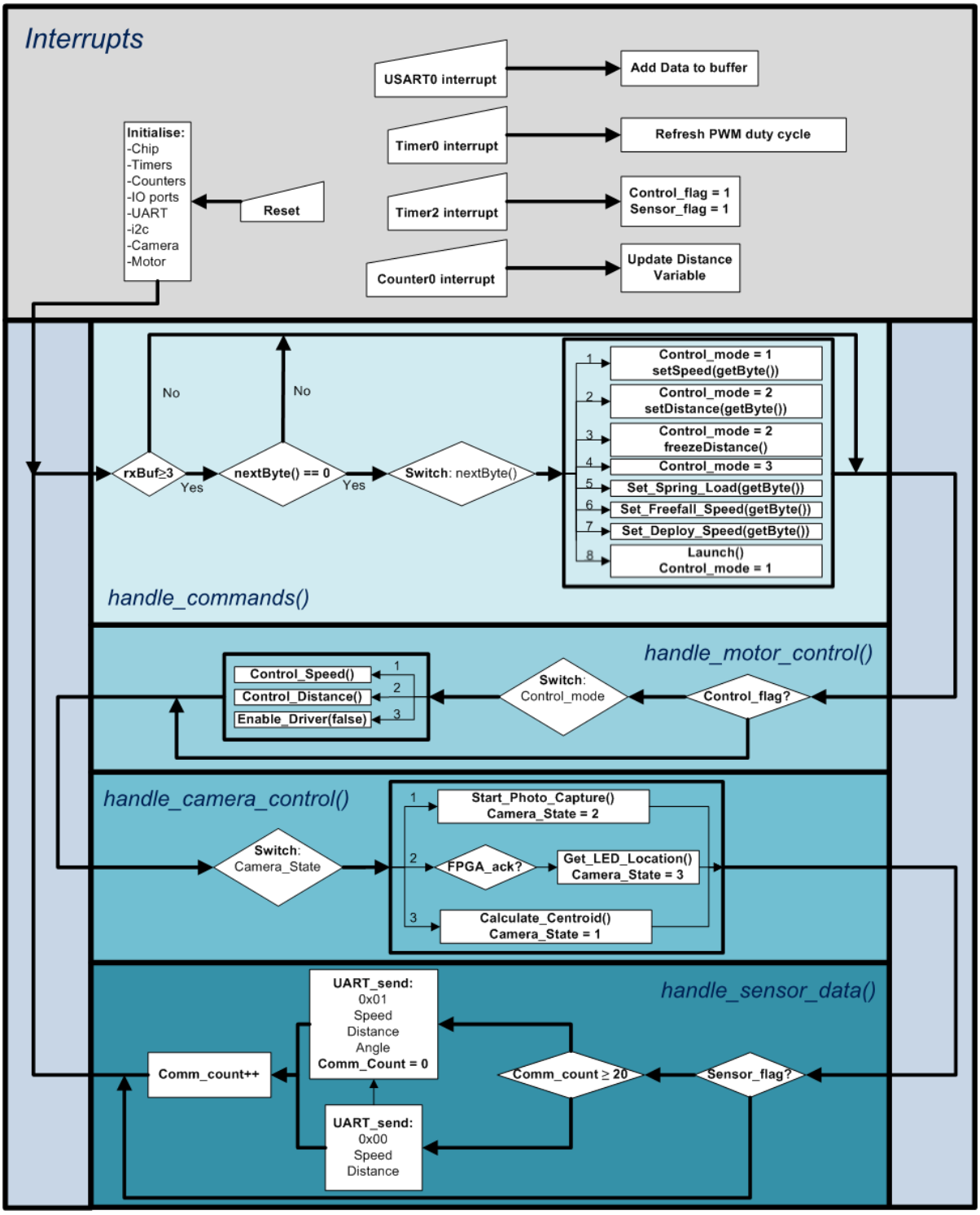

Figure 4.19: MCU Main Loop Structure.

The individual routines are discussed below.

handle_commands():
This routine handles user control data sent through the UART from the PC. These commands have fixed length of three bytes and have a structure as shown below:

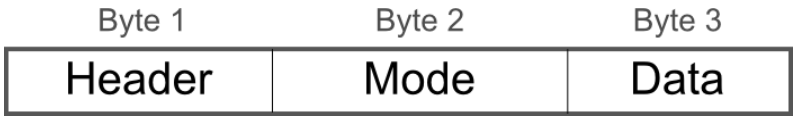

The list of commands to send to the MCU includes:

Byte 1	**Byte 2**	**Byte 3**	**Function**
0x00	0x01	*Speed*	Set to speed control with speed-reference of S*peed*
0x00	0x02	*Distance*	Set to distance control with distance reference of *Distance*
0x00	0x03	X	Set to distance control with current distance as reference
0x00	0x04	X	Cut motor
0x00	0x05	*Load*	Set spring load variable for deployment (for launch routine)
0x00	0x06	*Speed*	Set speed to which the system must free fall(for launch routine)
0x00	0x07	*Speed*	Set speed to which the system must control(for launch routine)
0x00	0x08	X	Do launch routine

handle_motor_control():
Control algorithms are only run every 30ms. These routines are triggered by software interrupts using the timer functions built into the MCU. During the interrupt a flag is set to signal to the main loop that the control routine is due. During the control routine the type of control that the system currently needs to perform, is executed. The three modes are:

- Speed control - The speed of the system is determined by filtering the quantised distance measurement from the motor's Hall sensors. This speed is then compared to a reference speed and PI control is implemented.

- Distance control - This controller compares the current deployed distance with a reference distance, and then calculates a proportional value for the speed controller.

- Safety Cut - In some cases the motor needs to be totally cut for safety reasons and in this case the motor driver is totally disabled.

handle_camera_control()
The camera sensor provides data at a lower rate and new data is available only every 200ms. Getting data from the camera happens in 3 phases namely taking a picture and storing it on the SRAM, downloading the LED location to the MCU, and calculating the centroid to determine the exact position of the LED. Saving the picture to the SRAM takes more than 30ms, and the system can therefore not perform motor control and other functions while a picture is being taken. A state machine is thus implemented where the capture of a new image

is initialised and the image controller is then placed in a state where periodic checks are done to determine if the image is successfully stored. While the image is being stored and the centroid being calculated by the FPGA and SRAM, the MCU is consequently free to perform other tasks.

`handle_sensor_data()`

The data from the MCU is sent through UART in two stages. Every 30ms a two packet data set is sent, containing the most up to date deployment distance and speed. Every 210ms a three packet data set is sent, containing the most up to date deployment distance and speed, and also the new tether angle calculated from the LED position from the camera. The structure of the two packet sets are shown below.

Packet 1:

Byte 1	Byte 2	Byte 3	Byte 4
0x00	Speed	Distance(MSB)	Distance(LSB)

Packet 2:

Byte 1	Byte 2	Byte 3	Byte 4	Byte 5
0x00	Speed	Distance(MSB)	Distance(LSB)	Angle

The speed and angle measurements are cast to a byte when sent. The actual variables in the MCU are of type `float`, but this accuracy is not required since the display of the angles and speeds is limited to the resolution of the screen. The values sent here are only to serve as indication of the size and does therefore not require 4 byte accuracy of a `float`.

4.3.2.2 FPGA Firmware

The FPGA software layout designed by [24] was used with minor changes made to accommodate a different camera module. The basic structure of the FPGA is shown in Figure 4.20.

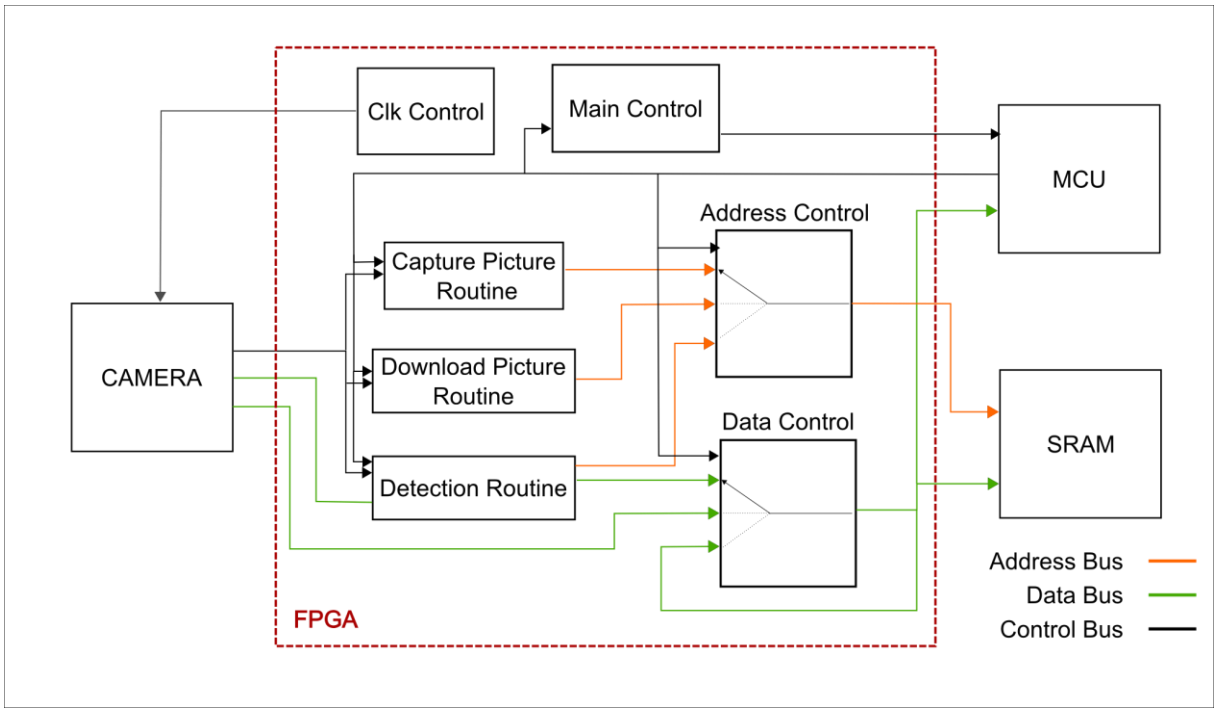

Figure 4.20: FPGA layout

Listed below is a log of changes made to the original design:

- Increased bus size for address bus.
- Implemented customized state machine for detection.
- Changed ‘acknowledge’ protocol between FGPA and MCU.
- Added VSYNC control pin from camera to signal start of new photo.
- Added clock divider for camera clock input.

When tracking the LED the FPGA is used in detection mode, and the detection routine is used. During this routine, the data that is saved to the SRAM from the camera is checked by parallel FPGA gates to locate the LED in the image. The location of the LED is latched in FPGA gates until the entire image is saved. When the image capture is completed and the MCU has received the FPGA ‘ACK’-command to signal that new data is available, the MCU initiates the transfer of only pixels near LED location, and no extra computation time on the MCU is required to find the LED position. The detection algorithm can therefore be run as fast as the camera can provide image data and is consequently limited only by the camera clock speed and exposure time.

4.3.2.3 Application Software

To control the hardware that was developed for the Tether Angle Sensor and for the deployer, an application was needed to gather and display data from the hardware on a PC. The application should mainly provide a UART communication link to send commands to control the hardware and receive sensor data from it. Java was chosen as programming language since it provides simple GUI interfacing to be done with minimal effort and because it has a very good built in serial package for sending and receiving data through the serial port for the UART communication. Figure 4.21 shows a screenshot of the application displaying sensor data.

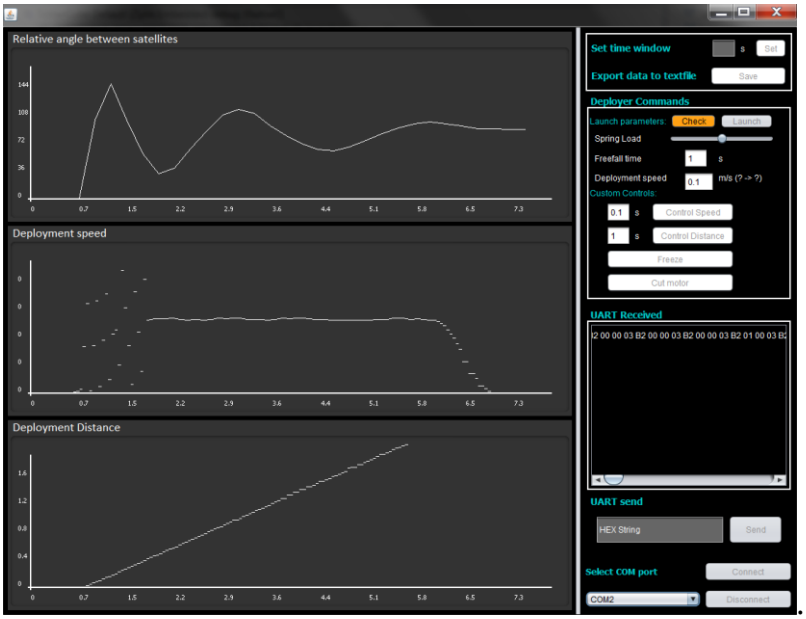

Figure 4.21: GUI application software screenshot

The application displays sensor data sent from the MCU. The MCU receives a real-time-, but quantised-version of the deployment distance from the motor Hall sensors, and image data every 200ms. The deployment distance data is used to calculate the deployment speed every 30ms during the control routine of the motor, and new deployment speed information is available every 30ms. The data is sent from the MCU in two different packets as specified in Section 4.3.2.1. The application handles these packets accordingly and updates display data in the display windows.

The application also provides control of the system through the GUI controls shown in Figure 4.21. Moreover the applications show all incoming UART data in the "UART Received"-window, and provide the option to send manual UART commands to the MCU in the "UART send"-window. Available COM ports are detected automatically and the option of COM port to connect to is given in a drop-down list.

4.3.3 Tether Angle Sensor Testing

4.3.3.1 Exposure adjustment

The sensor offers four automatic settings namely, ***Automatic Exposure Control*** (AEC), ***Automatic Gain Control*** (AGC), ***Automatic White Balance*** (AWB), and ***Automatic Black-Level Calibration*** (ABLC). For the purpose of taking photos in normal light of normal scenery during testing, these automatic settings work as expected. For the purpose of taking pictures of a LED with a black background, the AEC and the AWB are switched off and the optimal values for these settings are determined. Figure 4.22 shows pictures taken with exposure set for normal lighting (left) and for tracking the LED with the camera set to minimum exposure (right).

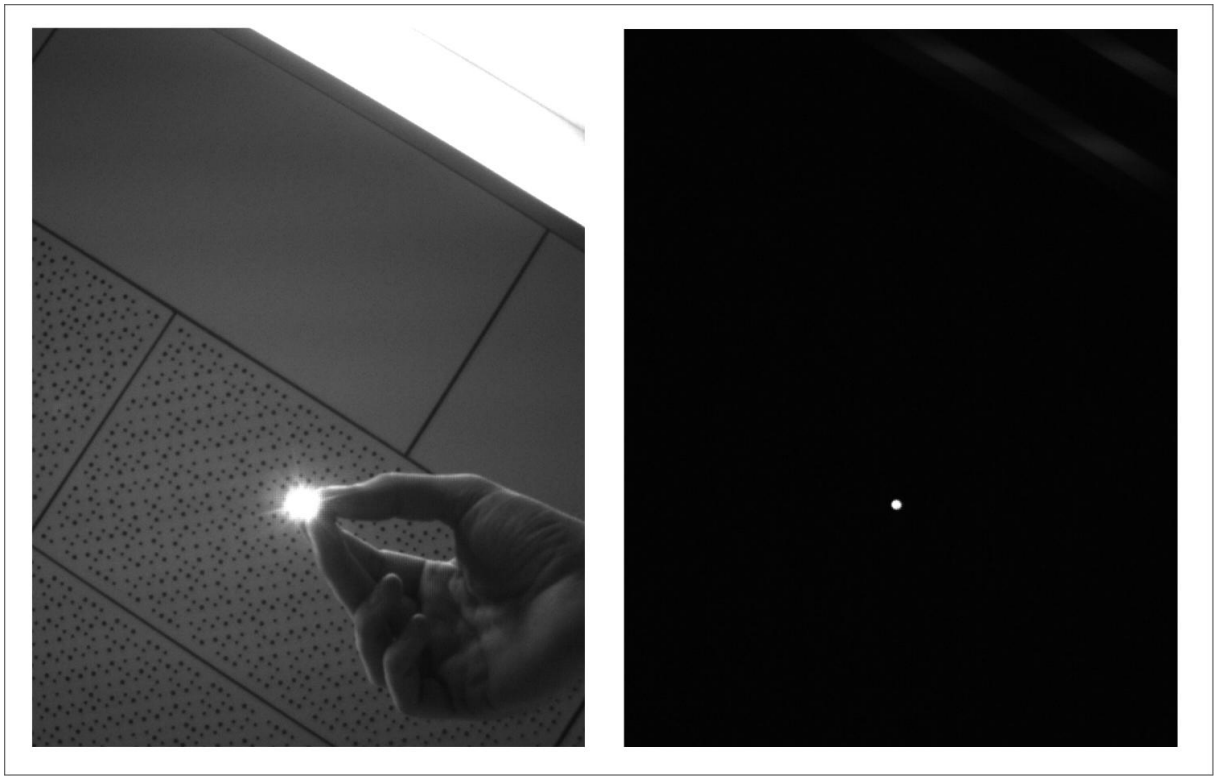

Figure 4.22: Normal versus low-exposure image of LED in office lighting.

4.3.3.2 Lens Calibration

The first step in setting up the practical test of the relative sensor, is calibrating the lens. The key characteristics to determine before using a lens are the boresight and the distortion. The lens non-linearity error is measured by aiming the lens boresight at a black dot on a white surface and then turning the lens incremental angles from the boresight. With an ideal lens the position of the dot on the image sensor will move away from the middle of the image linearly with the angle that the lens is turned from the zero-reference angle. The camera and lens must therefore be placed on a jig that can rotate at an accurate angle. However, with a practical realistic lens some non-linearity always exists. Typically this non-linearity is a function of the angle from the boresight of the lens, with the lens performing more like the ideal case near boresight and having major distortion near the edge of the lens. This distortion can be characterised and can be compensated for when using the lens on a digital camera module by doing post processing.

The amount of distortion is measured and plotted as a function of the angle from boresight. The actual boresight of the lens must be determined before the distortion can be measured. Ideally the boresight should be in the middle of the image plane, but in reality the lens holder is not mounted perfectly in line with the image sensor and the lens is not located perfectly orthogonally with the lens holder. As mentioned, the point of least distortion should be at the lens boresight. This is not necessarily always the case, but for the purpose of this application it is an acceptable assumption. To measure the boresight, a print of perpendicular lines is made and placed orthogonally to the front of the lens and an image is taken thereof. Ideally an image of the orthogonal lines should also contain orthogonal lines. By studying the image, the distortion can, however, be seen and the point of least distortion can be identified and an approximation of the boresight can be made.

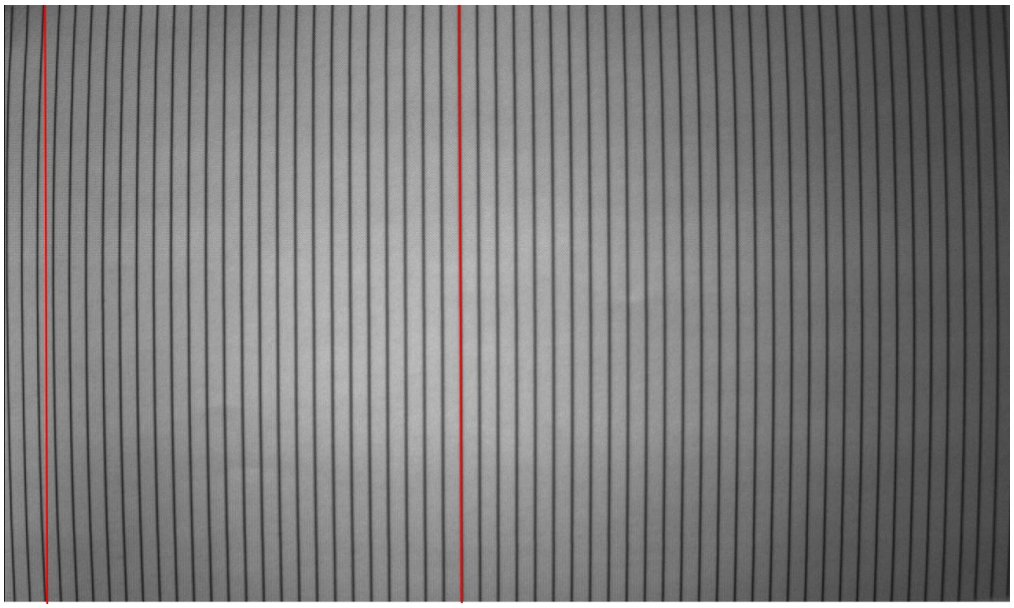

Figure 4.23: Lens distortion.

Figure 4.23 shows the image of the lines. In the left of the image the distortion can be seen by comparing the line on the image with a straight line, and in the middle of the image the point of least distortion can be seen. This is then assumed to be the X-coordinate of the boresight. By counting the individual pixels from the left of the image to the location of least distortion, this X-coordinate is measured as the 580th pixel. This is not perfectly accurate, because of the limited number of lines and the use of judgement to find the straightest line, but once again the application does not require such high accuracy and the measurement is adequate.

Next, the level of distortion is measured as the angle between the actual point and position of the point as seen by the camera.

An illustration and a photo of the setup are shown in Figure 4.24 and Figure 4.25.

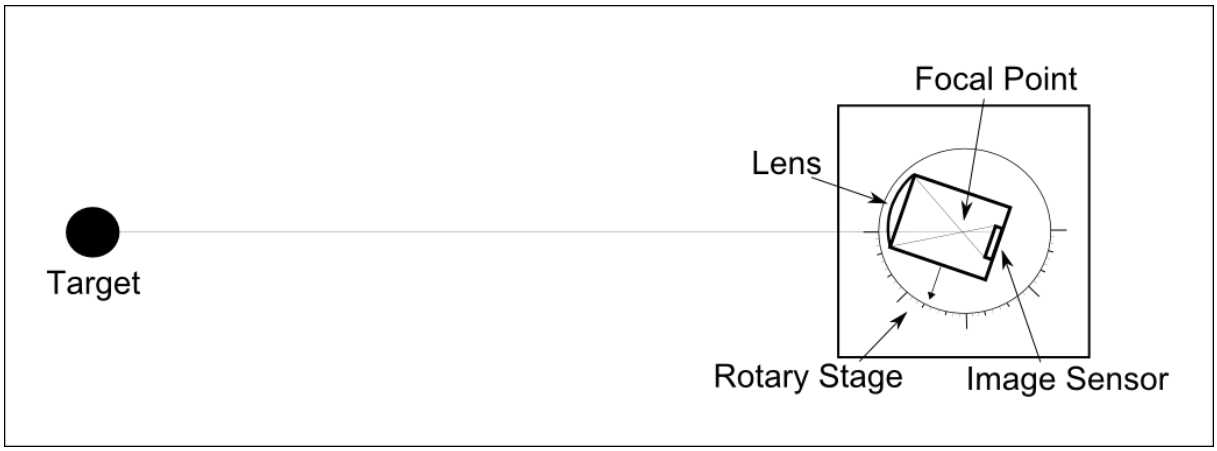

Figure 4.24: Experimental setup for determining camera lens distortion

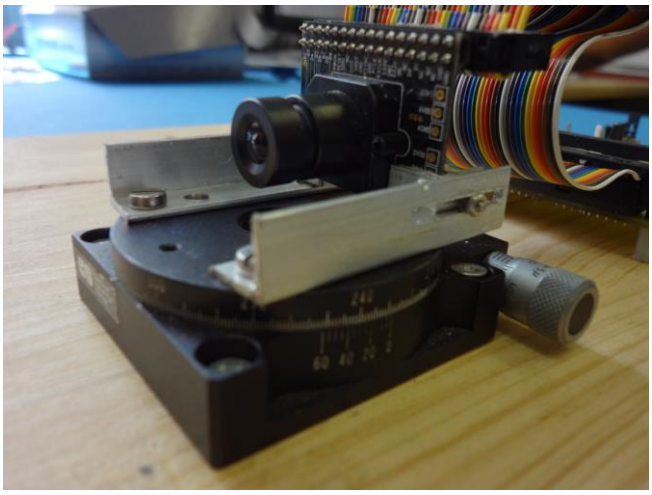

Figure 4.25: Image of the lens distortion tests.

The lens was rotated with increments of 5 degrees and after every rotation a picture was taken, the centroid of the target dot was calculated and the pixel position of it was saved. The data is presented in Figure 4.26.

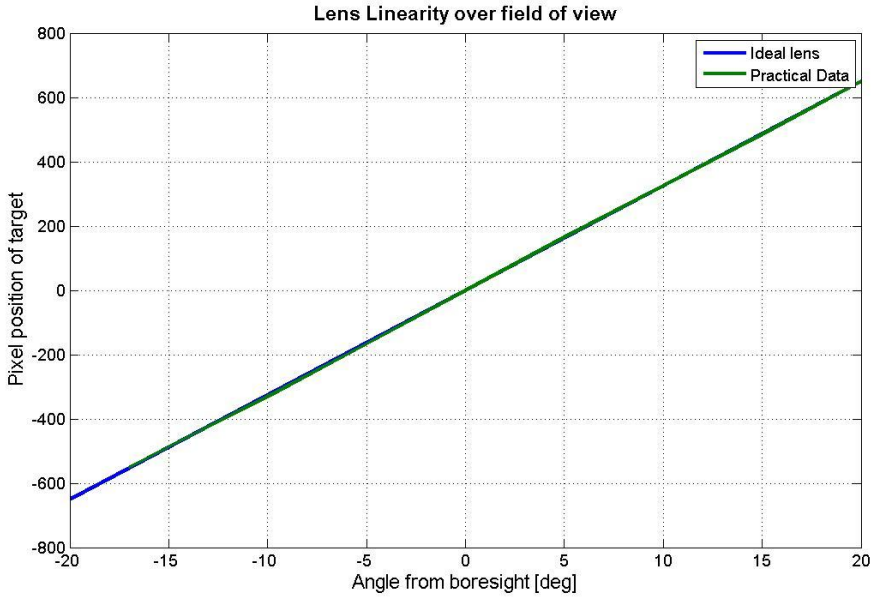

Figure 4.26: Real versus distorted angle measurements.

From Figure 4.26 it is clear that the lens distortion is very low with a maximum measured distortion of 2.5%. For this test a lens made for a $1/3$ inch image sensor was used on a sensor that is only $1/4$ inch in size. The result of doing so is that the light coming from the edges of the lens falls outside of the image sensor and is thus discarded. The downside of doing so is that the field of view of the lens is decreased, thus lowering the maximum angle the sensor will be able to measure. Most of the distortion of an optical lens is at its edges, and this smaller sensor has the advantage of having lower overall distortion over its field of view. The low distortion in the practical tests is due to this.

This small error corresponds to a measurement error of less than a degree. Considering that such high pointing accuracy of the tether is not required, the computational burden of compensating for this error is higher than the benefit that will be gained from it. The choice was therefore made to ignore this error and approximate the lens as an ideal linear lens.

The next step of characterising the lens is determining the actual focal length thereof and correlating this with its specifications. To determine the focal length, the relationship defined in Equation (43) is used. A line with predetermined length is placed at a predetermined distance from the camera and a photo is taken. Its size on the image is determined by counting the amount of pixels it represents and multiplying this with the size of a pixel on the image sensor. With the size on the sensor, the distance to the object and the size of the object known, the focal length can be determined. This was done at two different distances from the camera lens in order to increase accuracy. The focal length of the lens was determined to be exactly 6mm, which is perfectly in line with its specification.

4.3.3.3 Performance

The performance of the tether angle sensor is measured by the speed at which it can acquire new measurements, and by the accuracy of these measurements.

The speed of the sensor is constrained by the speed at which the camera can provide new images, and by the speed the position of the LED can be sent to the MCU. Practical tests of the sensor show that it takes approximately 170ms for an image to be stored on the SRAM from the camera. This time includes detection of the LED which is done in parallel within the FPGA. The region around the position of the LED and its location is sent to MCU within 21ms and the MCU takes approximately 10μs to calculate the centroid of the LED. The total time required for the sensor to produce a new measurement is therefore limited largely by the speed at which the camera operates. Taking into account all the steps in acquiring new sensor data, the sensor is able to produce measurements in less than 200ms.

The accuracy of the sensor is determined mainly by the distortion in the lens. As discussed in Section 4.3.3.2 the maximum distortion from the lens is 2.5% near the edge of the AOV. The lens has a focal length of 6mm and thus an AOV of about 30º. The maximum measurement error from the sensor is thus about 0.8 º at the edge of the AOV.

4.3.4 Deployer Testing

The control of the motor with the mass being subjected to 1g gravity proved difficult when the more complicated EKF algorithm was implemented to do estimation. This is attributed to the fact that tests could only be done over short distances because of practical limitations. This meant that control had to be more aggressive and therefore required smaller settling times. With the stricter requirements on the controller, the system is naturally less stable. This trade-off between performance and stability is a common theme in control theory.

The main uncertainty in the system, that increased the difficulty of accurately modelling the system, is the friction force in the reel and the electric motor. Usually the friction forces in BLDC-motors scale with the size of their magnets as well as their power. With a motor large enough to overcome the large forces present in a 1g environment, the friction is similarly large.

The problem with the motor was that the friction at speeds near zero was large and also varied dramatically with speed. This un-modelled behaviour of the system caused large deviations from the model, which assumes a constant static friction (stiction) force and a constant dynamic friction force.

A further problem that was caused by the aggressive controller was that the discrete nature of the Hall sensor output had a much larger effect when control was done at faster sample times. The fast sample times required to control the system at this fast rate, combined with the slow velocity of the deployment, meant that there were only singular steps in the Hall sensor output in-between samples. This caused a much discretised velocity reading. The Hall sensor output for a full rotation of the deployment spool is shown in Figure 4.27

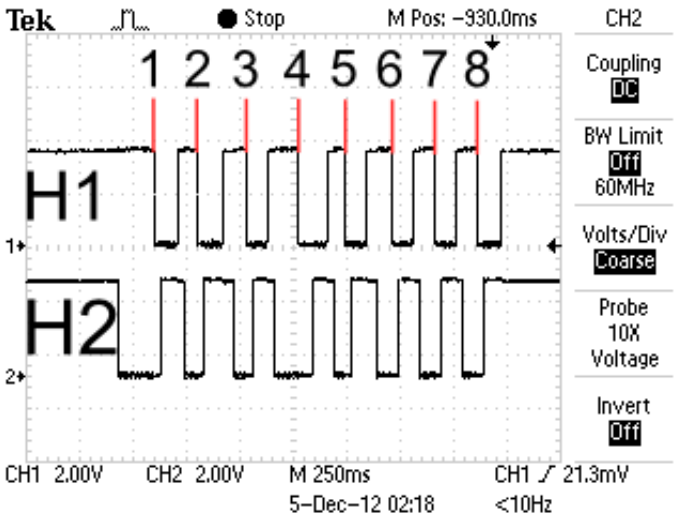

Figure 4.27: Hall sensor outputs for one rotation.

This shows that the hall sensor provides a resolution of eight pulses per revolution. This number can be increased by applying an XOR-gate on these two inputs. By doing information regarding the direction of the rotation of the system is lost. For the system to be able to do distance control, the rotation direction is necessary. The maximum resolution possible is therefore eight pulses per revolution. With a reel radius of 20mm, the discretisation interval of the Hall sensor encoder is then

$$\Delta s = \frac{2\pi R_{reel}}{\eta_{sensor}} = 15.7mm$$

The discretised Hall sensor output and the un-modelled friction in the system causes instability in an EKF which has sufficient time related performance to do the estimation of such an aggressive system. Due to time constraints, the EKF implementation on the ground had to be abandoned and only PI control was done. The EKF was, however, implemented in Embedded C code and practically tested with the microcontroller and performed as expected for situations where a constant deployment distance was kept. The EKF implementation is shown in Appendix A.4.

The alternative control method, as also implemented for the simulation environment, was the use of a PI controller. The integrator of the PI system helped to compensate for uncertainties in the model of the friction force, and ensured a zero steady state error. The system was run with a speed reference command of $0.1m.s^{-1}$ and the step response is shown below.

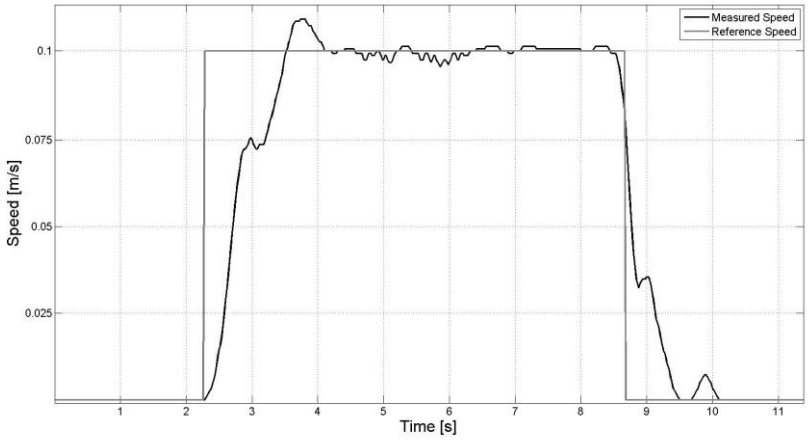

Figure 4.28: Deployment velocity step using PI controller.

For purposes of developing the system further and improving on the control performance, the EKF model needs to be expanded to include the friction in deployment spool and electric motor for varying speeds.

4.3.5 EKF Testing

To be able to accurately simulate the system, the time the OBC takes to execute the EKF algorithm must be determined. Even though the EKF is not used in the control of the prototype deployer system, the mathematical calculations needed to execute the EKF were still implemented in Embedded code and the performance of the OBC was tested.

The EKF requires a series of matrix multiplications and inversions in every step of the EKF which is computationally intensive. Implementing these multiplications is also not easily done since there are no standard built in C-libraries which contain functions for doing these calculations. Algorithms written by [26] were used and adapted to function in the Embedded C environment. The EKF algorithm was then implemented using these matrix functions and executed on the MCU built into the prototype electronics. The MCU was able to complete an

iteration of the algorithm in a maximum time of 7ms. These results are used to determine a realistic sample time for the orbital simulation which is run in Section 5.1.

The performance of the EKF in terms of estimating the angles and deployment distances is discussed in Section 5.2.1.

5 Orbital Simulation

5.1 Simulation Structure

Simulation of the system was done in MATLAB Simulink. Both MATLAB embedded code and C code were used for programming the simulation.

The simulation is a combination of an Orbital ADCS simulation originally done by Prof. W.H. Steyn [26], system dynamics discussed in Section 3.3, and control algorithms discussed in Section 3.4.3. The simulation is divided into separate sections representing the physical tether system, namely the main satellite and the payload satellite.

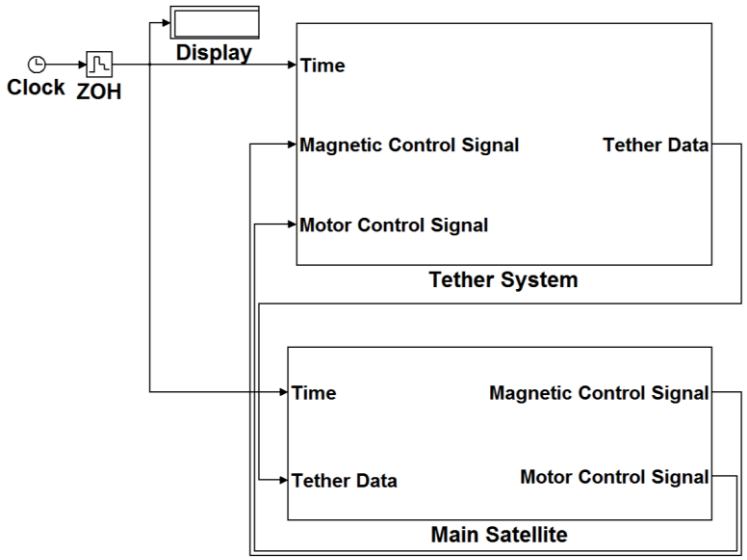

Each simulation block is further divided into modelling blocks and practical blocks. The modelling blocks serves as dynamic simulation model of the satellite or system. This is a

mathematical model of the physics underlying the motion of the satellite. The practical blocks are the blocks simulating functions executed by the satellites themselves. This includes measurements done by sensors, calculations done by OBCs and control done by actuators. In accordance with this partitioning, the tether system simulation block contains only dynamics blocks. Control signals for controlling the liberation angles of the tether and sensing of the liberation angles and tether deployment length are in reality done by the main satellite, and these signals are fed to and from the main satellite. The main satellite then contains practical blocks for its own ADCS as well as for the tether control. The architecture of the simulation and this interfacing between the subsystems are illustrated in Figure 5.1.

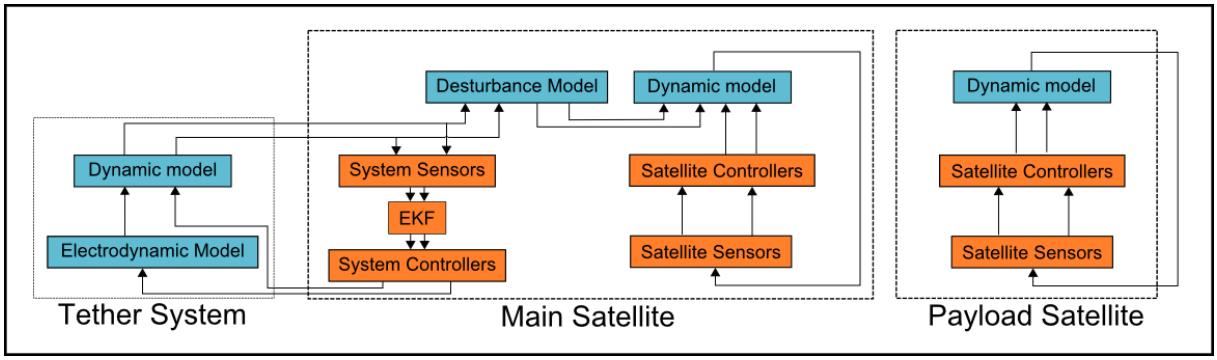

Figure 5.1: Simulation layout.

A key aspect to note here is that the dynamics of the tether is decoupled from the satellite attitude dynamics. The tether system assumes two end masses with tether connection at their COMs. The rotation of the satellite bodies thus has no influence on the tether tension. The effect of the tether tension is, however, included in the satellite ADCS simulation by including the tension in the tether, and the moment on the satellites that results from this tension force as a disturbance moment on the satellite bodies.

The calculation if the orbital parameters, such as the gravitational model, the geomagnetic model and the orbit propagation, is done by the ADCS_Models block [26].

5.1.1 Tether System

The simulation of the tether consists of the models derived in Section 3.3.5 and 3.3.6. The system is divided into the electrodynamic model, the tether model, and the ADCS_Models block which is discussed in the previous section.

The Tether Model block is an adaptation of a simulation block done by Prof. W.H. Steyn [26]. The normal satellite model is replaced with a model of the tether system as discussed in Section 3.3.5. To accommodate the dynamics in Euler angles, some transformations to the normal Euler angles had to be made to form the DCM needed for the orbital simulation which uses quaternions to propagate the rotations of the satellites. The electromagnetic simulations in the Electrodynamic block are based on the equations in Section 3.3.6.2.

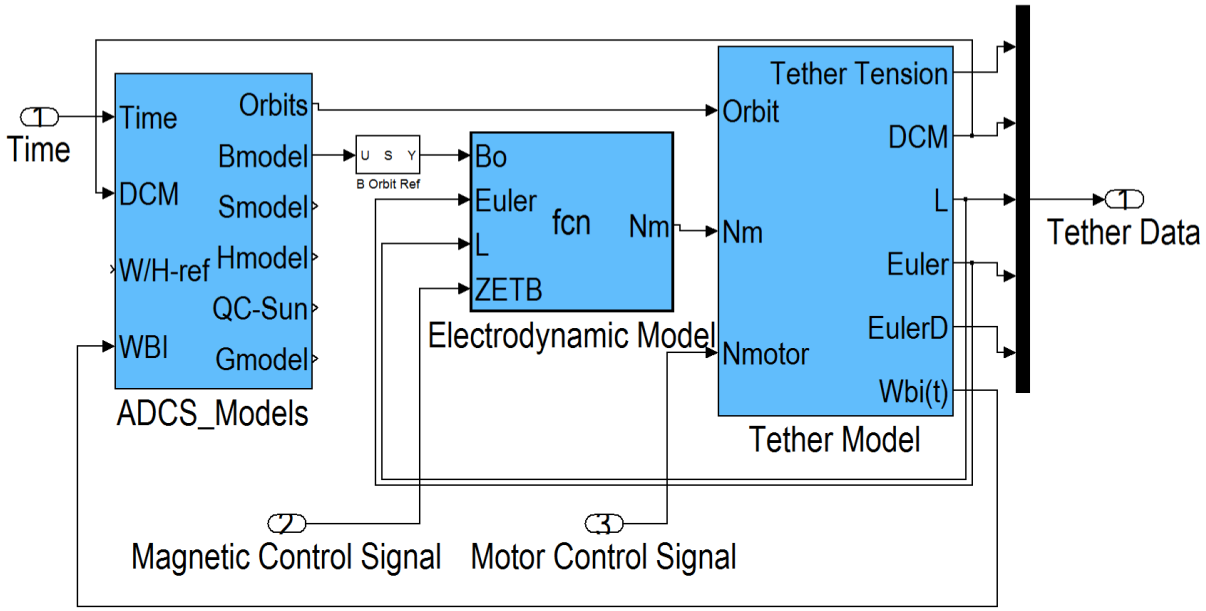

Figure 5.2: Simulink simulation of tether.

This part of the simulation is purely an application of the mathematical models describing the dynamics of the tether. The calculation of control signals and execution of estimation algorithms are done by the main satellite.

5.1.2 Main Satellite

The simulation of the main satellite includes the dynamics and ADCS-models block from the simulation done by Prof. W.H. Steyn [26]. These two blocks together simulate a CubeSat in orbit using quaternions to propagate the orientation of the satellite. The dynamics block accepts control torques from reaction wheel and magnetic-torquer controllers also designed by Prof. W.H. Steyn [26]. The reaction wheel and magnetic controllers offers a variety of control modes. Both of these controllers are set to function in earth pointing mode, and the details of the controllers are not discussed further in this study. The specifications for the reaction wheel controller are set for control magnitudes suitable for a Nano-satellite mission. The magnitudes of the control moments the magnetic controller can produce are also set to specifications corresponding to Nano-satellite torquer-rods.

The dynamics of the main satellite's orientation is then controlled by these predesigned controllers. The only adjustment made to this system, is to include a disturbance torque which originates from the forces the tether exerts on the satellite body. These forces are discussed in Section 3.3.7. The disturbance torques are calculated by using the DCM, and tether tension of the tether simulation, which is fed to the main satellite.

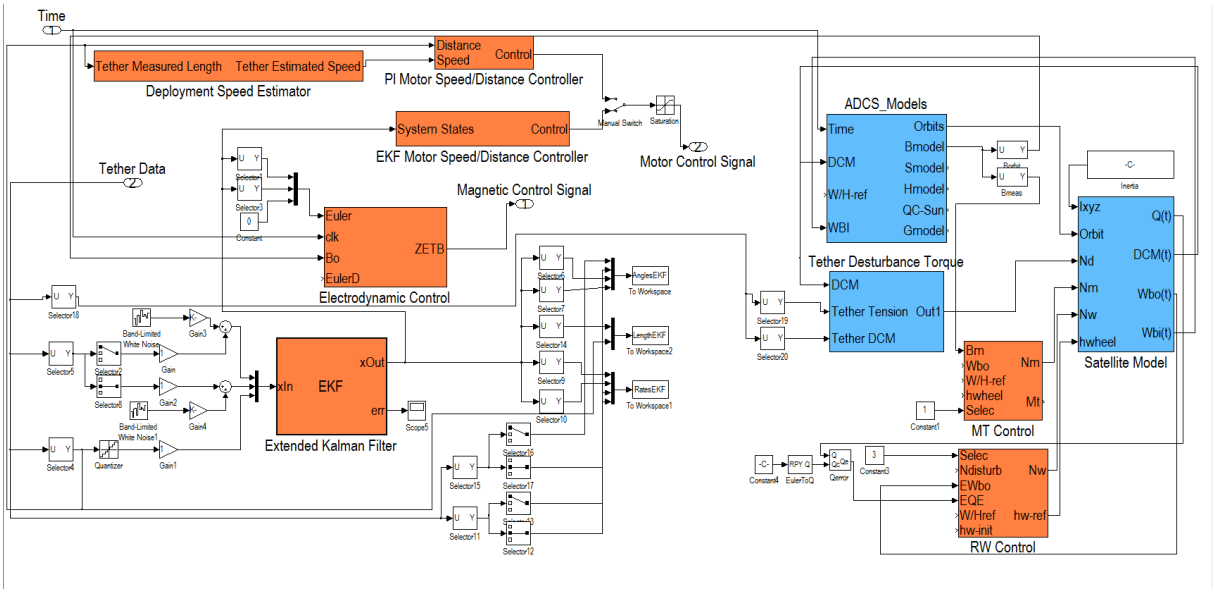

Figure 5.3: Simulink simulation of main satellite

The main satellite further executes the EKF and control algorithms for controlling the tether. These control signals are fed back to the tether simulation. In Section 4 sensors were designed and their performance was tested. These then provide us with realistic estimates of the accuracy and speed of measurements which would be possible in space. These results were incorporated in the simulation to accurately model the system as it would react in space. The main satellite simulation incorporates all this information about the sensors and the EKF performance, to provide realistic control signals for controlling the tether.

Direct feedback of the system states was not used to calculate control signals. A a Quantisation Simulink block was used to simulate the quantised nature of the Hall-sensor and the Tether Angle-sensor measurements, which are discussed in Section 3.4.1. Because there are no sensors for determining the rates of the system, it was estimated by the EKF. The performance of the physical system is used where angle measurements are only available every 200ms and the EKF algorithm is only run every 30ms, as discussed in Section 4 .

5.2 Simulations

5.2.1 Extended Kalman Filter

The performance of the EKF was tested by adding noise to the angle and distance variables fed to the filter. The size of the noise added was scaled to correspond to the practical results obtained in Section 4. Below is a summary of the noise added to the individual system states:

- Angle measurements: In accordance with the accuracy of the camera sensor tested in Section 4.3.3.2, a measurement error of up to 0.7 degrees was added. In accordance with Section 4.3.3.3, new measurements were only made available every 200ms.
- Deployment length measurements: As discussed in Section 4.3.4, the Hall sensor has 8 poles. Considering that the maximum radius of the deployment reel is 20mm, a

maximum quantisation interval of 16mm was added to the deployment distance in the simulation.

Figure 5.4 shows the EKF estimates of- and the measured system states with the added noise.

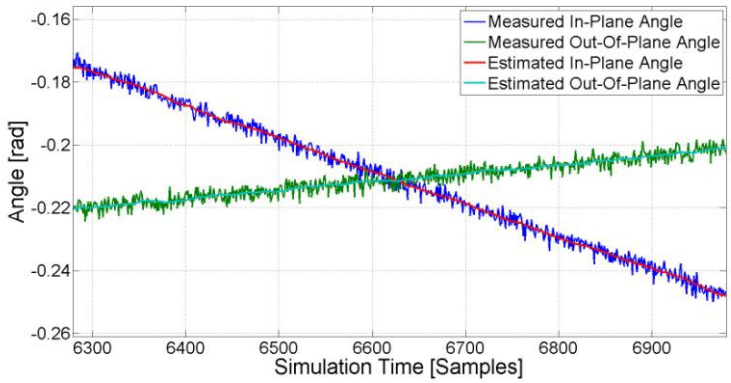

Figure 5.4: Estimated states of noisy measurements

From Figure 5.4 it can be seen how the EKF filters the noise present on the measured data by using the system model.

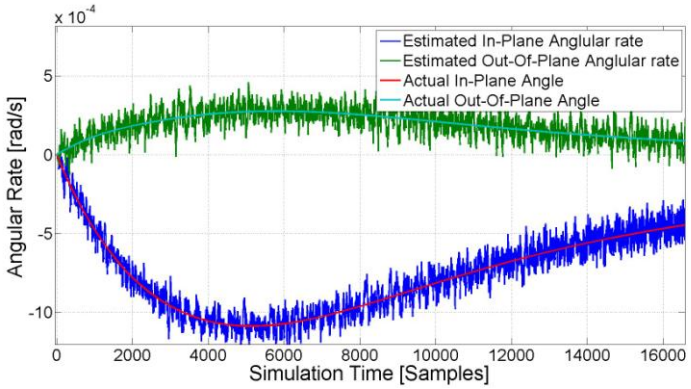

Figure 5.5: Estimated angular rates from noisy angle measurements ($\sigma^2 = 0.01$)

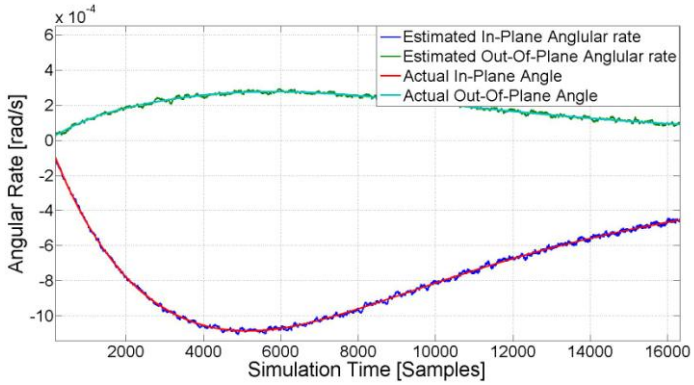

Figure 5.6 Estimated angular rates from noisy angle measurements ($\sigma^2 = 0.0001$)

Figure 5.5 and Figure 5.6 show how the noise added to the measurements affects the estimation of the angular rates. The EKF provides stable estimations of these angular rates. In Figure 5.6 the covariance matrix entries for the in-and out-of-plane angles were changed from $\sigma^2 = 0.01$ to $\sigma^2 = 0.0001$. By comparing these two figures the effect of changing the covariance matrix of the EKF can be seen. By lowering the covariance of the process noise

matrix, the EKF is set to trust the model of the system rather than new measurements. This makes the system less susceptible to measurement noise. By doing so, the consequences of errors in the model of the system become larger and un-modelled behaviour in space may cause larger deviations from the true states. An effective way of raising the reliability and stability of the EKF is to combine the algorithm with other estimation techniques and so to improve the robustness of the algorithm.

5.2.2 Deployment

Two approaches were taken for the deployer control. The first is a passive deployment using friction to slow down the deployment to a point where the tether is considered being fully deployed and a second approach where active control is implemented using an electric motor and hall sensors to constantly monitor and control the speed and deployed distance of the tether.

5.2.2.1 Passive Deployment

Passive deployment can be done using only the friction in the reel as restrictive force controlling the tether deployment. The system was simulated with a starting tether deployment speed of 0.1m/s and different friction forces for the reel and results are shown in Figure 5.7.

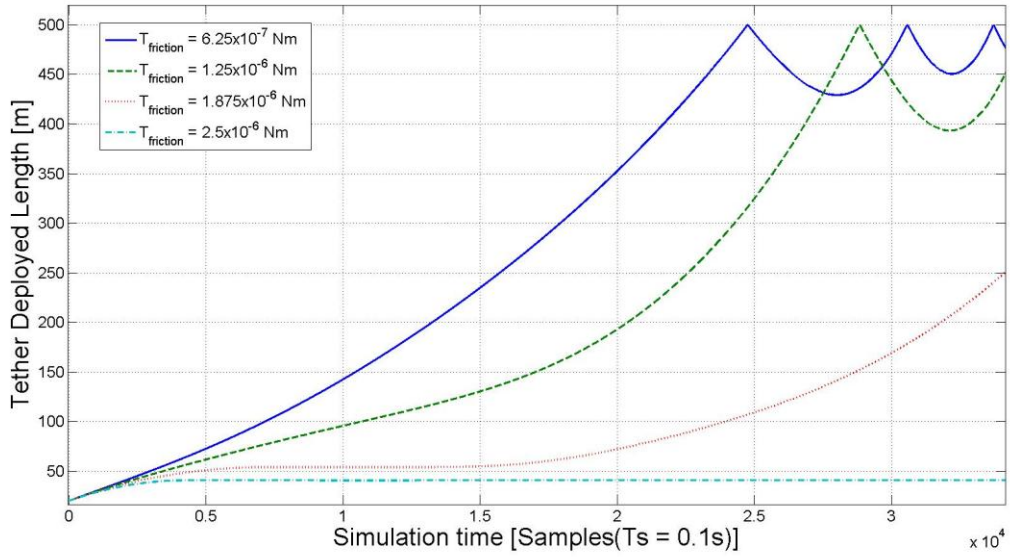

Figure 5.7: Simulated passive deployment scenarios.

From this figure it is clear that with a passive scheme such as this, the deployment will either stop at some distance or reach a point where the gravity gradient force becomes larger than the friction force in the reel and the deployment starts accelerating. In the case where the deployment distance passes the point where friction can stop the deployment, the system will accelerate until the tether is fully unwound. When this occurs, the satellites bounce back towards each other. Gravity gradient then pulls the system apart until it once again bounces back.

During simulation it was discovered that while deploying the tether, the system gained a leading in-plane angle, even though the bodies were launched from each other in the Nadir direction. As discussed in Section 3.1.1, the tether provides a restrictive force to keep the satellites moving in unison. This is true when the tether force is large enough to keep the satellites apart at a fixed distance. However, when the tether force is lower, and the bodies move apart in the Nadir direction, the bodies' radius of rotation changes and the law of conservation of angular momentum then require the orbital rate to change with it. The top satellite gains altitude, and thus loses orbital rate, and the bottom satellite loses altitude and gains orbital rate. The result of this is the lower satellite leading the top one. The simulation in Figure 5.8 illustrates this. The satellites are launched from each other in the Nadir direction with an initial velocity of 0.1m/s.

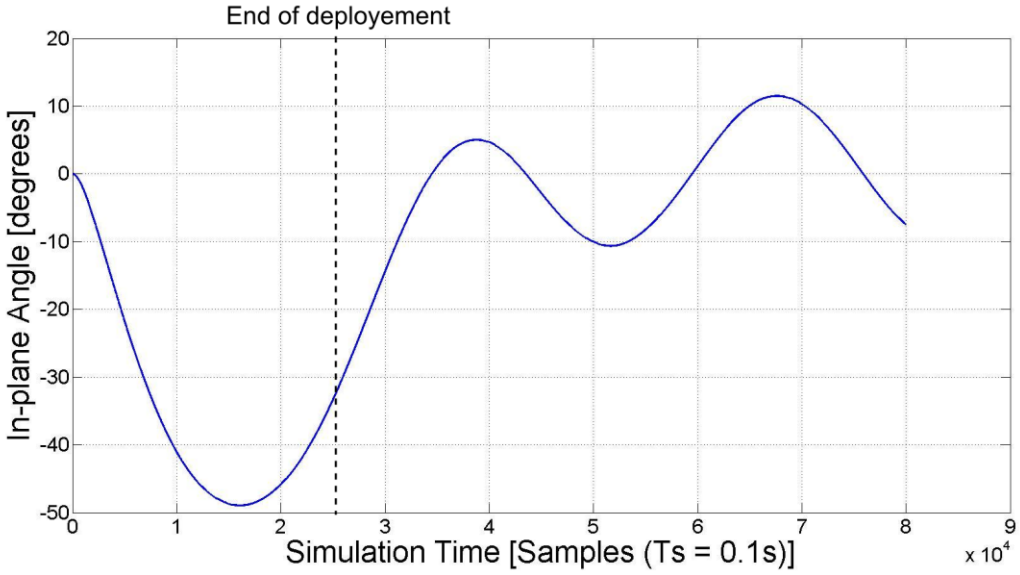

Figure 5.8: Residual in-plane angle after deployment.

When the deployment is stopped and the satellites are slowed down to a fixed tether distance, the tether force increases to the point where the two bodies are in the mode where the system is constrained to the length of the tether and gravity-gradient starts pulling the satellites back to the Nadir direction. During deployment the system will therefore always gain some in-plane offset, which will result in oscillation when the deployment is stopped and the tether tension is increased. The ideal will be to use the electromagnetic force to continuously force the tether back to Nadir during deployment. The electromagnetic force is typically small in comparison with the force causing this oscillation and the only option is to damp the oscillations electromagnetically after deployment. The size of the resulting oscillation is, however, a function of the deployment speed, as demonstrated later, and can be kept to a minimum by doing the deployment at low speed.

Another point to note here is that when the tether tension increases, the system starts swinging back towards Nadir, causing centrifugal forces to pull the satellite bodies apart. This effect can be seen in Figure 5.7 where the friction force is 1.25×10^{-6} Nm (Green line) and 1.875×10^{-6}Nm (Red line). In both these simulations, the deployment is slowed down by

the tether friction and then accelerated again when the tether starts swinging back. In the case where the friction was 1.875×10^{-6} Nm (Red line), the deployment was actually nearly brought to a halt when the centrifugal force started pulling the system apart again and then increased the deployed distance to the point where the gravity gradient force was large enough to overpower the friction force and so causing the system to fully deploy.

The situation where the tether stops at some distance is the type of deployment required of a tether system. As mentioned, the tether will only stop if the friction force is large enough to overcome the gravity gradient tension. This point where the two forces are equal is reached at less than 50m for a friction torque of 6.25×10^{-7}Nm. A deployment distance of 500m is required and the friction torque thus has to be much larger. As demonstrated in Figure 5.8, a larger friction also results in the tether braking quicker and stopping earlier. The only way to achieve a larger deployment distance is then to increase the friction and simultaneously increase the launch speed at which the two bodies are initially deployed from each other. For a friction force slightly larger than the gravity gradient force at 500m, the system is simulated at different launch speeds.

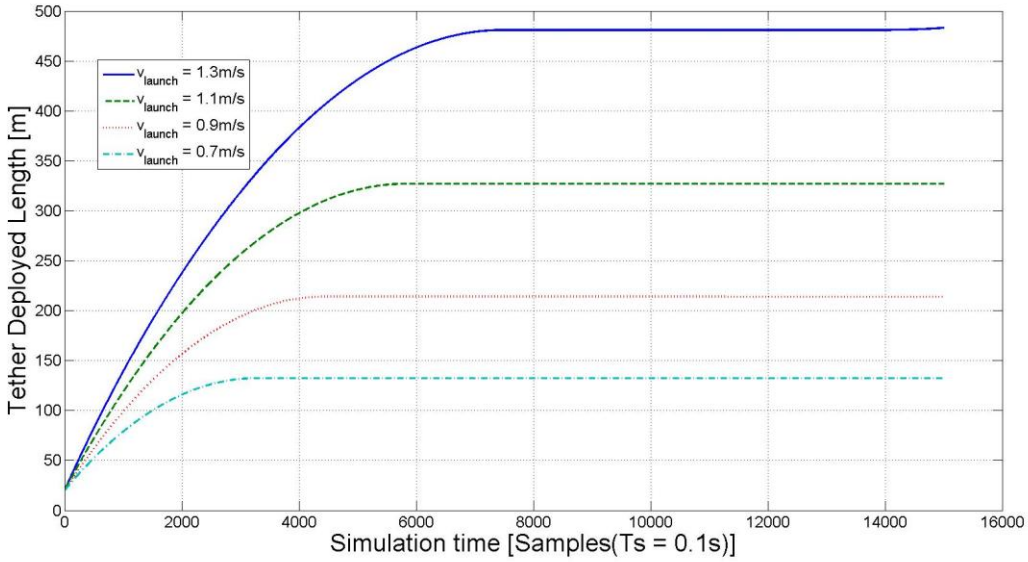

Figure 5.9: Stable passive deployment for varying launch speeds (fixed 18×10^{-6} Nm friction torque).

Figure 5.9 shows that it is possible to do a passive deployment to 500m, but that a launch speed of 1.3m/s is required to achieve this. This requires a very large impulse given to the deployed satellites and is deemed unpractical. There are multiple risks with this deployment method. Because such a large force is needed to propel the satellites apart, a misalignment in the deployment system will cause large moments and rotations on the satellite bodies, which will likely result in instability and critical failure of the deployment. If the deployment should encounter an unforeseen force within the deployment reel, causing the satellite to lose momentum, the deployment may fall short of its intended deployment distance. Similarly if the friction in the reel is smaller in space than anticipated, the deployment may go too far and the tether might become taut, causing the deployed satellite to bounce back towards the main satellite or even causes the tether to break.

This serves as motivation to abandon the lighter and simpler passive deployment system for a more complex but safer active deployment controller.

5.2.2.2 Active Deployment

For active deployment an electric motor can be used to control the speed of the tether as it deploys. To do this a proportional speed controller is implemented which takes the measured deployment speed as input, and gives a motor torque as output. When the tether approaches its final length, the deployment speed must be gradually decreased to bring the tether to a standstill. To do this, a proportional distance controller is implemented, taking the distance as input and giving a desired speed as output. This output speed is then fed as reference input to the speed controller. Both of these controllers are over-damped to keep the deployment process smooth and eliminate any overshoot. The system is simulated with a launch speed of 0.1m/s, reference tether deploy speed of 0.1m/s and reference deployment distance of 480m. The results are shown in Figure 5.10.

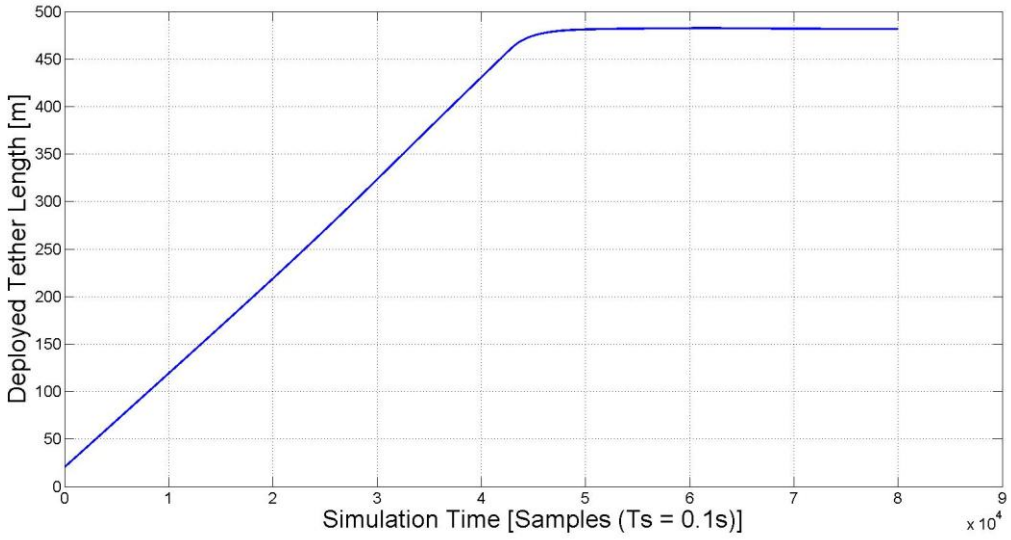

Figure 5.10: Simulated active deployment.

Figure 5.11 shown how the in-plane angle oscillation, varies with deployment speed.

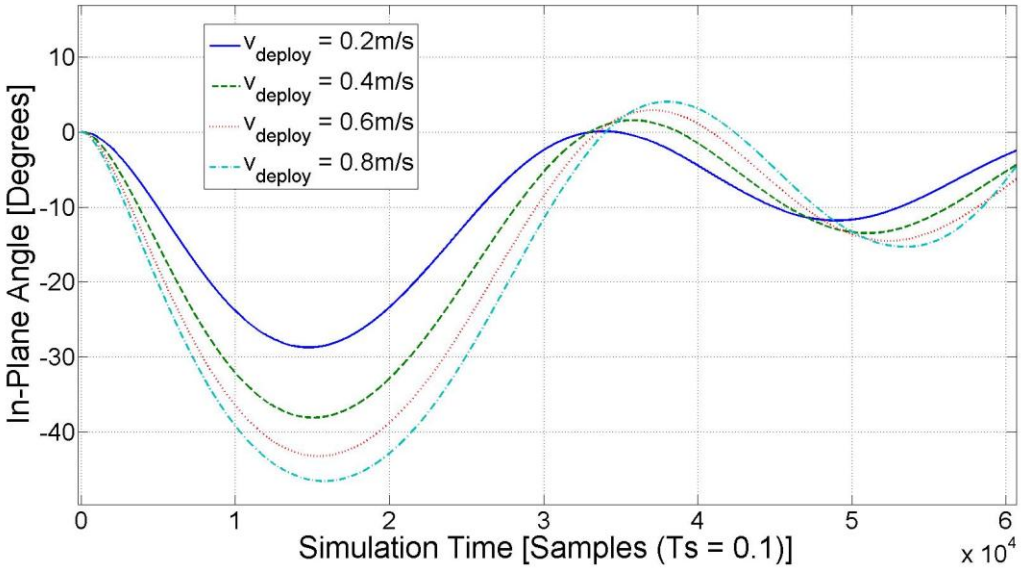

Figure 5.11: Residual in-plane angle for different deployment speeds.

As discussed in Section 3.4.3.2, two speed controllers were implemented; the first uses only the Hall sensor measurements of the deployment distance to do proportional control of the deployment speed, and the second controller uses an EKF to do full state feedback control of the non-linear system. These two controllers were both simulated and the results are shown in Figure 5.12.

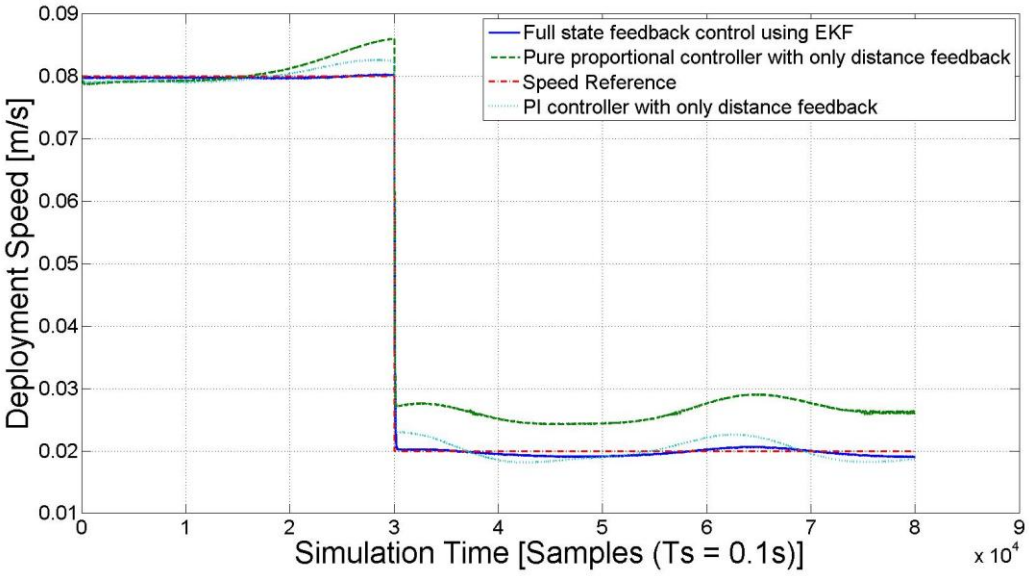

Figure 5.12: Deployment speed step response for different controllers.

From Figure 5.12 it can be seen that the proportional controller does perform worse than the full state feedback controller. As the tether is deployed and the gravity gradient force becomes larger, the simpler controller suffers from a steady state error. The performance can be improved by adding an integrator, but with the downside of having extra overshoot. The area

where its performance suffers most, is when the tether liberation angles and rotation rates become larger and forces such as centrifugal forces become significant. When this happens, the controller has significantly more oscillation than the state feedback controller. To decrease the overshoot of the PI controller, the gains can be lowered, but the centrifugal forces then cause larger oscillations and in some cases instability.

By using the EKF designed in Section 3.4.3.2, combined with the sensor measurements which the designed and built sensors would provide, the deployment of the system could be done to high accuracy by using an electric motor to control the tension on the tether.

5.2.3 Tether Angle

The simulation of the orientation of the tether system is done using the equations of motion derived earlier. The control of the system orientation is simulated, implementing two different control strategies for using the electrodynamic force on the tether to stabilise the system.

The weighted controller described in Section 3.4.3.1 was implemented to demonstrate the control of the tether liberation angles using electrodynamic control. The equations describing the electrodynamic moments on the system which is shown in Section 3.3.6.2 were used to calculate the moment on the system for a given input impedance placed between the tether and the contactor impedance. Simulations of the electrodynamic stabilisation of the tether were done for different controller weights and are demonstrated in Figure 5.13 to Figure 5.15. All these simulations started with the in- and out-of-plane angles at 5º and tether length fixed at 480m. The variables W_θ and $W_\emptyset$ are used to denote the control weights for the in- and out-of-plane angles respectively.

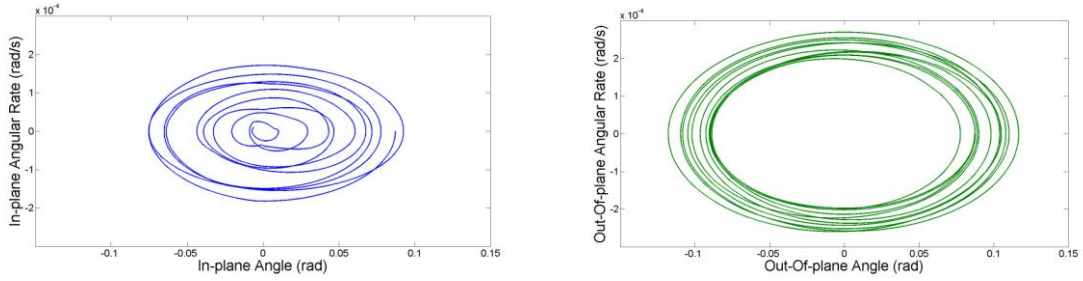

Figure 5.13: Tether in- and out-of-plane angles ($W_\theta = 4W_\emptyset$).

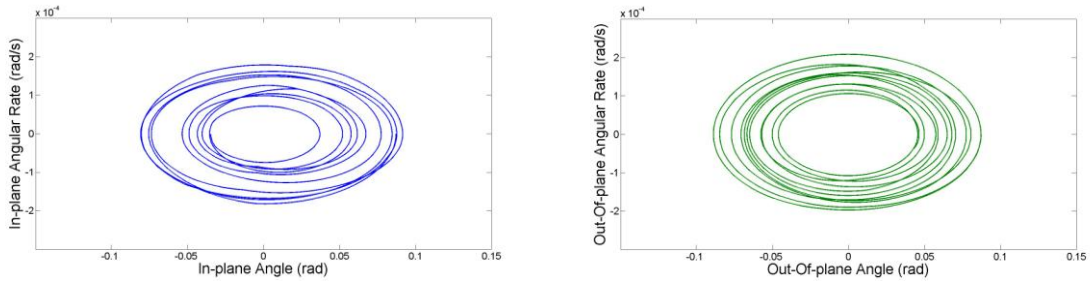

Figure 5.14: Tether in- and out-of-plane angles ($W_\theta = W_\emptyset$).

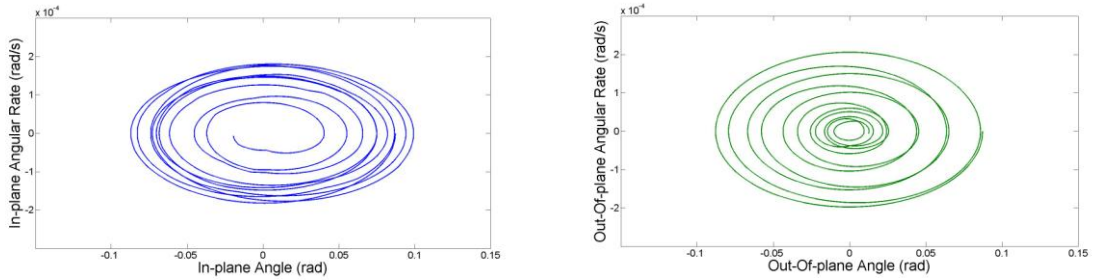

Figure 5.15: Tether in- and out-of-plane angles ($4W_\theta = W_\emptyset$).

Figure 5.13 to Figure 5.15 illustrate how the in- and out-of-plane angle can both be controlled at the same time. In all 3 these figures both angles are stable with control weight determining which angle enjoys most of the control effort, and is therefore controlled to a higher accuracy. With enough time, both angles in all of these figures will eventually control to an angle and speed close to zero. This controller takes only into account the direction of the B-field, the direction and motion of the tether, and the control weights. The complex physics involved in the current collection process only scales the size of the control current. This in turn only effects how aggressively these angles are controlled, but not the stability of the system and control law combination.

5.2.4 Main Satellite Body Rotations

The main satellite contains a full ADCS which utilises a three axis reaction wheel controller, as discussed in Section 3.2.1. As part of the tether angle measurement strategy, the main satellite needs to utilise its ADCS to keep its orientation Nadir. To do this, a controller outside of the scope of this study, is used to do full three-axis stabilisation. In the simulation, the tension in the tether and the relative orientation of the main satellite and the tether is fed to the main satellite where the disturbance toque on the main satellite is calculated as described in Section 3.3.7.

To demonstrate the disturbance torques the tether would exert on the main satellite, a simulation was done with the tether deployed to 480m, and the in-and out-of-plane angles both having oscillations with magnitude of 40º peak-to-peak. Figure 5.16 shows the tether disturbance force on the main satellite. The Nano-reaction wheels that are used for this control system has maximum torque-capacity of 0.35mNm. From this figure it is clear that the magnitude of the disturbance torque that should be present on the system, is well within the specifications of the reaction wheels.

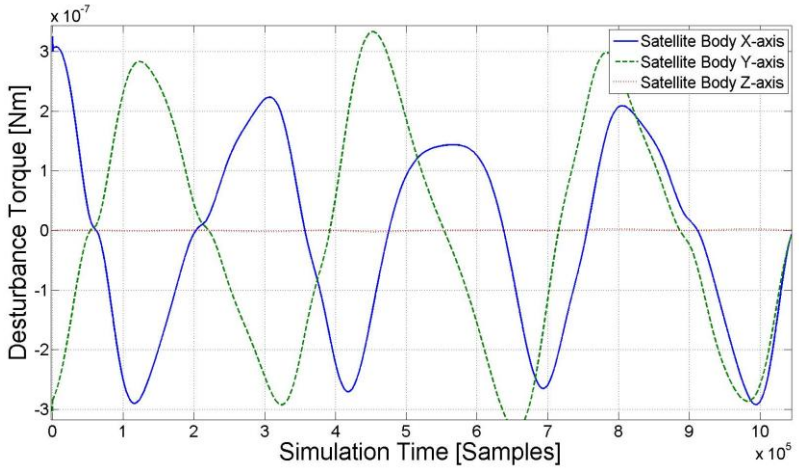

Figure 5.16:Tether disturbance torque on main satellite.

The main satellite utilises the reaction wheel controller to keep the main satellite pointing Nadir to less than 1º accuracy. This is illustrated in Figure 5.17.

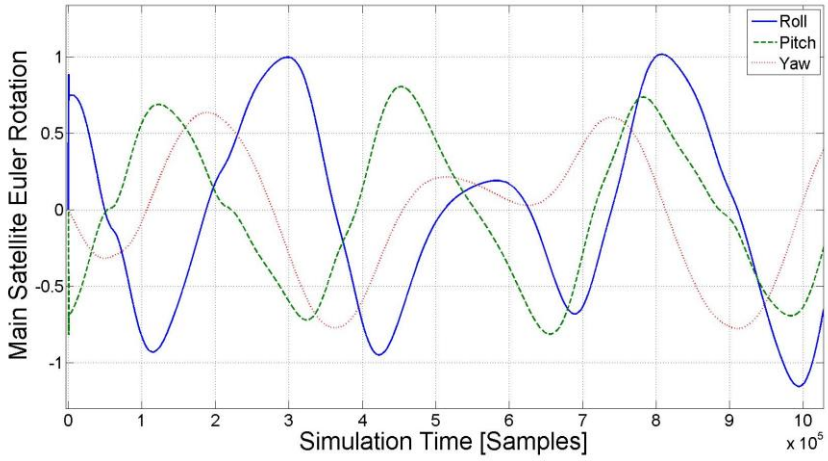

Figure 5.17: Main satellite Euler rotations.

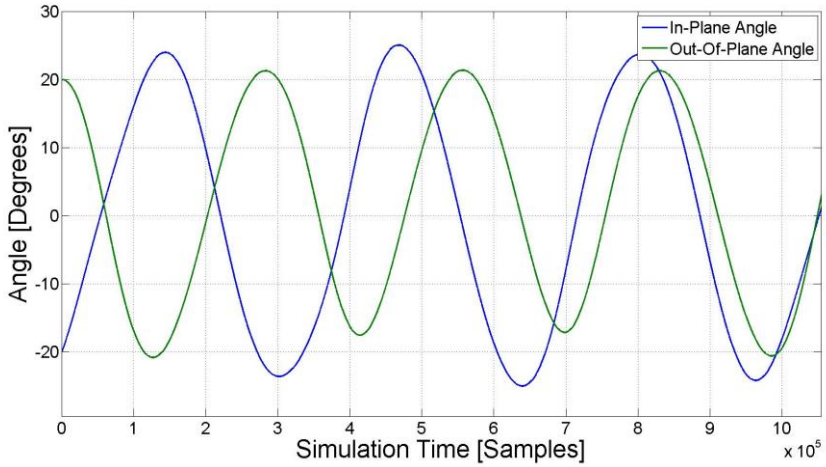

Figure 5.18: Tether liberation angles.

6 Conclusions & Recommendations

6.1 Conclusions

6.1.1 General Concept

In general all systems on a satellite, especially on a small satellite, must be kept as simple as possible. This decreases the risk of failure due to design error and generally reduces the number of subsystems in which a problem may arise.

With this goal of simplicity in mind, basic, general goals were set for the electrodynamic performance of the system. During this study the complexities and uncertainties surrounding the electron collection along the tether were highlighted. This uncertainty made the design of high accuracy controllers unnecessary. The conclusion was made that the focus should be on the overall stability of the system, rather than on high accuracy control. The low success rate of past missions also hints at the importance of focussing on designing a system that achieves the basic goal of stable deployment, rather than advanced manoeuvres.

The idea of a passive deployment strategy was also motivated by the goal of simplifying the design. However, after the dynamics of the system were studied, it became apparent that a simple, passive deployment strategy would not provide a safe, reliable deployment to a preferred deployment distance. With the complexity of the dynamics of the tethered system in mind, an active deployment strategy offers better reliability and control. In this case the more complex deployment system offers enough advantages over the simpler system to justify using it.

An analysis of the dynamics of the system suggests that a vertically-gravity-gradient-stabilised tether offers good stability. The variables to describe the orientation of such a system are also measurable by using the two sensors designed. These sensors are small, low power, and lightweight enough to fit the requirements of a CubeSat system. The study also proves that the electrodynamic force created by the tether can be used to damp oscillations in

the tether angle and drive the system towards the Nadir direction. With a 500m copper wire tether, the aerodynamic forces were found to have an insignificant effect on the orientation of the tether and these forces were left out of the controller design.

Verifying the mechanical and theoretical designs in this study on earth proved complex. It proved difficult to remove the effects of the large gravitational force present on earth from the deployment mechanism. Further, tests could only be done over short distance because of spatial limitations. The theoretical principles governing the performance of the designed sensors and actuators suggest that both the deployment mechanism and the tether angle sensor should provide the measurements and control needed to control the tether in space. Theoretical analysis of the camera and LED used in the tether angle sensor suggests that the sensor will be able to operate in the presence of stars. Simulations of the deployment mechanism suggest that the deployment speed and distance can be controlled to high accuracy using only an electric motor controlling the tether tension.

6.1.2 Tether Deployment and Angle Control

The two possibilities for deploying the tether were investigated namely, active and passive deployment. Simulations were done which indicated that passive deployment would require friction torques of up to 18×10^{-6}Nm to overcome the gravity gradient force present at 500m. To achieve deployment of 500m, unreasonably large separation speeds of 1.3m/s are required. Two methods of separating the satellites were discussed and a spring loaded system was found to be the best solution. If a spring loaded system were to be used for the separation mechanism, this large separation speed required for passive deployment would be difficult to achieve. One of the major causes of failure for tethered missions was found to be the issue of the tether becoming stuck within the deployment spool during deployment. The effect of such an event can be minimised by increasing the separation speed and by doing so, increasing the linear momentum of the two satellites moving apart. The aim should thus be to maximise the separation speed.

The alternative method of actively controlling the deployment of the tether using an electric motor was analysed next. Using the tether angle sensor developed in this study, in conjunction with the Hall sensors on the electric motor, an EKF was implemented to estimate the states of describing the motion of the system. Using these estimated system states, a controller was designed which compensated for the non-linear dynamics of the system and was able to control the deployment speed to high accuracy. The electronics built were able to execute the EKF in 7ms and the control algorithm was run every 30ms.

The performance of the tether angle sensor was evaluated. The sensor has a worst case accuracy of 2.5% when measuring angles near the edge of the AOV. The sensor is able to produce measurements every 200ms. The sensor can function with stars in the AOV and calculations showed that the LED will be five times more visible than the brightest star. A limitation of the sensor is that the AOV is only 30 degrees and the sensor will not be able to measure angles outside of this range.

Ultimately, the deployment motor control, measurement of the tether angle, and execution of estimation algorithms were done on a single PCB, serving as the tether control module.

Simulation of the deployment of the tether revealed that a residual oscillation after deployment cannot be avoided. The size of this oscillation depends on the deployment rate and can be minimised by deploying at a lower rate. Electrodynamic moments were found to be too weak to prevent this oscillation, but can be used to damp the oscillation after deployment. The system did however not become unstable, even at very large deployment rates. The orientation of the main satellite could be kept Nadir pointing using a 3-axis reaction wheel ADCS, despite large disturbance torques from the tether.

6.1.3 Electromagnetics

The electrodynamic performance of the system was studied. It was found that a critical part of an EDT system is maintaining good contact with the ionic plasma in space. This can be achieved using a hollow cathode plasma contactor. Currently, no plasma contactors suitable for a CubeSat sized satellite could be found in literature. Realistic assumptions were made to the performance that such a contactor would exhibit by consulting a professional in this field of study. The performance of the system was further based on these assumptions.

The average current induced in the tether was calculated to have magnitude of up to 15mA, causing moments on the system of up 12.2mN. These moments were found to be large enough to damp the oscillations in the tether angle and so control the tether to the Nadir direction. A bang-bang controller was designed which used a weighting system to determine when the EDT current should be allowed to flow in order to damp the oscillations in the tether angle.

Many uncertainties surrounding OML current collection theory were found, and the need for experimental verification of the theory was evident. The proposed mission could serve as a valuable experimental tool. The electrical currents through the tether could directly be measured and correlated with the theory. Further, the generated moment on the system can be determined by using the tether angle sensor developed in this study to track changes in the tether angle and from this, calculating the moments on the system. Once again these moments can be correlated with existing OML current collection theory and this theory, as well as the analytical solutions to the current profile used in this study, can be experimentally verified.

6.2 Future Research

For the purposes of testing the camera sensor, a setup was done where the LED was placed only a few metres away, which illuminated a large part of the image sensor. When the camera and LED are 500m apart, as it would be in space, the LED will, however, only illuminate one pixel on the sensor and the intensity of the light falling on the sensor would be less. Theoretical calculations show that the strength of the LED would still be sufficient for the

camera to successfully sense the LED, but this has to be verified experimentally. Doing tests over such a large distance, poses practical problems and an alternative test setup should be designed. The intensity of the LED can for instance be turned down by decreasing the current flowing through it, and the size on the camera can be decreased by placing the LED behind a shield with a pinhole for the light to shine through.

In this thesis the tether is treated according to the slack spring model and no attention is paid to the dynamics of the tether when slack. To improve the accuracy of the simulation of the tether system, a finite element analysis could be done, simulating the entire tether. The tether could be modelled as a series of spring-damper combinations, taking into account the elasticity, resistance against bending and friction within the tether. This requires complicated mathematical modelling and a complex simulation environment, but may provide significant insight to how the tether would react in space.

The body rotations of the satellites are treated separately from the dynamics of the tether system during mathematical modelling. As suggested in Section 3.3.7 the derivation of the equations of motion of the system can be expanded to include these rotations. This might reveal oscillating modes in the system which would not be apparent with the current simulations and may be necessary before considering launching such a satellite mission.

The availability of miniaturised plasma contactors for CubeSats poses a problem when evaluating the electrodynamic performance of a CubeSat tether system in space. The subject should be studied further and improvements in this technology should be monitored to identify the best alternative to such contactors. The effect of this should be considered in the mathematical modelling of the electron collection of the tether. As discussed, the PMG mission demonstrated the type of electron collection required from a small tether mission. The equipment on this mission were magnitudes too large for a CubeSat mission, though, and proves that sufficient plasma contact is the main limiting factor for a Nano-satellite tether mission.

The current sensor used for measuring the deployment distance between the satellites, relies on the incremental update of a distance variable by monitoring the Hall sensors on the deployment reel. As discussed, the risk exists of losing the current deployment distance in case of MCU reset. The solution proposed was to continuously write the deployment value to SRAM as backup and to continuously correlate these values. This should be implemented in hardware. A suggestion is to provide access for the MCU to write to the SRAM through the FPGA while the camera is not accessing the memory. The current hardware is set up in such a way that it could be implemented, but the programming and operational synchronisation must still be done.

The mechanical design of a reliable deployment spool is not discussed in this study. This does, however, form a critical part of the deployment process. Methods of ensuring reliable operation of the spool should be studied or this part of the system should be designed by professionals in this field.

Appendices

A Source Code

A.1 MCU Firmware

Camera setup:

The camera setups were done through i2c using the
"`i2c_writeByte(i2C_adress, register_adress, register_data)`" – function
Important values written to the camera registers are listed below

Register Address	Register Value	Description
0x12	0x80	Reset all registers
0x13	0x02	Enable AWB
0xA1	0x00	Exposure MSB 5 bits
0x10	0x00	Exposure bits 3-10(0x80 for regular picture in office light
0x04	0x01	Exposure LSB 2 bits
0x12	0x05	Raw RGB mode
0x40	0xC1	Output range 0x00–0xFF
0x1E	0x14	Flip image
0x11	0x80	Clock/Pre-scalar select

A.2 FPGA Firmware

main.vhd Behaviour:

```
BEGIN
    stage0: data_flow port map
(enable,rnw,detect,clk_cam,clk_mcu,cam_data,detect_data,mem_data,mcu_data);
    stage1: cam2sram port map (enable,rnw,href,vsync,clk_cam,cam_row,cam_col);
    stage2: sram2mcu port map (enable,rnw,detect,clk_mcu,mcu_row,mcu_col);
    stage4: adress_flow port map (enable, rnw, detect,
cam_row,cam_col,mcu_row,mcu_col,detect_row,detect_col,sram_row,sram_col);
    stage5: detect2mcu port map (enable,rnw,
detect,href,vsync,clk_mcu,clk_cam,cam_data,mem_data,detect_row,detect_col,detect_da
ta);
    stage6: createCamClk port map (clk_fpga,clk_camSup);

    process (enable,href,rnw, vsync,clk_cam)
    variable count_rows : std_logic_vector (9 DOWNTO 0) := "1111111111";

    begin
         if (enable = '0') then
            if (vsync = '0') then
                if rising_edge (href) and rnw = '0' then
                    if (count_rows < 1023) then
                        count_rows := count_rows + 1;
                    else
                        pic_taken <= '1';
                    end if;
                end if;
            else
                count_rows := "0000000000";
            end if;
       else
            pic_taken <= '0';
            count_rows := "0000000000";
       end if;
    end process;

    process (enable,pic_taken)
    begin
       if (enable = '0') and (pic_taken='1') then
            ack <= '1';
       else
            ack <= '0';
       end if;
    end process;

    process (enable,pic_taken,rnw)
    begin
       if (enable = '0') and (pic_taken='0') then
            if (rnw ='0') then
                nwe     <= '0';
                noe     <= '1';
            elsif (rnw = '1') then
                nwe     <= '1';
                noe     <= '0';
            end if;
       else
            nwe         <= '1';
            noe         <= '1';
       end if;
    end process;

END behavior;
```

A.4 Simulation Code

Extended Kalman Filter Algorithm

```
function [xOut,L] = EKF(xIn,Ts,TH0,PH0,L0,THD0,PHD0,LD0,OMEGA)

% Initialise Local Variables
persistent P x Q R
if isempty(P)
   x = [TH0;PH0;L0;THD0;PHD0;LD0];
   P = zeros(6,6);
   Q = diag([0.1 0.1 0.1 0.1 0.1 0.1]);
   R = diag([0.1 0.1 0.1]);
end

%Form Jacobians for F and H
temp = (x(4) + OMEGA);
Ft = zeros(6,6);
Ft(4) = 3*(OMEGA^2)*((sin(x(1)))^2 - (cos(x(1)))^2);
Ft(5) = 6*(OMEGA^2)*(sin(x(1)))*(cos(x(1)))*(sin(x(2)))*(cos(x(2)));
Ft(6) = -6*x(3)*(OMEGA^2)*(sin(x(1)))*(cos(x(1)))*(cos(x(2)))*(cos(x(2)));
Ft(10) = 2*temp*x(5)*((sec(x(2)))^2);
Ft(11) = (temp^2 + 3*OMEGA*(cos(x(1))))*((sin(x(2)))^2 - (cos(x(2)))^2);
Ft(12) = -2*x(3)*(sin(x(2)))*(cos(x(2)))*(temp^2)-
.....6*x(3)*(OMEGA^2)*((cos(x(1)))^2)*(sin(x(2)))*(cos(x(2)));
Ft(16) = (2*temp*x(6))/((x(3))^2);
Ft(17) = (2*x(5)*x(6))/((x(3))^2);
Ft(18) = ((x(5))^2)+((cos(x(2)))^2)*(temp^2) +
.....(OMEGA^2)*(3*((cos(x(1)))^2)*((cos(x(2)))^2) - 1);
Ft(19) = 1;
Ft(22) = 2*(x(5)*tan(x(2)) - x(6)/x(3));
Ft(23) = -2*(sin(x(2)))*(cos(x(2)))*temp;
Ft(24) = 2*x(3)*((cos(x(2)))^2)*temp;
Ft(26) = 1;
Ft(28) = 2*temp*tan(x(2));
Ft(29) = -2*(x(6))/(x(3));
Ft(30) = 2*x(3)*x(5);
Ft(33) = 1;
Ft(34) = -2*temp/(x(3));
Ft(35) = -2*x(5)/x(3);

H = [1 0 0 0 0 0;0 1 0 0 0 0; 0 0 1 0 0 0];

%Discritise F using first order Taylor expansion
F = eye(6) + Ft.*Ts;
```

```
f = zeros(6,1);
f(1) = x(4);
f(2) = x(5);
f(3) = x(6);
f(4) = -2*temp*(x(6)/x(3) - x(5)*tan(x(2)))-
3*(OMEGA^2)*(sin(x(1)))*(cos(x(1)));
f(5) = -2*x(6)*x(5)/x(3)-(sin(x(2)))*(cos(x(2)))*(temp^2 +
3*(OMEGA^2)*((cos(x(1)))^2));
f(6) = x(3)*((x(5))^2) + x(3)*((cos(x(2)))^2)*(temp^2) +
x(3)*(OMEGA^2)*(3*((cos(x(1)))^2)*((cos(x(2)))^2) - 1);

%Do control updates
P = F*P*F' + Q;
x = x + f.*Ts;

%Do measurement updates
K = P*H'/(H*P*H' + R);
P = (eye(size(K,1))-K*H)*P;
y = [x(1); x(2); x(3)];
x = x + K*(xIn - y);

%Outout Data
xOut = x;
L = K;
```

Lagrangian Algorithm

```
syms theta thetaD thetaDD phi phiD phiDD L LD LDD w0 muE muG M R

%Define Direct Cosine Matrix for rotating Orbit-frame to Body-frame
DCM_OB = [cos(theta) 0 -sin(theta);
    (sin(phi))*(sin(theta)) cos(phi) (sin(phi))*(cos(theta))
    (cos(phi))*(sin(theta)) -sin(phi) (cos(phi))*(cos(theta))];

%Define orbit and tether rotation vectors
wOrbit_O = [0; w0; 0];
wOrbit_B = DCM_OB*wOrbit_O;
wTether_B = [phiD; thetaD*cos(phi); thetaD*sin(phi)];

%Define orbit and tether unit vectors
p_B = [0; 0; 1];
er_O = [0; 0; 1];
er_B = DCM_OB*[0; 0; 1];

OMEGA_B = wOrbit_B + wTether_B;

%Define kinetic energy
```

```
T = 0.5*muE*(LD^2 + (L^2)*myDot((myCross((OMEGA_B), (p_B))),
(cross((OMEGA_B), (p_B)))));

%Define potential energy
V = -((w0^2)*(L^2)/2)*muE*(3*(myDot(p_B, er_B))^2 - 1);

%Calculate Lagrangian
Lag = simplify(T - V);
LCalc = simplify(Lagrange(Lag, [theta thetaD thetaDD phi phiD phiDD L LD
LDD]));
```

Where the *Lagrange()*-function is a MATLAB function available free from mathworks.com

B Datasheets

B.1 Motor Driver

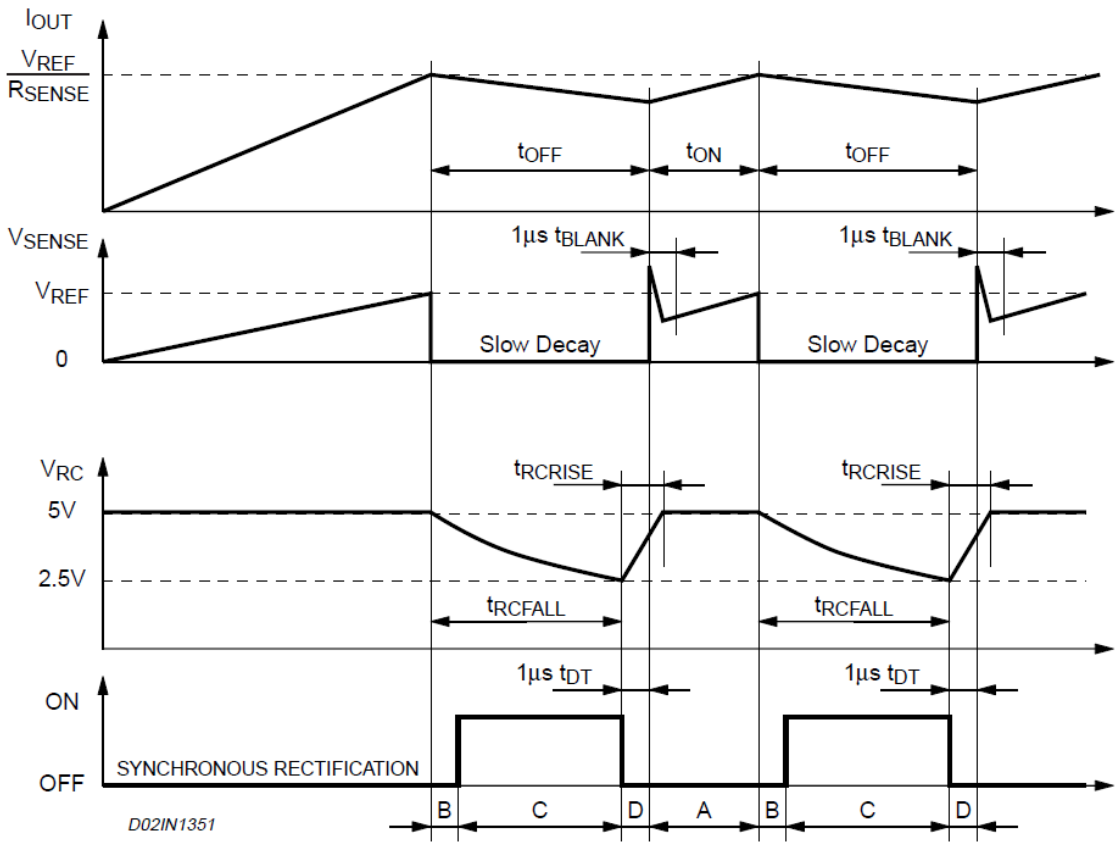

.

B.2 LED

VISHAY

VLHW4100

Vishay Semiconductors

Ultrabright White LED, Ø 3 mm

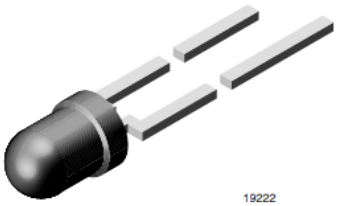

19222

FEATURES

- Clear, untinted lens
- Utilizing ultrabright InGaN technology
- High luminous intensity
- Luminous intensity and color categorized for each packing unit
- ESD-withstand voltage: up to 2 kV according to JESD22-A114-B
- Compliant to RoHS Directive 2002/95/EC

Pb-free

e3

RoHS COMPLIANT

OPTICAL AND ELECTRICAL CHARACTERISTICS (T_{amb} = 25 °C, unless otherwise specified)
WHITE VLHW4100

PARAMETER	TEST CONDITION	PART	SYMBOL	MIN.	TYP.	MAX.	UNIT
Luminous intensity	I_F = 20 mA	VLHW4100	I_V	4500	7150	11 250	mcd
Chromaticity coordinate x acc. to CIE 1931	I_F = 20 mA		x		0.33		
Chromaticity coordinate y acc. to CIE 1931	I_F = 20 mA		y		0.33		
Angle of half intensity	I_F = 20 mA		φ		± 22.5		deg
Forward voltage	I_F = 20 mA		V_F	2.8	3.2	3.8	V
Reverse current	V_R = 5 V		I_R			50	µA
Temperature coefficient of V_F	I_F = 20 mA		TC_{VF}		- 4		mV/K
Temperature coefficient of I_V	I_F = 20 mA		TC_{IV}		- 0.5		% / K

B.3 Loadcell

FUTEK MODEL Q10542 *OEM PARALLELOGRAM LOAD CELL*

INCH (mm)	R.O.= Rated Output		
WIRING CODE (WC 2)			
+Excitation	-Excitation	+Signal	-Signal
GREEN	BLACK	WHITE	RED

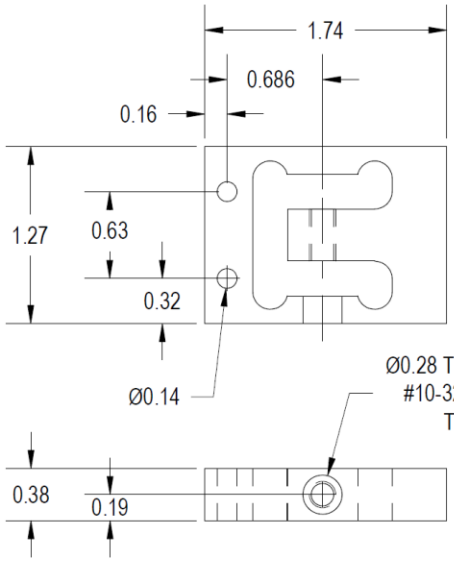

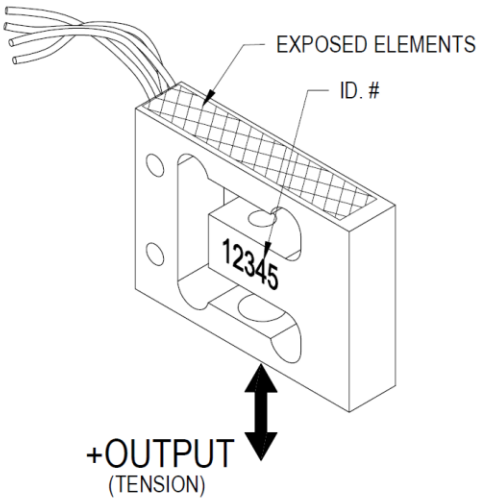

MECMESIN PART NO.	N	FUTEK MODEL Q10542 lb	FP NO.
400-168	9.8	2.2	FP12022-00519-C
400-169	44.5	10	FP12023-00519-C
400-170	222	50	FP12024-00519-C
400-171	445	100	FP12025-00519-C
400-172	890	200	FP12026-00519-C

SPECIFICATIONS:

RATED OUTPUT RANGE	*1.4 - 3.0 mV/V*
ZERO BALANCE	*±5% of R.O.*
SAFE OVERLOAD	*150% of R.O.*
ULTIMATE OVERLOAD	*200% of R.O.*
EXCITATION (VDC OR VAC)	*18 MAX.*
BRIDGE RESISTANCE	*1000 Ω nom.*
COMBINED (NL. & HYST.)	*±0.2% of R.O.*
TEMP. SHIFT ZERO	*±0.05% of R.O./°C*
TEMP. SHIFT SPAN	*±0.05% of LOAD/°C*
COMPENSATED TEMP.	*16 to 71°C*
OPERATING TEMP.	*-1 to 71°C*
CABLE	*#29 AWG 4 Conductor Teflon Color Coded Wire 6 in Long*
CALIBRATION	*1pt Tension (No Record Kept)*

MATERIAL: —

HEAT TREATMENT - FINISH: —

REVISIONS: (Refer to dwg # revision sheet)
A 5-05-01

OUTLINE DRAWING

STANDARD NOTES: (Unless Otherwise Specified)

- ALL DIMENSIONS ARE IN INCHES
- DRAWING INTERPRETATION DIMS. PER ASME-Y14.5M
- REMOVE BURRS AND BREAK SHARP EDGES .005 - .015
- THREADS PER HANDBOOK H-28
- DIMENSIONS ARE SHOWN AFTER PLATING

3rd ANGLE PROJ.

ANGLE: ±1/2°
CHAMFER: ±5°
TOLERANCE: .XX ±.01 .XXX ±.005

This drawing is submitted solely for the information and exclusive use of the original addressee. It is not to be divulged in whole or in part, by any firm or individual without written permission from:

FUTEK ADVANCED SENSOR TECHNOLOGY, INC.
10 THOMAS
IRVINE, CA 92618 USA
Phone: (949) 465-0900
Fax: (949) 465-0905

MODEL: Q10542 DWG No.: F3756
DRAWN BY: R. WALKER CHECKED BY: XXXXX
APPROVED BY: J. MOKHBERY DATE: Oct. 19, 2000

B.4 BLDC Motors

EC 45 Flat motor Æ45 mm, brushless, 30 Watt

maxon flat motor

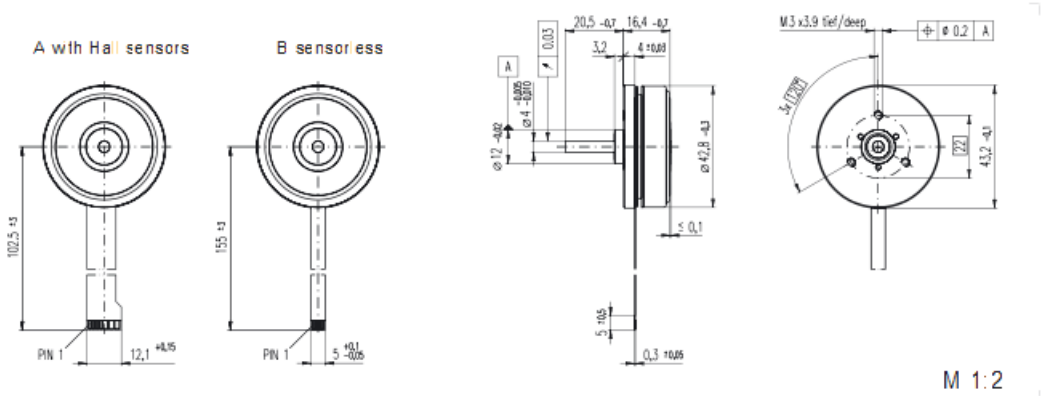

Stock program
Standard program
Special program (on request)

			Order Number	
		with Hall sensors	200142	
		sensorless		200189
Motor Data				
1	Assigned power rating	W	30	30
2	Nominal voltage	Volt	12.0	12.0
3	No load speed	rpm	4400	4400
4	Stall torque	mNm	260	220
5	Speed / torque gradient	rpm / mNm	17.5	20.5
6	No load current	mA	150	150
7	Terminal resistance phase to phase	Ohm	1.20	1.40
8	Max. permissible speed	rpm	10000	10000
9	Max. continuous current at 5000 rpm	A	2.30	2.30
10	Max. continuous torque at 5000 rpm	mNm	53.8	53.8
11	Max. efficiency	%	77.6	76.0
12	Torque constant	mNm / A	25.5	25.5
13	Speed constant	rpm / V	374	374
14	Mechanical time constant	ms	17.0	20.0
15	Rotor inertia	gcm²	92.5	92.5
16	Terminal inductance phase to phase	mH	0.410	0.410
17	Thermal resistance housing-ambient	K / W	4.0	4.0
18	Thermal resistance winding-housing	K / W	6.0	6.0
19	Thermal time constant windings	s	11.6	11.6
20	Thermal time constant stator	s	42.2	42.2

Specifications

- Axial preload > 5 N
- Max. ball bearing loads
  axial (dynamic) 2.8 N
  radial (7.5 mm from flange) 5.5 N
  Force for press fits (static) 50 N
  (static, shaft supported) 1000 N
- Ambient temperature range -40 ... +100°C
- Max. permissible winding temperature +125°C
- Weight of motor 88 g
- Version with and without Hall sensors
- 16 pole permanent magnet
- 3 phased coil stator with 4 pole shoes each
- Values listed in the table are nominal.
- Connection with Hall sensors sensorless
  Pin 1 4.5 ... 18 VDC Motor winding 1
  Pin 2 Hall sensor 3* Motor winding 2
  Pin 3 Hall sensor 1* Motor winding 3
  Pin 4 Hall sensor 2* neutral point
  Pin 5 GND
  Pin 6 Motor winding 3
  Pin 7 Motor winding 2
  Pin 8 Motor winding 1
- Adapter Order number Order number
  see p. 275 220300 220310
- Connector Article number Article number
  AMP 1-487551-* 487551-4
  MOLEX 52207-1190 52207-0490
  MOLEX 52085-1110 52085-0410

  Pin for design with Hall sensors:
  FFC, 11 pole, pitch 1.0 mm, top contact style

  *Internal pull-up (7 ... 13 kW) on pin 1
- For wiring diagram for Hall sensors, see p. 28

Operating Range

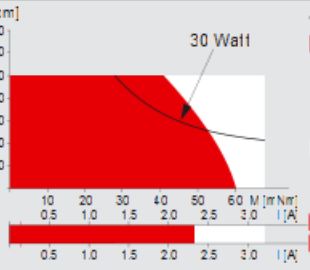

Comments Details on page 148

Curve of constant assigned power rating

Continuous operation
In observation of above listed thermal resistances (lines 17 and 18) the maximum permissible winding temperature will be reached during continuous operation at 25°C ambient.
= Thermal limit.

Short term operation
The motor may be briefly overloaded (recurring).

200189 Motor with high resistance winding
200142 Motor with low resistance winding

maxon Modular System Overview on page 17 - 21

Spur Gearhead
Æ45 mm
0.5 - 2.0 Nm
Details page 228

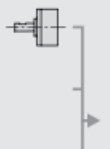

Recommended Electronics:
AECS 35/3 page 262
DEC 50/5 264
DECV 50/5 265
EPOS 24/1 271
EPOS 24/5 271
Notes 17

NEW

FAULHABER

Brushless Flat DC-Micromotors 0,6 mNm

For combination with Speed Controller: SC1801

Series 1509 ... B

		1509 T	006 B	012 B	
1	Nominal voltage	U_N	6	12	Volt
2	Terminal resistance, phase-phase	R	22,0	92,8	Ω
3	Output power [1]	$P_{2max.}$	0,31	0,30	W
4	Efficiency	$\eta_{max.}$	66	65	%
5	No-load speed	n_0	14 700	14 700	rpm
6	No-load current	I_0	0,0174	0,0067	A
7	Stall torque	M_H	0,97	0,92	mNm
8	Friction torque, static	C_0	0,025	0,025	mNm
9	Friction torque, dynamic	C_V	$2,6 \cdot 10^{-6}$	$2,6 \cdot 10^{-6}$	mNm/rpm
10	Speed constant	k_n	2 623	1 312	rpm/V
11	Back-EMF constant	k_E	0,381	0,762	mV/rpm
12	Torque constant	k_M	3,64	7,28	mNm/A
13	Current constant	k_I	0,275	0,137	A/mNm
14	Slope of n-M curve	$\Delta n/\Delta M$	15 858	16 721	rpm/mNm
15	Terminal inductance, phase-phase	L	590	2 350	µH
16	Mechanical time constant	τ_m	115	121	ms
17	Rotor inertia	J	0,69	0,69	gcm²
18	Angular acceleration	$\alpha_{max.}$	14	13	$\cdot 10^3$ rad/s²
19	Thermal resistance	R_{th1} / R_{th2}	65 / 45		K/W
20	Thermal time constant	τ_{w1} / τ_{w2}	10 / 130		s
21	Operating temperature range		-25 ... +80		°C
22	Shaft bearings		ball bearing, preloaded		
23	Shaft load max.:				
	– radial at 3 000/16 000 rpm (3mm from mounting flange)		2,0 / 0,5		N
	– axial at 3 000/16 000 rpm (push-or-pull)		2,0 / 1,7		N
	– axial at standstill (push-or-pull)		15		N
24	Shaft play:				
	– radial	≤	0,015		mm
	– axial	=	0		mm
25	Housing material		plastic		
26	Weight		6,5		g
27	Direction of rotation		electronically reversible		

Recommended values - mathematically independent of each other					
28	Speed up to	$n_{e max.}$	16 000	16 000	rpm
29	Torque up to [1] [2]	$M_{e max.}$	0,52 / 0,60	0,51 / 0,58	mNm
30	Current up to [1] [2]	$I_{e max.}$	0,174 / 0,198	0,085 / 0,096	A

[1] at 5 000 rpm
[2] thermal resistance R_{th2} not reduced / thermal resistance R_{th2} by 55 % reduced

Note:

The diagram indicates the recommended speed in relation to the available torque at the output shaft for a given ambient temperature of 22 °C.

The diagram shows the motor in a completely insulated as well as thermally coupled condition (R_{th2} 55% reduced).

The nominal voltage curve shows the operating point at nominal voltage in the insulated and thermally coupled condition. Any points of operation above the curve at nominal voltage will require a higher operating voltage. Any points below the nominal voltage curve will require less voltage.

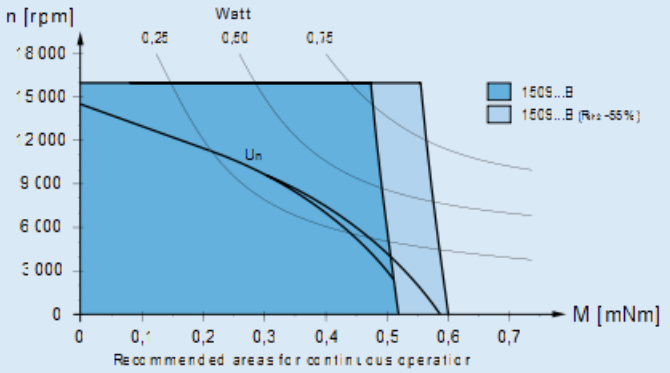

For notes on technical data and lifetime performance refer to "Technical Information"
Edition 2010 – 2011

C CAD

C.1 Base Manufacturing Drawings

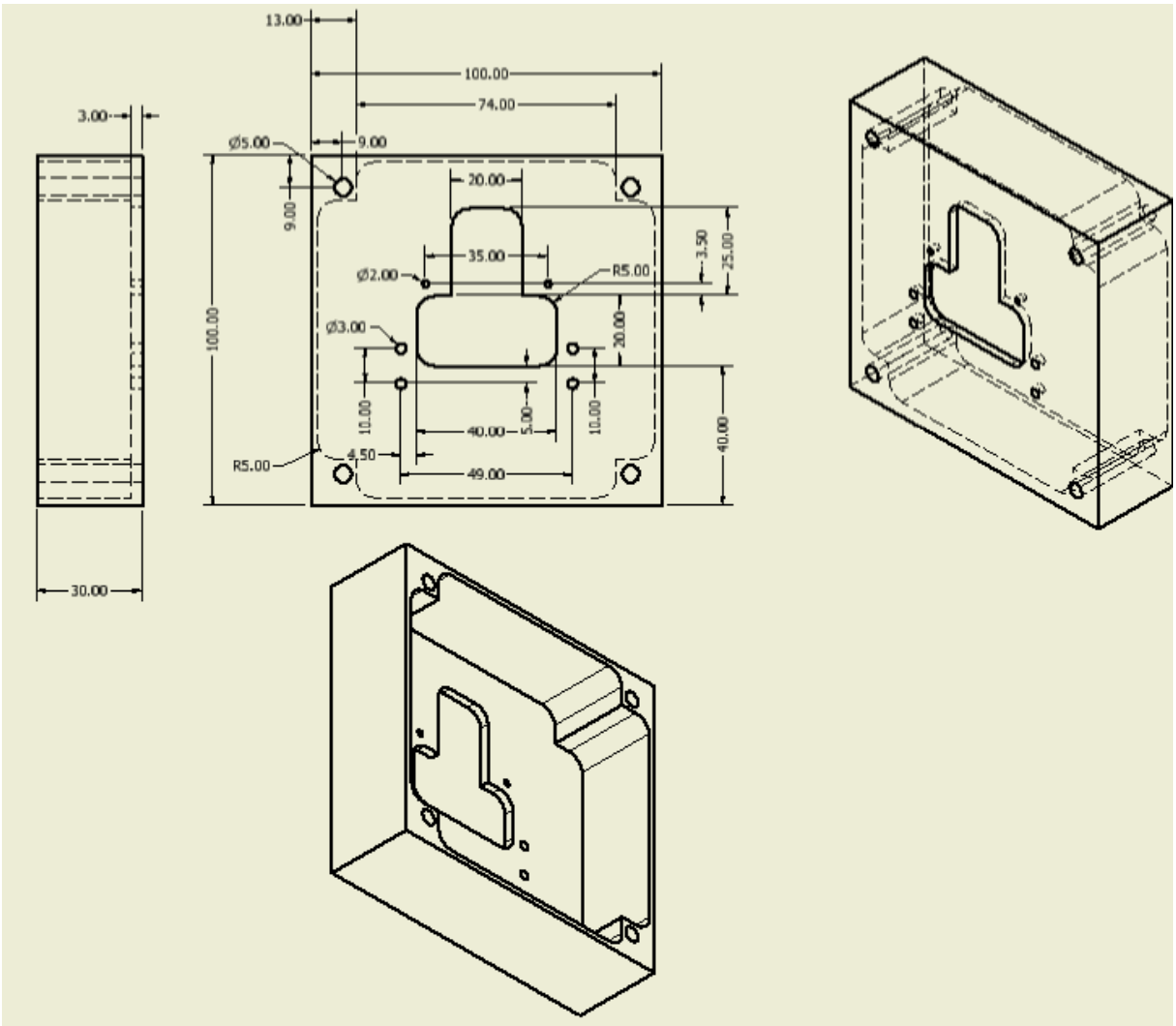

C.2 Bearing Bracket

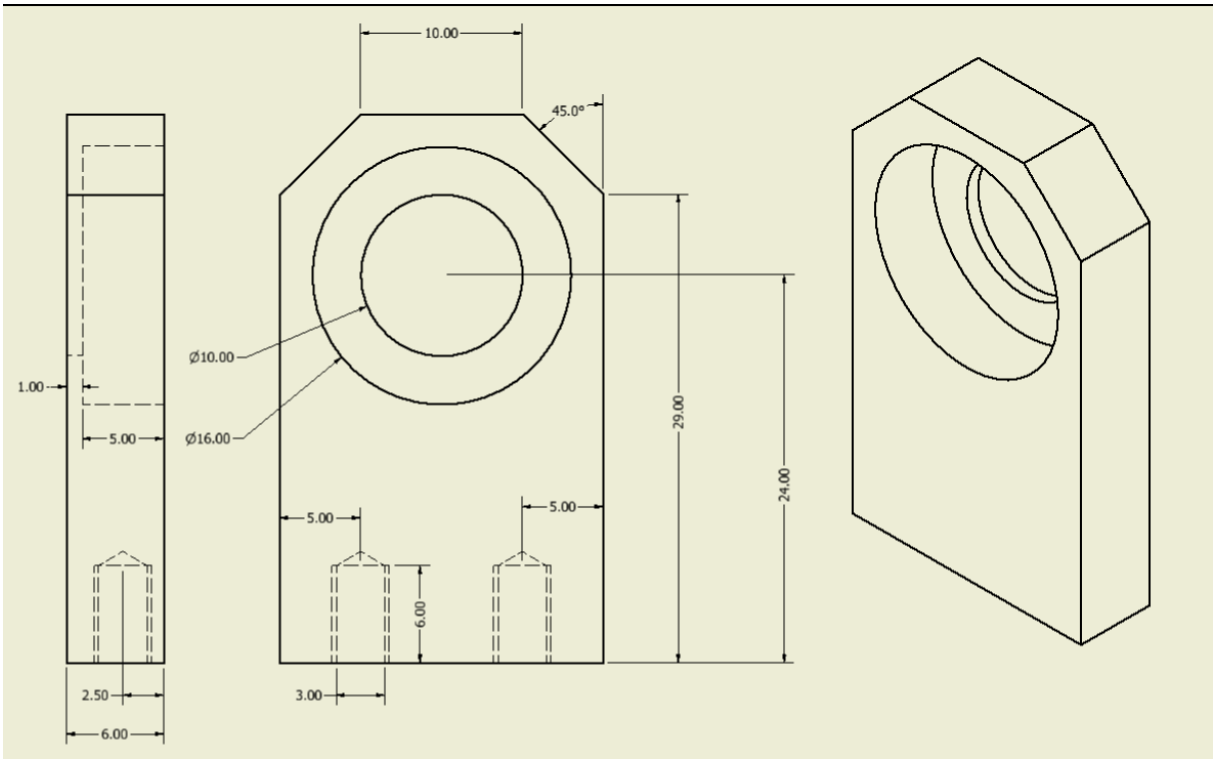

D Circuit diagrams

FPGA Pin Layout

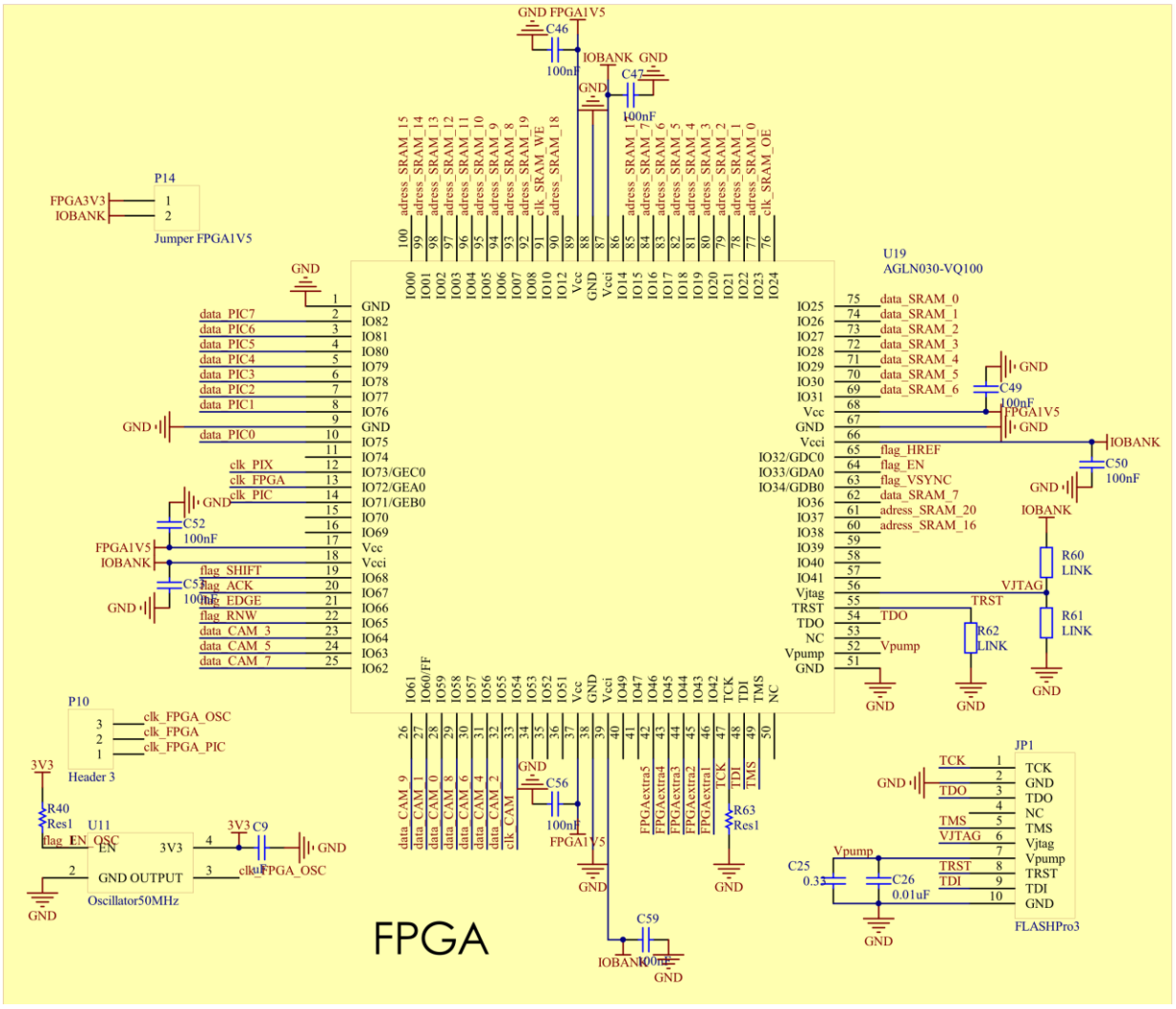

MCU Pin Layout

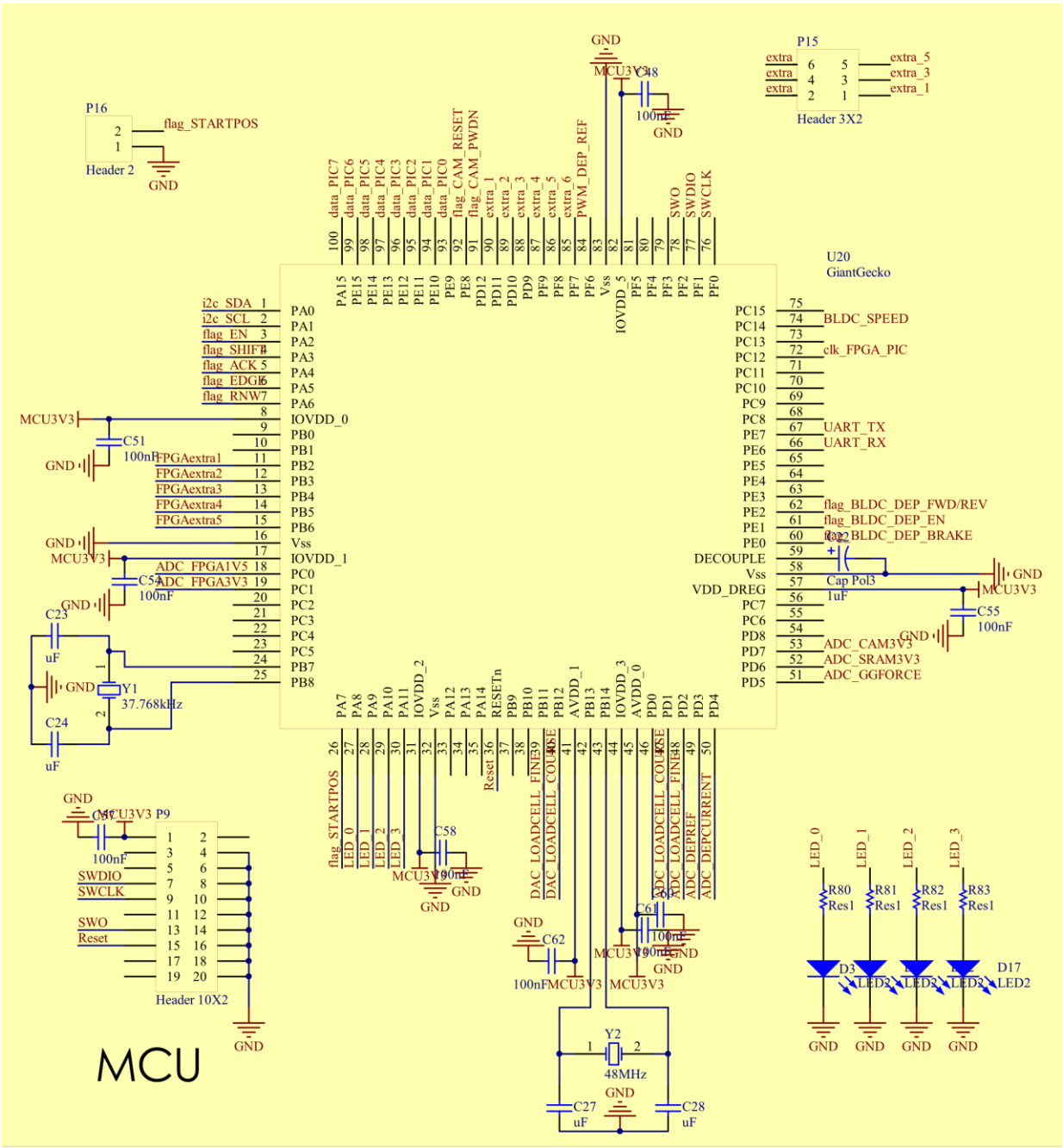

References

[1] M.L. Cosmo and E.C. Lorenzini, *Tethers In Space Handbook*, NASA Marshall Space Flight Center is, Ed. Smithsonian Astrophysical Observatory, 1997.

[2] Michel van Pelt, *Space Tethers and Space Elevators*.: Praxis Publishing, 2009.

[3] NASA. Nasa Multimedia. [Online]. http://www.nasa.gov/multimedia/index.html

[4] P. Palmer, M. Roberts K. Uldall Kristiansen, "A unification of models of tethered satellites," urrey Space Centre and Department of Mathematics, 2011.

[5] Alain J. Brizard, *An Introduction To Lagrangian Mechanics*.: World Scientific, 2008.

[6] A. Misra, "Dynamics and control of tethered satellite systems," *Acta Astronautica*, vol. 63, no. 11-12, pp. 1169-1177, 2008.

[7] Paul Williams, "Optimal Control of Electrodynamic Tether Orbit Transfers Using Timescale Separation," *Journal of Guidance, Control, and Dynamics*, vol. 12, no. 4, pp. 979-998, 2010.

[8] M. B. Larsen and M. Blanke, "Passivity-Based Control of a Rigid Electrodynamic Tether," *Journal of Guidance, Control, and Dynamics*, vol. 34, no. 1, pp. 118-127, 2011.

[9] D.E. Hastings, E. Ahedo R.I. Samanta Roy, "Systems Analysis of Electrodynamic Tethers," *ournal of spacecraft and rockets*, vol. 29, no. 3, 1992.

[10] Claudio, Pelaez, Jesus, Sanjurjo, Manuel Bombardelli, "Asymptotic Solution for the Current Profile of Passive Bare Electrodynamic Tethers," *Journal of Propulsion and Power*, vol. 26, no. 6, pp. 1291-1304, 2010.

[11] Jose Manuel Nuñez-Ayllón, Jesus Peláez Claudio Bombardelli, "Performance Analysis Of Bare Electrodynamic Tethers As Microsat Deorbiting Systems," *ADVANCES IN THE ASTRONAUTICAL SCIENCES*, vol. Volume 136, no. 1, 2010.

[12] L. Johnson , J. Moore , F. Bagenal, D.L. Gallagher, Electrodynamic Tether Propulsion and Power Generation at Jupiter, 1998, Marshall Space Flight Center.

[13] W. Ivanic , K. Dorpelkus, L. Wood, "Using Light-Emitting Diodes for intersatellite links," in *Aerospace Conference, 2010 IEEE*, 2010.

[14] Jean, Hoffmann, Nick Koster, CubeSat Tether System, 2009, Project Definition Document, Department of Aerospace Engineering Sciences.

[15] IAGA. (2010) International Geomagnetic Reference Field. [Online]. http://www.ngdc.noaa.gov/IAGA/vmod/igrf.html

[16] R. D., Lorenzini, E. C., Sanmart-egrave, J., Pel-Uuml, J., Mart-egrave, M., Johnson, C. L., Vas, I. E. Estes, "Bare Tethers for Electrodynamic Spacecraft Propulsion," *Journal of Spacecraft and Rockets*, vol. 37, no. 2, 2000.

[17] L. Johnson and M. Herrmann, International Space Station Electrodynamic Tether Reboost Study, 1998, Marshall Space Flight Center, NASA.

[18] Von Karman Institute for Fluid Dynamics, Belgium, Call for CubeSat Proposals for QB50, 2012.

[19] Haim Baruh, *Analytical Dynamics*, 1st ed.: McGraw Hill, 1999.

[20] Auret J., Design of an Aerodynamic Attitude Control System for a CubeSat, 2012.

[21] K.J. Pascoe, *Properties of materials for electrical engineers*.: John Wiley & Sons, 1973.

[22] Bombardelli Claudio, , Senior Researcher at Technical University of Madrid. Published 22 papers in pear reviewed ISI-recognised journals and have delivered over 30 papers at conference proceedings.

[23] M. Charro, J. Pelaez, I. Tinao, S. Elaskar, A. Hilgers, M. Martinez-Sanchez, J. R. Sanmartin, "Floating bare tether as upper atmosphere probe," *Journal of Geophysical Research*, vol. 111, 2006.

[24] H.E. Loubser, The development of Sun and Nadir sensors for a solar sail CubeSat, 2010, M.Sc Thesis.

[25] L.G. Kraige, J.L. Meriam, *Engineering Mechanics Dynamics*, 5th ed.: John Wiley & Sons, 2003.

[26] W.H. Steyn, A Multi-mode Attitude Determiniation and Control System for Small Satellites, 1995, Ph.D Thesis.

[27] G. V. Khazanov, E. N. Krivorutsky, and K. Sorenson, Analysis of Bare-Tether Systems as a Thruster for MXER Studies, 2005, NASA, Marshall Space Flight Center.

[28] J.R. Sanmartin, E. Ahedo, "Analysis of Bare-Tether Systems for Deorbiting Low-Earth-Orbit Satellites," *Journal Of Spacecraft And Rockets*, vol. 39, no. 2, 2002.

This documentation is based on a template created by Patrik FUHRER and Pedro DE ALMEIDA (Software Engineering Group, University of Fribourg, Switzerland). The template is open source.